

Spring 1980

Influence of Nonequilibrium Radiation and Shape Change on the Flowfield of a Jupiter Probe With Ablation and Mass Injection

Sundaresa Venkata Subramanian
Old Dominion University

Follow this and additional works at: https://digitalcommons.odu.edu/mae_etds



Part of the [Aerospace Engineering Commons](#), [Astrophysics and Astronomy Commons](#), and the [Mechanical Engineering Commons](#)

Recommended Citation

Subramanian, Sundaresa V.. "Influence of Nonequilibrium Radiation and Shape Change on the Flowfield of a Jupiter Probe With Ablation and Mass Injection" (1980). Doctor of Philosophy (PhD), Dissertation, Mechanical & Aerospace Engineering, Old Dominion University, DOI: 10.25777/d4cs-ej57
https://digitalcommons.odu.edu/mae_etds/280

This Dissertation is brought to you for free and open access by the Mechanical & Aerospace Engineering at ODU Digital Commons. It has been accepted for inclusion in Mechanical & Aerospace Engineering Theses & Dissertations by an authorized administrator of ODU Digital Commons. For more information, please contact digitalcommons@odu.edu.

INFLUENCE OF NONEQUILIBRIUM RADIATION AND SHAPE
CHANGE ON THE FLOWFIELD OF A JUPITER PROBE WITH
ABLATION AND MASS INJECTION

by

Sundaresa Venkata Subramanian

B.E. (Mechanical Engineering) June 1972, University of Madras, India

M.E. (Mechanical Engineering) December 1976, Old Dominion University

A Dissertation Submitted to the Faculty of
Old Dominion University in Partial Fulfillment of the
Requirements for the Degree of

DOCTOR OF PHILOSOPHY

MECHANICAL ENGINEERING

OLD DOMINION UNIVERSITY
March 1980

Approved by:

Dr. Surendra N. Tiwari (Director)

ABSTRACT

INFLUENCE OF NONEQUILIBRIUM RADIATION AND SHAPE CHANGE ON THE FLOWFIELD OF A JUPITER PROBE WITH ABLATION AND MASS INJECTION

SUNDARESA VENKATA SUBRAMANIAN

OLD DOMINION UNIVERSITY, 1980
DIRECTOR: DR. SURENDRA N. TIWARI

The influence of nonequilibrium radiative energy transfer and the effect of probe configuration changes on the flow phenomena around a Jovian entry body is investigated. The radiating shock-layer flow is assumed to be axisymmetric, viscous, laminar and in chemical equilibrium. The radiative transfer equations are derived under nonequilibrium conditions which include multi-level energy transitions. The equilibrium radiative transfer is calculated with an existing nongray radiation model which accounts for molecular band, atomic line and continuum transitions. The nonequilibrium results are obtained with and without ablation injection in the shock layer. The nonequilibrium results are found to be influenced greatly by the temperature distribution in the shock layer. In the absence of ablative products, the convective and radiative heating to the entry body are reduced significantly under nonequilibrium conditions. The influence of nonequilibrium is found to be greater at higher entry altitudes. With coupled ablation and carbon phenolic injection, 16 chemical species are used in the ablation layer for radiation absorption. Equilibrium and nonequilibrium results are compared under peak heating conditions. For the study of the probe shape change effects, the initial body shapes considered are 45-degree sphere cone,

35-hyperboloid, and 45-degree ellipsoid. In all three cases, the results indicate that the shock-layer flowfield and heat transfer to the body are influenced significantly by the probe shape change. The effect of shape change on radiative heating of the after-bodies is found to be considerably larger for the sphere cone and ellipsoid than for the hyperboloid.

ACKNOWLEDGEMENTS

I am indebted to Dr. Surenda N. Tiwari, Eminent Professor, Mechanical Engineering and Mechanics Department for his guidance and valuable suggestions during the entire course of this study. Equally, I wish to thank Dr. Kenneth Sutton of NASA Langley Research Center for assisting and participating in the proceedings of this investigation.

To my parents in India, I extend my deepest gratitude for their patience, sacrifice and encouragement during the years of my study.

I wish to thank Drs. Randolph A. Graves, James N. Moss, and Jim J. Jones of NASA Langley Research Center for providing the technical support and encouragement during these years. My sincere appreciation is extended to the dissertation advising committee Drs. Robert L. Ash, Wynford L. Harries, and Charlie H. Cooke for their continued interest and advice regarding this work. I wish to extend special thanks to Dr. Kuo-yen Szema currently at Virginia Polytechnic Institute and State University for the numerous constructive discussions we had in the past three years of graduate study and research work. Finally, I thank Beverly A. Johnson for her assistance in typing the final version of this dissertation.

This work was supported by NASA Langley Research Center through Grants NAS1-14193-26 and NSG-1500.

TABLE OF CONTENTS

	<u>Page</u>
LIST OF TABLES	v
LIST OF FIGURES	vi
LIST OF SYMBOLS	x
1. INTRODUCTION	1
2. BASIC FORMULATION.	8
2.1 Inviscid Flow Equations	8
2.2 Viscous Flow Equations.	10
2.3 Free-stream and Boundary Conditions	13
3. RADIATIVE TRANSPORT MODELS	17
3.1 Radiative Flux Equations.	17
3.1.1 LTE Radiative Flux Equations	18
3.1.2 NLTE Radiative Flux Equations.	25
3.2 Spectral Model for Gaseous Absorption	32
4. RADIATIVE LIFETIMES AND COLLISIONAL PROCESSES FOR THE SHOCK-LAYER GASES.	39
4.1 Radiative Lifetime of Excited States.	39
4.2 Collisional Relaxation Time	42
5. THERMODYNAMIC AND TRANSPORT PROPERTIES	50
6. METHOD OF SOLUTION	57

	<u>Page</u>
7. RESULTS AND DISCUSSIONS.	60
7.1 Significance of Radiation Models on the Flow Field Solutions	60
7.1.1 Comparison of Inviscid and Viscous Results	61
7.1.2 Viscous Results for a 55-Degree Sphere cone. . . .	65
7.1.3 Viscous Results for a 50-Degree Hyperboloid. . . .	71
7.2 Influence of NLTE Radiation Without Ablation Injection. .	81
7.2.1 NLTE Results for a 50-Degree Hyperboloid	81
7.2.2 NLTE Results for a 55-Degree Sphere Cone	98
7.3 Importance of NLTE Radiation With Ablation Injection. . .	100
7.4 Effect of Probe Shape Change on the Flow Phenomena. . . .	110
7.4.1 Results for 45-Degree Sphere Cone.	116
7.4.2 Results for 35-Degree Hyperboloid.	129
7.4.3 Comparison of Peak Heating Results	138
8. CONCLUSIONS.	146
REFERENCES	148
APPENDIX	153

LIST OF TABLES

<u>Table</u>		<u>Page</u>
1	Free-stream conditions for Jovian entry.	14
2	Coefficients for evaluation of the specific heat at constant pressure for hydrogen-helium species.	53
3	Coefficients for evaluation of the specific heat at constant pressure for the ablative species	54
4	Coefficients for evaluating the thermal conductivity of the shock-layer species	56

LIST OF FIGURES

<u>Figure</u>	<u>Page</u>
1a. Physical model and coordinate system.	9
1b. Physical model and coordinate system for the radiative field	19
2. A 30-Step model to approximate the absorption by Nicolet's detailed model ($T_s = 15,500$ K).	37
3. Collisional relaxation time for atomic and molecular hydrogen species.	46
4. Variation of collisional relaxation time with temperatures.	47
5. Collisional relaxation time for hydrogen ions	49
6. Temperature distribution along the stagnation streamline for inviscid and viscous analysis (55-degree sphere cone, $Z = 116$ km)	62
7. Shock standoff variation with distance along the body surface for inviscid and viscous analysis (55-degree sphere cone, $Z = 116$ km)	64
8. Radiative heating along the body for inviscid and viscous analysis (55-degree sphere cone, $Z = 116$ km) . . .	66
9. Temperature distribution along the stagnation streamline for two different free-stream densities (55-degree sphere cone)	67
10. Temperature variation just behind the shock ($n = 0.05$) with distance along the body surface (55-degree sphere cone, $Z = 116$ km).	69
11. Shock standoff variation with distance along the body surface (55-degree sphere cone, $Z = 116$ km).	70
12. Radiative heating along the body for two different free-stream densities (55-degree sphere cone)	72
13. Radiative heating along the body for entry conditions at $Z = 131$ km (55-degree sphere cone)	73
14. Temperature distribution along the stagnation streamline (50-degree hyperboloid, $Z = 116$ km)	74
15. Temperature distribution just behind the shock ($n = 0.07$) with distance along the body surface (50-degree hyperboloid, $Z = 116$ km).	75

<u>Figure</u>	<u>Page</u>
16. Shock standoff variation with distance along the body surface (50-degree hyperboloid, $Z = 116$ km)	77
17. Radiative heating along the body for entry conditions at $Z = 116$ km (50-degree hyperboloid).	78
18. Radiative heating along the body for free-stream conditions at $Z = 116$ km (50-degree hyperboloid)	79
19. Radiative heating along the body for entry conditions at $Z = 131$ km (50-degree hyperboloid)	80
20. Equilibrium and nonequilibrium absorption coefficients for two-level energy transitions	82
21a. Variation of relaxation time across the shock-layer for H-H and $0.5 \text{ H} - 0.5 \text{ H}_2$ collisions	83
21b. Variation of relaxation time across the shock-layer for H-H and $\text{H}^+ - \text{H}^+$ collisions.	84
21c. Variation of relaxation time across the shock-layer for $0.95 \text{ H} - 0.05 \text{ H}_2$ and $\text{H}^+ - \text{H}^+$ collisions	85
22a. Temperature variation across the shock layer for H-H and $\text{H}^+ - \text{H}^+$ collisions	87
22b. Temperature variation across the shock layer for $0.95 \text{ H} - 0.05 \text{ H}_2$ and $\text{H}^+ - \text{H}^+$ collisions.	88
23. Temperature variation along the body for two locations in the shock layer, H-H and $\text{H}^+ - \text{H}^+$ collisions.	90
24. Shock-standoff variation with distance along the body surface.	91
25. Radiative heating along the body for entry conditions at $Z = 109$ km, H-H and $\text{H}^+ - \text{H}^+$ collisions.	92
26. Radiative heating along the body for entry conditions at $Z = 116$ km	94
27. Radiative and convective heating along the body for entry conditions at $Z = 131$ km, H-H and $\text{H}^+ - \text{H}^+$ collisions.	96
28. Stagnation-point radiative heating for different entry altitudes, H-H and $\text{H}^+ - \text{H}^+$ collisions.	97

<u>Figure</u>	<u>Page</u>
29. Radiative heating along the body (55-degree sphere cone) for entry conditons at $Z = 116$ km, H-H and $H^+ - H^+$ collisions	99
30. Species concentration in the vicinity of the wall	101
31. Temperature distribution across the shock-layer	103
32. Enthalpy and density variations across the shock layer	104
33. Shock standoff variation with distance along the body surface.	105
34. Pressure and heating rate variations along the body surface.	107
35. Variation of heating rate along the body surface.	108
36. Ablation mass loss rate along the body surface.	109
37a. Forebody configurations for 45-degree sphere cone	113
37b. Configuration for 35-degree hyperboloid	114
37c. Configuration for 45-degree ellipsoid	115
38. Shock-standoff variation for 45-degree sphere cone, $Z = 116$ km	117
39. Shock-standoff variation for 45-degree sphere cone.	118
40. Variation of temperature just behind the shock for 45-degree sphere cone	119
41. Variation of density just behind the shock for 45-degree sphere cone	121
42. Variation of density in the shock layer for 2 body location ($s = 0$ and 1.4), 45-degree sphere cone	122
43a. Variation of v-velocity component in the shock-layer along the stagnation streamline and for $s = 1.4$ and $Z = 116$ km.	123
43b. Variation of v-velocity component in the shock layer along the stagnation streamline and for $s = 1.4$ and $Z = 138$ km.	124
44. Surface pressure variation for 45-degree sphere cone.	126

<u>Figure</u>	<u>Page</u>
45a. Radiative heating rates for 45-degree sphere cone, $Z = 116$ km	127
45b. Radiative heating rates for 45-degree sphere cone.	128
46. Shock-standoff variation for 35-degree hyperboloid.	130
47. Variation of temperature just behind the shock for 35-degree hyperboloid	131
48. Variation of density just behind the shock for 35-degree hyperboloid	132
49. Variation of density in the shock layer for body location ($s = 0$ and 1.5), 35-degree hyperboloid	134
50. Variation of v -velocity component in the shock layer for 2 body locations ($s = 0$ and 1.5), 35-degree hyperboloid	135
51. Surface pressure variation for 35-degree hyperboloid.	136
52. Radiative heating rates for 35-degree hyperboloid	137
53. Comparison of shock standoff distance for $Z = 116$ km	139
54. Comparison of shock temperature for $Z = 116$ km	140
55. Comparison of shock density for $Z = 116$ km	141
56. Comparison of surface pressure for $Z = 116$ km.	143
57. Comparison of radiative heating rates for $Z = 116$ km	144
A.1. Finite difference representation of flow field.	155
A.2. Flow-chart for shock-layer solution procedure	159
A.3. Flow-chart for subroutine SHOKLY for shock-layer solution.	160
A.4. Flow-chart for subroutine NRAD.	161
A.5. Definition of integrals used in NRAD.	163

LIST OF SYMBOLS

A_{nm}	Einstein coefficient for spontaneous emission
$A'\pi_u$	lower electronic energy level for the C_2 - Freymark transition
$a^3\pi_u$	lower electronic energy level for the C_2 - Swan transition
B_{mn}	Einstein coefficient for absorption
B_{nm}	Einstein coefficient for stimulated emission
B_ν	Planck function
c	speed of light
C_{10}	collisional deexcitation rate coefficient
C_i	mass fraction of species i in the shock layer, ρ_i/ρ
C_p	equilibrium specific heat of mixture, $\sum C_i C_{p,i}$
$C_{p,i}$	specific heat of species i , $C_{p,i}^*/C_{p,\infty}^*$
D_{ij}	binary diffusion coefficient
$D'\Sigma_u^+$	upper electronic energy level for the C_2 - Mulliken transition
$d^3\pi_g$	upper energy level for the C_2 - Swan transition
$E'\Sigma_g^+$	upper energy level for the C_2 - Freymark transition
h	specific enthalpy, h^*/V_∞^{*2} (also Planck constant)
H_T	total enthalpy, $h + (u^2+v^2)/2$
I_ν	intensity of radiation
\bar{I}_ν	mean radiation intensity averaged over the spectral interval $\Delta\nu$
J_ν	NLTE source function

J_i	mass diffusion flux of species i , $J_i^* R_N / \mu_{ref}^*$
k	thermal conductivity of mixture, $k^* / \mu_{ref}^* C_{p,\infty}^*$ (also Boltzmann constant)
Le	Lewis number, $\rho^* D_{ij}^* C_p^* / k^*$
M^*	molecular weight of mixture
m_1	net weight of a H_2 molecule, gm/molecule
\dot{m}_a	ablation mass loss rate, $\text{kg m}^2 \text{sec}^{-1}$
\bar{m}	principal quantum number of the lower level
N_{H_2}	number density of H_2
N_m	number density of particles in the m th level
N_n	number density of particles in the n th level
n	coordinate normal to the body surface
\bar{n}	principal quantum number of the upper level
P	pressure, $P^* / (\rho_\infty^* V_\infty^{*2})$
Pr	Prandtl number, $\mu^* C_p^* / k^*$
$q_{c,w}$	convective heat flux to the body
q_R	net radiative heat flux, $q_R^* / (\rho_\infty^* V_\infty^{*3})$
q_R	spectral radiative heat flux
$q_{R,w}$	radiative heat flux to the body
R_N^*	body nose radius
R^*	universal gas constant
R_b^*	radius of the body
r	radius measured from axis of symmetry to a point on the body surface, r^* / R^*

r_s	radius measured from axis of symmetry to a point on the bow shock, r_s^*/R_N^*
$ R_e/ea_0 $	electronic transition moment
S	spin quantum number
s	coordinate along the bow shock, s^*/R_N^*
T	temperature, T^*/T_{ref}^*
T^*	dimensional temperature
T_{ref}^*	reference temperature, $V_\infty^*/C_{p,\infty}^*$
u	velocity tangent to body surface, u^*/V_∞^*
v	velocity normal to body surface, v^*/V_∞^*
V_∞^*	free-stream velocity, km/sec
\bar{v}	mean speed of the colliding species cm sec^{-2}
$x'\Sigma_g^+$	lower energy level for the C_2 - Mulliken transition
Z	entry altitude, km
α	shock angle, defined in figure 1a
Γ	quantity defined as $\Gamma = 1 + \kappa n = 1 + \kappa \delta \eta$
δ	shock-layer thickness (same as n_s), $f(\xi, t)$
ϵ	gray surface emittance
ϵ_1	surface emittance of the body
ϵ_2	surface emittance of the shock
θ	body angle defined in figure 1a
η	transformed n coordinate, $n/n_s = n/\delta$
η_c	collisional relaxation time
η_r	radiative lifetime
κ	body curvature ($= -d\theta/ds$), $\kappa^* R_N^*$

κ_ν	spectral absorption coefficient
ξ	coordinate along the body surface, $\xi = s$
μ	viscosity of mixture, μ^*/μ_{ref}^*
μ_{ref}	reference viscosity, $\mu^*(T_{\text{ref}}^*)$
ρ	density of mixture, ρ^*/ρ_∞^*
σ	Stefan Boltzmann constant
τ	optical coordinate
τ_0	optical thickness

Subscript

i	i th species
s	shock value
w	wall value
∞	free-stream condition
ν	radiation frequency
k,o	lower state of the energy level
j,l	upper state of the energy level

Superscripts

"	lower state of the energy level
'	upper state of the energy level
*	dimensional quantity

1. INTRODUCTION

During the exploratory missions to the planetary atmospheres the entry spacecraft is subjected to various flow environments and heating conditions. The type and intensiveness of this heating mainly depends on the atmospheric composition of the planet and the trajectory of the entry vehicle. At hypersonic entry conditions, radiation plays a very important role in the analysis of the flow phenomena around the planetary entry body. The radiative energy transferred to the body from the high temperature shock-layer gas exceeds the convective and aerodynamic heating rates. The problem of radiative heating of planetary entry bodies have been investigated extensively in the literature [1-4]*. One such situation where the radiative heating constitutes the major portion of the heat transferred to the probe is the case of Jovian entry heating [5-8]. In order to study the composition and structure of the Jupiter's atmosphere, the National Aeronautics and Space Administration has scheduled a probe spacecraft to enter the planet Jupiter in 1985. At times, the entry velocity of the Jupiter probe is expected to exceed 40 km/sec. The probe has to survive the intense radiative heating during this high speed entry mission. For this purpose, the probe is normally coated with ablative heat shield materials. As the probe advances through the Jovian atmosphere the heat shield ablates and forms

*The numbers in brackets indicate references

a protective layer of cool gases around the probe and these are responsible mainly for absorbing the incoming radiation. For the Jovian entry probe, it has been estimated that the heat shield weight for thermal protection will be as much as 45 percent of the total weight of the probe. Since experimental facilities cannot adequately simulate the conditions expected during a Jovian entry mission, most of the required information must be obtained from theoretical studies. This is particularly true for investigating the extent of radiative heating to the entry body.

In order to assess the magnitude of radiative heating to the Jovian entry body (and its influence on convecting heating and other flow phenomena), it is essential to employ meaningful radiative transport models in analyzing the shock-layer flow phenomena. In formulating the transfer equations for radiating gases, it is normally assumed that the gas is in local thermodynamic equilibrium (LTE). With this assumption, the transfer equation is simplified significantly as the populations of the various atomic and molecular states are given by the equilibrium (Boltzmann) distribution. For a wide range of conditions encountered in high speed gas dynamics, the transitions to or from the excited energy states are primarily due to atomic and molecular collisional process (rather than radiative emission and absorption process). Under these conditions, the assumption of LTE is usually justified. There are situations, however, where this assumption cannot be justified and conditions of non-local thermodynamic equilibrium (NLTE) may exist. In a very strict sense, NLTE corresponds to the condition where population densities of various energy levels deviate from the equilibrium (Boltzmann) distribution. Quite often, it has been speculated that use

of a LTE radiative transport model may not be justified in a shock-heated plasma. This is because, for the combined conditions of high velocities, high temperatures and low densities, the probability of a radiative transition becomes comparable with the probability of corresponding collisional transitions [9]. Unless the gas is optically thick the emission of a photon is a process that is not balanced by its inverse. Consequently, the population distribution among the energy levels departs from that predicted by the Boltzmann equation. Only one transition in one atom, molecule or ion need be unbalanced in this way to invalidate the LTE assumption.

Most analyses available on the NLTE radiative heat transfer are limited to vibrationally excited infrared active diatomic and triatomic molecules [10-13]. This situation is encountered in some engineering and upper atmospheric studies. The radiative processes associated with the Jovian entry conditions, however, correspond to ultraviolet radiation and involve electronic transitions. Furthermore, the shock-layer gas consists of molecules and atoms as well as charged particles. Hence, the studies available on the NLTE radiative heat transfer are not particularly suitable for Jovian entry conditions. One particular study by Horton [14] estimates the importance of nonequilibrium radiation during a hypersonic entry into the Jupiter's atmosphere. It is concluded, in this study, that the NLTE effect depletes the ablation layer thickness. This leaves the ablative products more transparent and the absorption of radiation by these species is less than the equilibrium value. As a result, the net radiative heat flux to the probe surface is more under NLTE conditions. Although this conclusion is in general agreement with the kind of behavior expected in an ablation contaminated nonequilibrium

boundary layer flow, the analysis is not complete. It is important to remember that the NLTE phenomena is among the gas particules themselves rather than between the gas and the radiation field. Thus, essentially no study is available that treats the problem of NLTE radiative transfer under planetary entry conditions in a systematic manner.

Under NLTE, there are more particles in the higher energy levels than normally predicted by the equilibrium theory. This is because the particles take considerably longer time to establish a deexcitation collision in a nonequilibrium field. The over population of the excited energy levels leaves the unexcited levels under populated. As a direct consequence of this, the absorption pattern of the particles is not the same as the equilibrium absorption behavior (since a particle in an unexcited state is capable of absorbing more radiation than the one in an excited state). Hence, a more detailed analysis of the absorption cross section of these particles has to be made under both the LTE and NLTE conditions. The frequency dependent absorption coefficient for a nongray gas analysis may be treated either in detail or by a "step model". There are several methods available in the literature for detailed computation of the equilibrium absorption coefficient [15-17]. In a step model, the frequency dependence is broken into a number of discrete steps. Zoby et al. [18] developed a 58-step model for the hydrogen and helium mixture. For this case, a 30-step model developed by Tiwari and Subramanian [19] simplifies the analysis even further and the results compare well with the other two models under certain conditions. In general, the nonequilibrium absorption coefficient is obtained by multiplying the equilibrium values by a nonequilibrium factor. This factor is a function of the intensity of the incident radiation,

collisional relaxation time of the particle under investigation and the radiative lifetime of the excited state. It is, therefore, important to find an appropriate relation for this nonequilibrium factor for the Jovian entry conditions.

After evaluation of the spectral absorption coefficient, the next step is to develop an appropriate expression for spectral and total radiative heat fluxes. The expression for the total radiative transport involves integration over both the frequency spectrum and the physical space. In general, the problem of radiative exchange is a complex three dimensional phenomena. The inclusion of nonequilibrium formulation adds to this complexity with different chemical species at different energy levels. Hence, reasonable assumptions are required in order to obtain meaningful solutions of the transfer equation. In many physically realistic problems, the complexity of the three-dimensional radiative transfer can be reduced by introduction of the "tangent slab approximation". This approximation treats the gas layer as a one-dimensional slab in the calculation of radiative transport. Radiation in directions other than normal to either the body or shock is neglected. The methods for calculating the divergence of the radiative flux and other conservation equations are available in [20-22].

Another problem which arises directly from the radiative heating rates is the effect of shape change and mass loss on the flow field of a Jovian entry body. For exploratory missions to planets such as Mars and Venus, the levels of heating to the entry probe are not severe enough to change significantly the mass and shape of the probe. In contrast, the large radiative heating rates associated with Jovian entry results in massive ablation of the protective heat shield material as the probe

advances through the atmosphere [23]. This, in turn, results in different probe configurations at different stations along the entry trajectory. This change of shape can affect significantly the flow pattern and the heating rate distribution around the probe. Sutton et al. [24-26] have presented an inviscid flow-field analysis for investigating the effects of the recession of the heat shield caused by radiative heating to the Jupiter probe. The initial probe configurations considered were hyperboloids and spherecones. Important studies available on the effects of mass loss, shape change and real-gas aerodynamics of a Jovian atmospheric probe are discussed in a survey article by Walberg et al. [27]. It is clear from the review of this article that further studies are needed to investigate the effects of the shape changes on heating of the forebody and afterbody of different Jovian entry probes.

From the literature survey, it is clear that no work is available which considers the influence of non-local thermodynamic equilibrium radiative heating flow phenomena around a Jovian entry body. A few available studies are either inappropriate or provide very little information for nonequilibrium analysis under Jovian entry conditions. The presence of different ablative species further complicates the nonequilibrium analysis. For a correct NLTE analysis, it is essential to consider the various excitation and deexcitation probabilities of all important species in the shock layer. It is important to realize that through an entirely different temperature distribution, the NLTE radiative transfer influences significantly the convective heating rate as well as other flow properties in the shock layer. Since an accurate determination of the total heating rate is essential for the design of the heat shield and for assessing the survival of the entry probe, it is necessary to

investigate the extent of NLTE influence on the entire shock-layer flow phenomena in a systematic manner.

The primary objectives of this study, therefore, are two-fold: First to investigate the influence of NLTE radiative transfer; and then to determine the effects of changes in probe configurations on the entire shock-layer flow phenomena. To accomplish this in a systematic manner, the present study is divided into four major areas: (1) Significance of radiation models on the flow-field solutions, (2) Influence of NLTE radiation without ablation injection, (3) Importance of NLTE radiation with ablation injection, and (4) Effect of probe shape change on the flow phenomena.

The basic formulation of the entire problem considered for the present study is given in Chapter 2. Discussions on the radiative transfer equations, radiation absorption models, and radiative flux equations (for both the LTE and NLTE conditions) are presented in Chapter 3. Information on collisional relaxation times and radiative lifetimes of different species (in their appropriate states) are presented in Chapter 4. Thermodynamic and transport properties for each species considered in the shock layer are given in Chapter 5. Solution procedures for the NLTE radiative flux equations and other shock-layer equations are presented in Chapter 6. The entire results of the study are discussed in Chapter 7.

2. BASIC FORMULATION

The physical model and coordinate system for a Jovian entry body are shown in Fig. 1a. In this figure, s is the distance measured along the body surface and n is the distance normal to the body surface. The flow in the shock layer is considered to be axisymmetric, steady, radiating and in chemical equilibrium. Both inviscid as well as viscous shock-layer analyses are considered in the present study. The basic governing equations (along with the appropriate boundary conditions) are presented in this chapter.

2.1 Inviscid Flow Equations

For the physical model considered, the governing equations for inviscid flow are expressed as [28, 29]

Continuity:

$$(\partial/\partial s) [(r+n \cos \theta)\rho u] + (\partial/\partial n) (\Gamma \zeta \rho v) = 0 \quad (2.1)$$

s-momentum:

$$(u/\Gamma) (\partial u/\partial s) + v (\partial u/\partial n) + uv\kappa/\Gamma + (1/\rho\Gamma) (\partial p/\partial s) = 0 \quad (2.2)$$

n-momentum:

$$(u/\Gamma) (\partial v/\partial s) + v (\partial v/\partial n) - u^2\kappa/\Gamma + \rho^{-1} (\partial p/\partial y) = 0 \quad (2.3)$$

Energy:

$$\begin{aligned} (u/\Gamma) (\partial h/\partial s) + v (\partial h/\partial n) - (u/\rho\Gamma) (\partial p/\partial s) - (v/\rho) (\partial p/\partial n) \\ + (1/\rho) (\text{div } q_R) = 0 \end{aligned} \quad (2.4)$$

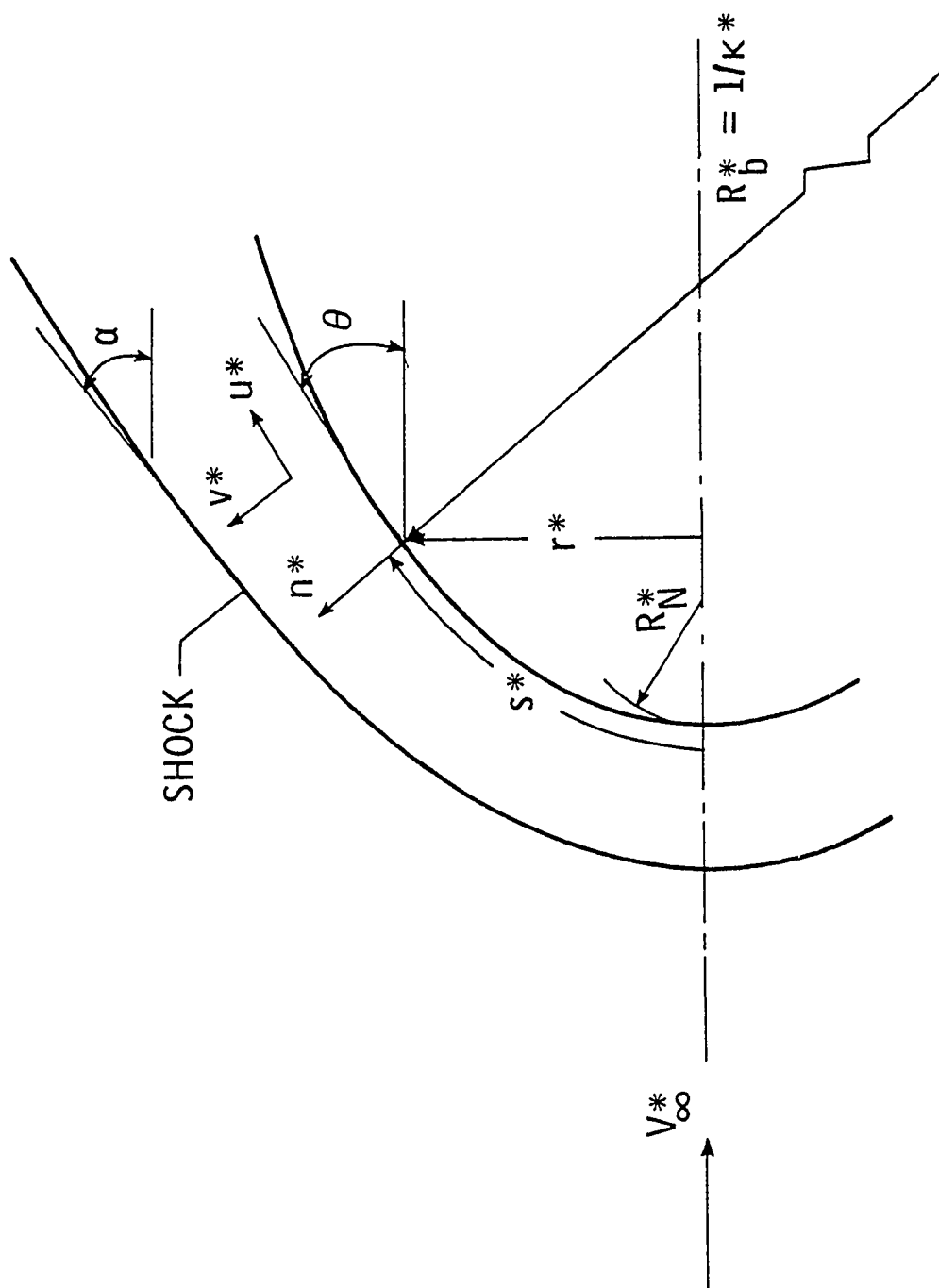


Fig. 1a Physical model and coordinate system

where

$$\Gamma = 1 + n\kappa$$

$$\text{div } q_R = (\partial q_R / \partial n) + q_R (\kappa / \Gamma + \cos \theta / r)$$

It should be noted that the above equations are written in nondimensional form. The quantities used to nondimensionalize these equations are defined as:

$$\begin{aligned} s &= s^* / R_N^* & n &= n^* / R_N^* & u &= u^* / V_\infty^* \\ \rho &= \rho^* / \rho_\infty^* & p &= p^* / (\rho_\infty^* V_\infty^{*2}) & h &= h^* / V_\infty^{*2} \\ r &= r^* / R_N^* & q_R &= q_R^* / (\rho_\infty^* V_\infty^{*3}) & \kappa &= \kappa^* / R_N^* \end{aligned} \quad (2.5)$$

2.2 Viscous Flow Equations

Basic governing equations for viscous shock layer are obtained from the steady-state Navier-Stokes equations by keeping terms up to second order in the inverse square root of the Reynolds number, ϵ , as [5,30]

Continuity:

$$(\partial / \partial s) [(r+n \cos \theta) u] + (\partial / \partial n) (\Gamma \zeta \rho v) = 0 \quad (2.6)$$

s-momentum:

$$\begin{aligned} \rho [(u/\Gamma) (\partial u / \partial s) + v (\partial u / \partial n) + uv\kappa/\Gamma] + \Gamma^{-1} (\partial p / \partial s) \\ = \epsilon^2 [(\partial / \partial n) (\partial \psi) + \mu (2\kappa/\Gamma + \cos \theta / \zeta) \psi] \end{aligned} \quad (2.7)$$

n-momentum:

$$\rho [(u/\Gamma) (\partial v / \partial s) + v (\partial v / \partial n) - u^2 \kappa / \Gamma] + \partial p / \partial n = 0 \quad (2.8)$$

Energy:

$$\begin{aligned}
 & \rho[(u/\Gamma) (\partial H/\partial s) + v (\partial H/\partial n)] - v \partial p/\partial n + \rho u^2 v \kappa/\Gamma \\
 & = \epsilon^2 [\partial/\partial n (\Phi_1 + \Phi_2)] \\
 & - [\partial q_R/\partial n + q_R (\kappa/\Gamma + \cos \theta/r)] \quad (2.9)
 \end{aligned}$$

where

$$\Psi = \partial u/\partial n - u\kappa/\Gamma$$

$$\begin{aligned}
 \Phi_1 = & \mu/Pr (\partial H/\partial n) - \mu/Pr \sum_{i=1}^{N_S} h_i (\partial c_i/\partial n) - \sum_{i=1}^{N_S} h_i J_i \\
 & + \mu/Pr (Pr - 1) u (\partial u/\partial n) - \mu \kappa u^2/\Gamma \quad (2.9a)
 \end{aligned}$$

$$\begin{aligned}
 \Phi_2 = & [(\kappa/\Gamma) + \cos \theta/(r + n \cos \theta)] [\mu/Pr (\partial H/\partial n) \\
 & - \mu/Pr \sum_{i=1}^{N_S} h_i (\partial c_i/\partial n) - \sum_{i=1}^{N_S} h_i J_i \\
 & + \mu/Pr (Pr-1) u \partial u/\partial n - \mu \kappa u^2/\Gamma] \quad (2.9b)
 \end{aligned}$$

In the preceding equations, the total enthalpy $H = (u^2 + v^2)/2 + h$ and J_i is the mass flux relative to the mass velocity and is given by [31,32]

$$J_i = -(\mu/Pr) Le (\partial c_i/\partial n) \quad (2.10)$$

In Eq. (2.10) Le represents the multicomponent Lewis number and, in the present analysis, is taken to be a constant for all species as 1.10. In addition to the quantities given in Eq. (2.5), the terms used to nondimensionalize the above set of viscous equations are

$$\begin{aligned}
Pr &= \mu^* C_p^* / k^* & Le &= \rho^* C_p^* D_{ij}^* / k^* & \mu &= \mu^* / \mu_{Ref}^* \\
k &= k^* / (\mu_{Ref}^* C_{p,\infty}^*) & C_p &= C_p^* / C_{p,\infty}^* & \mu_{Ref}^* &= \bar{\mu}^* (V_\infty^* / C_{p,\infty}^*) \\
J_i &= J_i^* R_N^* / \mu_{Ref}^* & \varepsilon &= [\mu_{Ref}^* / (\rho^* V_\infty^* R_N^*)]^{1/2}
\end{aligned} \tag{2.11}$$

In addition to the preceding set of equations for the inviscid and viscous shock-layer flow, the species continuity equation and equation of state are needed to complete the set of equations. The species continuity is given by the expression

$$\rho[(u/\Gamma) (\partial C_i / \partial s) + v (\partial C_i / \partial n)] = (\varepsilon^2 / \Gamma \zeta) [(\partial / \partial n) (\Gamma \zeta J_i)] \tag{2.12}$$

where

$$\zeta = r + n \cos \theta \tag{2.12}$$

The equation of state for the gas, in general, can be expressed as

$$p = \rho T (R^* / M^* C_{p,\infty}) \tag{2.13}$$

where $C_{p,\infty}$ represents the specific heat of the gas at the free-stream conditions. The expression for the equation of state for a hydrogen/helium mixture is given by Zoby et al. as [33]

$$T^* = C_T [(p^* / 1013250)^l / (\rho^* / 0.001292)^k] \tag{2.14}$$

$$H^* = C_H [(p^* / 1013250)^m / (\rho^* / 0.001292)^n] (R^* T_0^* / M^*) \tag{2.14a}$$

where

$$k = 0.65206 - 0.04407 \ln(X_{H_2})$$

$$l = 0.67389 - 0.04637 \ln(X_{H_2})$$

$$m = 0.95252 - 0.1447 \ln(X_{H_2})$$

$$n = 0.97556 - 0.16149 \ln(X_{H_2})$$

$$U_t = V_\infty \sin \theta [1 + 0.7476(1-X_{H_2})]$$

$$CTU = -545.37 + 61.608 U_t - 22459 U_t^2 + 0.039922 U_t^3 \\ - 0.00035148 U_t^4 + 0.0000012361 U_t^5$$

$$CHU = 5.6611 - 0.52661 U_t^2 + 0.020376 U_t^3 - 0.00037861 U_t^4 \\ + 0.0000034265 U_t^5 - 0.000000012206 U_t^6$$

$$C_T = CTU + 61.2 (1-X_{H_2})$$

$$C_H = CHU - 0.3167 (1-X_{H_2})$$

and H_{X_2} represents the mole fraction of H_2 .

2.3 Free-Stream and Boundary Conditions

The Jupiter atmosphere mainly consists of hydrogen and helium gases. In the past, the nominal composition of the atmosphere was assumed to be 85 percent hydrogen and 15 percent helium [34]. For different entry times and altitudes, the free stream conditions are different. The values used in the present study at different altitudes are given in Table I. The free-stream enthalpy can be calculated by the relation [35]

$$H_\infty = 1.527 RT_\infty \quad (2.15)$$

where $R = 8.135$ Joules/K-mole, is the universal gas constant. The number density of hydrogen can be calculated by the ideal gas law and the relation can be given as

Table 1. Free-stream conditions for Jovian entry.

Altitude Z, km	Velocity $V_{\infty}^*, \text{km/sec}$	Density $\rho_{\infty}^*, \text{kg/m}^3$	Pressure $p_{\infty}^*, \text{N/m}^2$	Temperature T_{∞}^*, K
109	35.207	7.197E-4	443.02	163.72
116	39.09	4.360E-4	245.00	166.91
138	44.04	2.127E-4	132.00	167.02

$$N_{H_2} = (7.243117 \times 10^{22}) (P_\infty/T_\infty) X_{H_2} \quad (2.16)$$

where X_{H_2} is the mole fraction of H_2 .

In order to solve the set of governing equations given in Secs. 2.1 and 2.2, it is essential to specify appropriate boundary conditions at the body surface and shock interface. In all cases, the boundary conditions immediately behind the shock wave are calculated by using the Rankine - Hugoniot relations. In the viscous analysis, the no-slip and no-temperature-jump boundary conditions are used. Consequently, the velocities at the surface are

$$u(o,n) = u_w = 0 \quad (2.17)$$

$$v(o,n) = v_w = 0 \quad (2.18)$$

The boundary condition given by Eq. (2.18) is valid only for the case with no mass injection. For this case, the temperature at the wall is usually specified as

$$T_w = \text{const.} \quad (2.19)$$

For the case of ablation mass injection, the wall temperature is either specified or calculated. For the calculated wall temperature conditions, the wall temperature is the sublimation temperature of the ablator surface. Moreover, the ablation process is assumed to be quasi-steady. With these assumptions, the expressions for the coupled mass injection rate and the sublimation temperature (for the carbon-phenolic heat shield material considered in this study) are given by

$$\dot{m} = [(-q_{C,w}^* - q_{R,w}^*) / \sum_{i=1}^{N_s} (C_i h_i^*)_w - h_A^*] / (\rho_\infty^* V_\infty^*) \quad (2.20)$$

$$\begin{aligned}
T_{\text{Sub}}^* = & \sum_{j=1}^5 \lambda_{1,j} C_A^{j-1} + \log p_w^* \sum_{j=1}^5 \lambda_{2,j} C_A^{j-1} \\
& + \log p_w^* \sum_{j=1}^5 \lambda_{3,j} C_A^{j-1}
\end{aligned} \quad (2.21)$$

where p_w^* is the wall pressure in atmospheres and C_A is the ablator mass fraction at the wall. The $\lambda_{i,j}$ coefficients whose values are given in [8, 64-67] are applicable for a free-stream gas composition of 89 percent hydrogen and 11 percent helium by mole fraction and for ablator mass fractions of 0.4 to 1.0. If the ablator mass fraction at the wall is unity, then these coefficients are valid for any free-stream gas mixture. For ablation injection, the elemental concentrations at the wall are governed by convection and diffusion and are given by

$$(\partial c_i / \partial n)_w - 1/\epsilon^2 (mSc/\mu)_w [(c_i)_w - (c_i)_-] = 0 \quad (2.22)$$

where Sc is the Schmidt number ($Sc = Pr/Le$) and $(c_i)_-$ is the elemental mass fraction of the solid ablator material at the surface.

The heat transferred to the wall due to conduction and mass diffusion is referred to as the convective heat flux and is given by the expression

$$-q_{c,w} = \epsilon^2 (k \partial T / \partial n + \mu / Sc \sum_{i=1}^{N_s} h_i (\partial c_i / \partial n)_w) \quad (2.23)$$

The radiative flux emitted from the wall is given by the relation

$$q_R^+(0) = q_{R,w}^+ = \epsilon_w \sigma T^{*4} \quad (2.24)$$

A value of surface emittance $\epsilon_w = 0.8$ is used in this study.

3. RADIATIVE TRANSPORT MODELS

An appropriate expression for the radiative flux q_R is needed for the solution of the energy equation presented in the previous chapter. This requires a suitable radiative transport model and a meaningful spectral model for variation of the absorption coefficient of the gas. In this Chapter appropriate expressions for the spectral and total radiative flux are given, and a detailed discussion on models for the spectral absorption by the hydrogen-helium gas and other important ablative species in the shock layer is presented.

3.1 Radiative Flux Equations

The equations for radiative transport, in general, are integral equations which involve integration over both frequency spectrum and physical coordinates. In many physically realistic problems, the complexity of the three dimensional radiative transfer can be reduced by introduction of the "tangent slab approximation". This approximation treats the gas layer as a one dimensional slab in calculation of the radiative transport. Radiation in directions other than normal to either the body or shock is neglected in comparison. Discussions on the validity of this approximation for planetary entry conditions are given in [36-39]. The tangent slab approximation is employed in this study. It should be pointed out here that this approximation is used only for the radiative transport calculations and not for other flow variables.

3.1.1 LTE Radiative Flux Equations

For the present study, the equations of radiative transport are obtained for a gas confined between two infinite, parallel boundaries, the shock wave, and the body. This is shown in Fig. 1b. For one-dimensional radiation, the equations of transfer for a nonscattering medium in local thermodynamic equilibrium are given by [20,21]

$$\mu(dI_{\nu}^{+}/d\tau_{\nu}) = B_{\nu}(\tau_{\nu}) - I_{\nu}^{+} \quad (3.1a)$$

$$\mu(dI_{\nu}^{-}/d\tau_{\nu}) = B_{\nu}(\tau_{\nu}) - I_{\nu}^{-} \quad (3.1b)$$

where

$$\mu = \cos \theta \quad (3.2a)$$

$$\tau_{\nu} = \int_0^n \kappa_{\nu}(n) \, dn \quad (3.2b)$$

$$\tau_{0\nu} = \int_0^{n_s} \kappa_{\nu}(n) \, dn \quad (3.2c)$$

In the above equation, κ_{ν} and B_{ν} represent the frequency-dependent linear absorption coefficient and Planck function, respectively.

Furthermore, it should be noted that I_{ν}^{+} and I_{ν}^{-} correspond to positive and negative values of μ respectively. The boundary conditions for Eqs. (3.1a) and (3.1b) can be expressed as

$$I_{\nu}^{+}(\tau_{\nu}, \mu) = I_{\nu}^{+}(0, \mu), \quad \tau_{\nu} = 0 \quad (3.3a)$$

$$I_{\nu}^{-}(\tau_{\nu}, \mu) = I_{\nu}^{-}(\tau_{0\nu}, \mu), \quad \tau_{\nu} = \tau_{0\nu} \quad (3.3b)$$

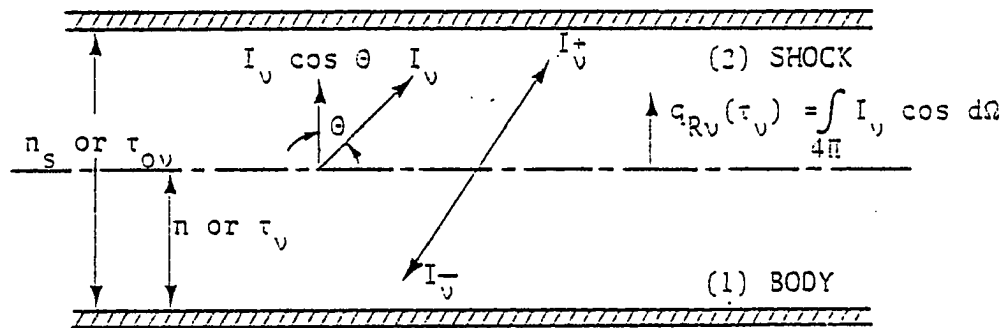


Fig. 1b Physical model and coordinate system for the radiation field.

By employing the above conditions, integration of Eqs. (3.1a) and (3.1b) results in

$$I_{\nu}^{+}(\tau_{\nu}, \mu) = I_{\nu}^{+}(0, \mu) \exp(-\tau_{\nu}/\mu) + \int_0^{\tau_{\nu}} B(t) \times \exp[-(\tau_{\nu} - t)/\mu] \mu^{-1} dt \quad (3.4a)$$

$$I_{\nu}^{-}(\tau_{\nu}, \mu) = I_{\nu}^{-}(\tau_{0\nu}, \mu) \exp[-(\tau_{0\nu} - \tau_{\nu})/\mu] - \int_{\tau_{\nu}}^{\tau_{0\nu}} B_{\nu}(t) \exp[-(t - \tau_{\nu})/\mu] \mu^{-1} dt \quad (3.4b)$$

Equations (3.4a) and (3.4b) describe the radiation field in terms of the temperature field within the medium. The temperature field is expressed by the Planck function. The term $I_{\nu}^{+}(0, \mu) \exp(-\tau_{\nu}/\mu)$ in Eq. (3.4a) represents the radiant energy that originated at the body surface which has been attenuated by the factor $\exp(-\tau_{\nu}/\mu)$ as a result of absorption. The integral term represents the augmentation of I_{ν}^{+} due to gaseous emission. A similar explanation goes for Eq. (3.4b), with respect to the shock surface.

Referring to Fig. 1b, the spectral radiative flux is expressed in terms of intensity of radiation as [21]

$$q_{R\nu}(\tau_{\nu}) = \int_{4\pi} I_{\nu} \cos \theta \, d\Omega = 2\pi \int_{-1}^1 I_{\nu}(\tau_{\nu}, \mu) \mu \, d\mu \quad (3.5)$$

By noting that I_{ν}^{+} and I_{ν}^{-} correspond to positive and negative values of μ , Eq. (3.5) can be expressed as

$$q_{R\nu}(\tau_{\nu}) = 2\pi \int_0^1 I_{\nu}^{+} \mu \, d\mu - 2\pi \int_0^{-1} I_{\nu}^{-} \mu \, d\mu \quad (3.6)$$

The substitution of values for I_{ν}^{+} and I_{ν}^{-} from Eqs. (3.4a) and (3.4b) into Eq. (3.6) results in the one-dimensional expression for spectral radiative flux as [21].

$$q_{R\nu}(\tau_{\nu}) = 2\pi \left\{ \int_0^1 I_{\nu}^{+}(0, \mu) e^{-\tau_{\nu}/\mu} + \int_0^{\tau_{\nu}} B_{\nu}(t) E_2(\tau_{\nu} - t) dt \right. \\ \left. - \left[\int_0^1 I_{\nu}^{-}(\tau_{0\nu}, -\mu) e^{-(\tau_{0\nu} - \tau_{\nu})/\mu} \mu d\mu + \int_{\tau_{\nu}}^{\tau_{0\nu}} B_{\nu}(t) E_2(t - \tau_{\nu}) dt \right] \right\} \quad (3.7)$$

where $E_n(t)$ is the exponential integral function defined by

$$E_n(t) = \int_0^1 \mu^{n-2} e^{-t/\mu} d\mu \quad (3.8)$$

The expression for the net radiative flux at any location is given by

$$q_R(n) = \int_0^{\infty} q_{R\nu}(\tau_{\nu}) d\nu \quad (3.9)$$

Often, it is desirable to obtain separate relations for total radiative flux going towards the body and the bow shock. Upon denoting the radiative flux towards the shock by q_R^{+} and towards the body by q_R^{-} , Eq. (3.9) can be written as

$$q_R(n) = q_R^{+}(n) - q_R^{-}(n) = \int_0^{\infty} q_{R\nu}^{+}(\tau_{\nu}) d\nu - \int_0^{\infty} q_{R\nu}^{-}(\tau_{\nu}) d\nu \quad (3.10)$$

where

$$q_{Rv}^+ = 2\Pi \int_0^\infty \left[\int_0^1 I_v^+(0, \mu) e^{-\tau_v/\mu} \mu d\mu + \int_0^{\tau_v} B_v(t) \cdot E_2(\tau_v - t) dt dv \right] \quad (3.11a)$$

$$q_{Rv}^- = 2\Pi \int_0^\infty \left[\int_0^1 I_v^-(\tau_{ov}, -\mu) e^{-(\tau_{ov} - \tau_v)/\mu} \mu d\mu + \int_{\tau_v}^{\tau_{ov}} B_v(t) E_2(t - \tau_v) dt \right] dv \quad (3.11b)$$

For diffuse surfaces, $I_v^+(0, \mu)$ and $I_v^-(\tau_{ov}, \mu)$ are independent of direction (i.e., independent of μ) and may be expressed in terms of surface radiosities B_{1v} and B_{2v} as

$$\Pi I_v^+(0, \mu) = B_{1v}, \quad \Pi I_v^-(\tau_{ov}, \mu) = B_{2v}$$

Hence, Eqs. (3.11a) and (3.11b) are expressed as

$$q_v^+(n) = 2 \int_0^\infty [B_{1v} E_3(\tau_v) + \Pi \int_0^{\tau_v} B_v(t) E_2(\tau_v - t) dt] dv \quad (3.12)$$

$$q_v^-(n) = 2 \int_0^\infty [B_{2v} E_3(\tau_{ov} - \tau_v) + \Pi \int_{\tau_v}^{\tau_{ov}} B_v(t) E_2(t - \tau_v) dt] dv \quad (3.13)$$

The expressions for surface radiosities appearing in this equation are given by [21]

$$B_{1v} = \epsilon_{1v} [\Pi B_v(T_w)] + 2 \rho_{1v} [B_{2v} E_3(\tau_{ov}) + \int_0^{\tau_{ov}} \Pi B_v(t) E_2(t) dt] \quad (3.14a)$$

$$B_{2v} = \epsilon_{2v} [\Pi B_v(T_s)] + 2 \rho_{2v} [B_{1v} E_3(\tau_{ov}) + \int_0^{\tau_{ov}} \Pi B_v(t) \cdot E_2(\tau_{ov} - t) dt] \quad (3.14b)$$

where ρ_{1v} and ρ_{2v} represent the surface reflectance of the body and the shock respectively. For nonreflecting surfaces, $\rho_{1v} = \rho_{2v} = 0$, and Eqs. (3.14a) and (3.14b) reduce to

$$B_{1v} = \Pi \epsilon_{1v} B_v(T_w), B_{2v} = \Pi \epsilon_{2v} B_v(T_s) \quad (3.15)$$

Sometimes, it is convenient to express the radiative flux equations in terms of gas emissivities, defined by

$$\epsilon_v^+ = 1 - 2E_3(\tau_v - t), \epsilon_v^- = 1 - 2E_3(t - \tau_v) \quad (3.16)$$

By noting that

$$d\epsilon_v^+ = -2E_2(\tau_v - t) dt, d\epsilon_v^- = 2E_2(t - \tau_v) dt$$

$$\epsilon_v^+(t = 0) = 1 - 2E_3(\tau_v) = \epsilon_b^+ = \epsilon_w^+$$

$$\epsilon_v^+(t = \tau_v) = 1 - 2E_3(0) = 1 - 2\left(\frac{1}{2}\right) = 0 = \epsilon_v^-(t = \tau_v)$$

$$\epsilon_v^-(t = \tau_{ov}) = 1 - 2E_3(\tau_{ov} - \tau_v) = \epsilon_b^- = \epsilon_s^-$$

Eqs. (3.13a) and (3.13b) can be written as

$$q_R^+(n) = \int_0^\infty [2B_{1v} E_3(\tau_v) + \Pi \int_0^{\epsilon_w^+} B_v(\epsilon_v^+) d\epsilon_v^+] dv \quad (3.17a)$$

$$q_R^-(n) = \int_0^\infty [2B_{2v} E_3(\tau_{ov} - \tau_v) + \Pi \int_0^{\epsilon_s^-} B_v(\epsilon_v^-) d\epsilon_v^-] dv \quad (3.17b)$$

If the radiative flux into the slab at the boundaries is neglected, then the first term on the right of Eqs. (3.17a) and (3.17b) vanishes and the net radiative flux is given by

$$q_R(n) = \Pi \int_0^\infty \left[\int_0^{\epsilon_w^+} B_\nu(\epsilon_\nu^+) d\epsilon_\nu^+ - \int_0^{\epsilon_s^-} B_\nu(\epsilon_\nu^-) d\epsilon_\nu^- \right] d\nu \quad (3.18)$$

Depending upon the particular assumptions made in a physical problem, use is made of either Eqs. (3.13a) and (3.13b), (3.17a) and (3.17b), or Eq. (3.18) in obtaining the net radiative heat flux.

For mathematical convenience, exponential integrals often are approximated by appropriate exponential functions. There are a few standard procedures for doing this, and these are discussed in [20,21]. It has been demonstrated (see Ref. 21, for example) that when the exponential integral of third order is approximated by

$$2E_3(z) = \exp(-2z) \quad (3.19)$$

the radiative transport solutions are exact in the optically thin limit, and of satisfactory accuracy in the optically thick limit. By using Eq. (3.19), approximate expressions for the gas emissivities are obtained from Eq. (3.16) as

$$\epsilon_\nu^+ = 1 - \exp[2(t - \tau_\nu)] \quad (3.20a)$$

$$\epsilon_\nu^- = 1 - \exp[2(\tau_\nu - t)] \quad (3.20b)$$

Since $E_n(z) = -E_{n-1}(z)$, one could obtain the relation for the exponential integral of second order by differentiating Eq. (3.19) as

$$E_2(z) = \exp(-2z) \quad (3.21)$$

Use of Eqs. (3.19) and (3.21) could be made directly in Eqs. (3.10), (3.11a) and (3.11b) to obtain appropriate relations for the radiative heat flux.

In this study, use of the exponential kernel approximation, as given by Eqs. (3.19) and (3.21), is made for the radiative transport in the shock layer. Furthermore, the bow shock is considered transparent, and the free stream is considered cold and transparent. For the evaluation of the equilibrium spectral radiative flux, use of Eqs. (3.13a) and (3.13b) are made in the present analysis.

3.1.2 NLTE Radiative Flux Equations

In the previous section, the transfer equation and the resulting radiative flux equations were obtained under the condition of local thermodynamic equilibrium. For this situation distribution of the molecules in the various energy levels are collision dominated and the emission process depends on the local equilibrium temperature alone. The treatment outlined in obtaining these equations are of macroscopic nature. The non-local thermodynamic equilibrium situation, on the other hand, involves a study of the individual molecules of the radiating system since these particles do not obey the equilibrium Boltzmann distribution. The derivation of the NLTE transfer equation employs a quantum mechanics treatment. The equation of radiative transfer, in general, may be expressed in terms of Einstein coefficients A_{nm} , B_{nm} , and B_{mn} as [20,40].

$$dI_v/dn = \rho \bar{\kappa}_v [1 - N_n/N_m] (B_{nm}/B_{mn})] \\ \times A_{nm} [B_{mn} \left\{ (N_m/N_n) (B_{mn}/B_{nm}) - 1 \right\} - I_v]$$

where N_n represents the number density of the n th level, B_{mn} is the Einstein coefficient for absorption, B_{nm} is the Einstein coefficient for stimulated emission, and A_{nm} is the Einstein coefficient for spontaneous emission. The above equation can be written in a simplified form as

$$dI_\nu/dn = \rho\kappa_\nu(J_\nu - I_\nu) \quad (3.23)$$

where J_ν is the NLTE source function and κ_ν is the reduced absorption coefficient which includes the effect of induced emission (negative absorption) in the medium and is defined as

$$\kappa_\nu = \bar{\kappa}_\nu [1 - (N_n/N_m) (B_{nm}/B_{mn})] \quad (3.24)$$

In this equation $\bar{\kappa}_\nu$ is the equilibrium absorption coefficient. The NLTE source function is given in terms of the population ratio as

$$J_\nu = A_{nm} / \left\{ B_{nm} [(N_m/N_n) (B_{mn}/B_{nm}) - 1] \right\} \quad (3.25)$$

By making use of the relations between the Einstein coefficients, the source function can be expressed as [14,20,40,41]

$$J_\nu = (2h\nu^3/c^2) / [(N_m/N_n) (g_n/g_m) - 1] \quad (3.26)$$

where

$$A_{nm} = (2h\nu^3/c^2) B_{nm} \quad (3.27a)$$

$$B_{nm} = (g_m/g_n) B_{mn} \quad (3.27b)$$

In this equation h represents the Planck constant and g_m and g_n are corresponding statistical weight factors for the lower and upper

energy levels (different for different species), which are assumed to be unity in the present analysis.

From Eqs. (3.24) and (3.26), it is evident that the state population ratio, N_m/N_n , has to be known in order to evaluate the nonequilibrium absorption coefficient and NLTE source function. This is achieved by the method of detailed balancing of various transition processes. The three processes involved in the steady-state detailed balancing are the induced absorption, induced emission, and spontaneous (stimulated) emission. In the induced absorption process a quantum of radiation of appropriate energy and frequency is absorbed, and this results in exciting an atom (or molecule). In the induced emission, a quantum of radiation interacts with an excited particle to give emission of another quantum of the same energy, and thereby the particle reverts to the lower energy state. In the spontaneous emission case, an excited particle spontaneously emits a quantum of radiation of the appropriate frequency and reverts to a lower energy state. These processes may be expressed as



where M^* denotes the excited state of the species M . The statistical steady-state equation for a particular electronic state is given by

$$dN_1/dt = 0$$

This implies that the sums of the radiative and collisional rates into and out of the state 1 must be equal. By employing this criterion, the

state population ratio for any two levels, in a multilevel system consisting of k levels, is expressed as [10]

$$N_m/N_n = \left(\sum_k P_{nk} Q_{km,n} / \sum_k P_{mk} Q_{kn,m} \right) \quad (3.29)$$

where P_{nk} is the sum of the radiative term A_{nk} and the collision term C_{nk} . The quantity $Q_{km,n}$ is the probability for all transitions from level k to m not involving n such that for $k = m$, $Q_{kk,n} = 1$.

Upon combining Eqs. (3.26) and (3.29), the source function for the transition between levels n and m (containing k intermediate levels) is given by [42]

$$J_\nu = \frac{\int_{\Delta\nu} I_\nu^* \phi_\nu d\nu + \epsilon^* + \theta^*}{1 + \epsilon^* + \eta^* - \delta\theta} \quad (3.30)$$

where

$$\theta = 1/B_{mn} \sum_{\substack{\ell=1 \\ \ell \neq n,m}}^k P_{m\ell} Q_{\ell n,m} \quad (3.31a)$$

$$\eta^* = 1/A_{nm} \sum_{\substack{\ell=1 \\ \ell \neq n,m}}^k P_{n\ell} Q_{\ell m,n} \quad (3.31b)$$

$$\epsilon^* = C_{nm}/[B_{mn} B_\nu(T)] \quad (3.31c)$$

$$\delta = c^2/2h\nu^3, I_\nu^* = I_\nu/B_\nu(T), \theta^* = \theta/B_\nu(T) \quad (3.32)$$

Equations (3.29) and (3.30) simplifies considerably if the level of transitions involved are less. For example, in a three-level transition the relation for the population ratio N_0/N_1 is obtained from Eq. (3.29)

as

$$\frac{N_0}{N_1} = \frac{A_{10} + B_{10} \bar{I}_{\Delta\nu} + C_{10} + C_{20} (B_{12} \bar{I}_{\Delta\nu} + C_{12})/Q_T}{B_{01} \bar{I}_{\Delta\nu} + C_{01} + C_{02} (A_{21} + C_{21} + B_{21} \bar{I}_{\Delta\nu})/Q_T} \quad (3.33)$$

In this equation, Q_T represents the total probability for transitions from level 2 (i.e., from the third level) and is given by

$$Q_T = A_{21} + B_{21} \bar{I}_{\Delta\nu} + C_{21} + C_{20} \quad (3.34)$$

It can be shown easily that, under equilibrium conditions, Eqs. (3.33) reduces to the Boltzmann distribution as

$$N_0/N_1 = \exp(\Delta E/kT) \quad (3.35)$$

where $\Delta E = E_1 - E_0$ is the difference of energy (in eV) between levels 1 and 0.

Upon combining Eqs. (3.26) and (3.33), a simplified expression for the source function is obtained as [43]

$$J_\nu = \left\{ (2h\nu^3/c^2) / [\exp(h\nu/kT) - 1] \right\} \times [1 + \eta \bar{I}_{\Delta\nu} / \bar{B}_{\Delta\nu} + \delta_1] / (1 + \eta + \delta_2) \quad (3.36)$$

where

$$\bar{B}_{\Delta\nu} = 4\pi \int_{\Delta\nu} B_\nu d\nu \quad (3.37)$$

$$\delta_1 = C_{02} (A_{21} + C_{21} + B_{21} \bar{I}_{\Delta\nu}) / (B_{01} Q_T) \quad (3.38a)$$

$$\delta_2 = [C_{20} (B_{12} \bar{I}_{\Delta\nu} + C_{12}) - C_{02} (A_{21} + C_{21} + B_{21} \bar{I}_{\Delta\nu})] / (A_{10} Q_T) \quad (3.38b)$$

In the preceding equations, $\eta = A_{10}/C_{10}$ represents the ratio of the collisional deactivation (or relaxation) time and radiative lifetime of the first excited state, and quantities δ_1 and δ_2 are the influence factors on the NLTE source function arising from the higher level energy transitions.

For a two-level transition, the expression for the source function, as given by Eq. (3.36), further simplifies as [12,44]

$$J_\nu = B_\nu - \eta \left[\int_{\Delta\nu} (dq_R/dy) d\nu \right] / 4\pi \int_{\Delta\nu} \kappa_\nu d\nu \quad (3.39)$$

It is evident from the above equation as well as Eq. (3.36) that the degree of NLTE depends upon the magnitude of the quantities η , δ_1 and δ_2 . Since values of δ_1 and δ_2 are always lower than η for all particles involving multilevel energy transitions, the extent of nonequilibrium is characterized essentially by the parameter η . This implies that the major contribution to the source function comes from the transitions (collisional as well as radiative) involving the ground state and the first excited state. Consequently, for $\eta \ll 1$, the source function becomes the Planck function, and the assumption of LTE is justified. In this case, the collisional process is sufficiently fast to deexcite the particles to the lower state before deexcitation takes place by the emission of radiation. On the other hand, the condition of radiative equilibrium is reached for $\eta \gg 1$, and in this case the entire process of excitation and deexcitation is radiatively controlled. The NLTE radiation becomes important for conditions where $\eta = 0(1)$. By theoretical considerations, Jefferies [10] has established that the value of $\delta_{1,2}/\eta$ is approximately 0.1 for most gases involving multilevel energy transitions. Use of Eq. (3.36) is made in evaluating the

nonequilibrium source function when no ablation mass injection is considered in the study. With ablation injection in the shock-layer, Eq. (3.39) is used for the evaluation of J_ν to simplify the analysis.

To find the expression for the NLTE spectral radiative flux, the procedure outlined in the previous section, under the LTE conditions (Eqs. 3.5 - 3.18), are applicable in general. However, in this case the NLTE transfer equation, given by Eq. (3.23), is integrated between the two parallel boundaries (the body and the shock). The formal solution of Eq. (3.23) is given by [21]

$$q_{R\nu}(\tau_\nu) = 2 \left\{ B_{1\nu} E_3(\tau_\nu) + \int_0^{\tau_\nu} J_\nu(t) E_2(\tau_\nu - t) dt - [B_{2\nu} E_3(\tau_{0\nu} - \tau_\nu) + \Pi \int_{\tau_\nu}^{\tau_{0\nu}} J_\nu(t) E_2(t - \tau_\nu) dt] \right\} \quad (3.40)$$

where τ_ν is the nonequilibrium optical thickness and is given in terms of the nonequilibrium absorption coefficient κ_ν^* as

$$\tau_\nu = \int_0^n \kappa_\nu^*(n) dn \quad (3.41)$$

Following Eq. (3.10), the total radiative flux may be divided into two components as q_R^+ going towards the shock and q_R^- going towards the body. Thus Eq. (3.40) is rewritten as

$$q_R^+(n) = 2 \int_0^\infty [B_{1\nu} E_3(\tau_\nu) + \Pi \int_0^{\tau_\nu} J_\nu(t) E_2(\tau_\nu - t) dt] dv \quad (3.42a)$$

$$q_R^-(n) = 2 \int_0^\infty [B_{2\nu} E_3(\tau_{0\nu} - \tau_\nu) + \Pi \int_{\tau_\nu}^{\tau_{0\nu}} J_\nu(t) E_2(t - \tau_\nu) dt] dv \quad (3.42b)$$

Since NLTE parameter η is the property of the absorbing/emitting species, the NLTE source function appears only in the terms which are attenuated by absorption of radiation by the gaseous species. Use of Eqs. (3.40) and (3.42) are made for evaluating the NLTE radiative flux.

3.2 Spectral Model for Gaseous Absorption

Appropriate spectral models for gaseous absorption are needed for the solution of the radiative flux Eqs. (3.13) and (3.40) derived under equilibrium and nonequilibrium conditions respectively. The absorption model considered in this study is for a nongray gas with molecular band, continuum and atomic line transitions. In general, the spectral absorption coefficient for continuum and line transitions may be expressed as

$$\kappa_{\nu} = \sum \kappa_i^C(\nu) + \sum \kappa_j^L(\nu) \quad (3.43)$$

The summations in the above equation extend over all continuum and line transitions respectively. In the present analysis, only the transitions of the species H_2 , H and H^+ are considered for the no ablation case. For the case with carbon-phenolic ablation injection, the additional chemical species considered for the radiative transport are C_2 , C_3 , C , C^+ , C^- , CO , O , O_2 , e^- , and O^+ .

The absorption coefficients for line transitions depend on the plasma conditions both through the population of the absorption levels and the shape of the spectral lines. For heavy atomic species at high temperatures, the dominant mechanism for the line broadening is the Stark broadening by electron impacts. Following Armstrong et al. [45], the lines can be treated as having the Lorentz shape, for which the shape,

factor is given by

$$b_k(\nu) = (\gamma_k^S/\pi)/[(\nu - \nu_k)^2 + (\gamma_k^S)^2] \quad (3.44)$$

where ν_k is the frequency of the k th line center and γ_k^S is the Stark half-width of the line. In calculation of the absorption coefficients due to atomic line transitions, a line grouping technique is used. In this technique, line transitions near a specified frequency value are grouped together, and the spectral absorption is given as that from the line group. However, each line within the group is treated individually.

The continuum contribution depends mainly on the plasma state through the population of absorbing levels. The spectral absorption coefficient due to continuum transitions is given by

$$\kappa_i^C(\nu) = \sum N_{ij} \sigma_{ij}^C(\nu) \quad (3.45)$$

where N_{ij} is the number density of the absorbing level and σ_{ij}^C is its cross section. The number density of the particular particle is obtained from thermodynamic state calculations.

By employing the detailed information on line and continuum absorption, Nicolet developed a fairly sophisticated radiative transport model for applications to planetary entry environment [17,46,47]. For the calculation of the equilibrium radiative transport properties in the ablation contaminated boundary layers, use of the method given in [46] is made. An approximate model for the frequency dependent absorption coefficient is also developed by Sutton et al.[18]. In this model, the frequency dependence of the absorption coefficient is represented by a step-function with 58 steps of fixed (but not necessarily equal) widths. In this model, the absorption of helium species is neglected. In step-function models, the total absorption coefficient of the j th step is a

summation of the average absorption coefficient for the i th transition in the j th step, given by

$$\kappa_j(\omega) = \sum_i \kappa_{ij}(\omega) \quad (3.46a)$$

$$\kappa_{ij}(\omega) = \frac{1}{\Delta\nu_j} \int_{\nu_j}^{\nu_j + \Delta\nu_j} \kappa_i(\omega) d\nu \quad (3.46b)$$

$$\kappa_i = f(T, N_i, \nu) \quad (3.46c)$$

Once again κ is the equilibrium absorption coefficient, ν the frequency in eV, T is the temperature in degrees Kelvin, and N_i are the number density in cm^{-3} . In this model, the absorption coefficients for the free-free and bound-free transitions of atomic hydrogen are expressed by

$$\kappa_{ff}^H = (2.61 \times 10^{-35} N_e N_{H^+}) / (T^{1/2} \nu^3) \quad (3.47)$$

$$\begin{aligned} \kappa_{bf}^H = & \left[\frac{(1.99 \times 10^{-14} N_H)}{\nu^3} \right] \times \sum_{n_\ell=1}^4 \left(\frac{1}{n_\ell^3} \right) \exp \left[\left(\frac{-157780}{T} \right) \right. \\ & \left. \times \left(1 - \left(\frac{1}{n_\ell^2} \right) \right) \right] \end{aligned} \quad (3.48)$$

$$\text{for } 1 \leq n_\ell \leq 4$$

and

$$\kappa_{bf}^H = [6.31 \times 10^{-20} \left(\frac{T}{\nu^3} \right) N_H] \exp(A) [\exp(B) - 1] \quad (3.49)$$

$$\text{for } 4 < N_\ell \leq N_{\ell\max}$$

where

$$A = \left(\frac{-157880}{T} \right) \left[1 - \left(\frac{\delta}{13.6} \right) \right]$$

$$B = \left(\frac{157780}{T} \right) \left[\frac{1}{25} - \left(\frac{\delta}{13.6} \right) \right]$$

The reduction in the ionization potential δ is calculated by

$$\delta = (1.79 \times 10^{-5} N_e^{2/7}) / T^{1/7} \quad (3.50)$$

For bound-bound transition of hydrogen molecules and atoms

$$\kappa_{bb}^H = S b_k(\nu) \quad (3.51)$$

where the line strength S is given by

$$S = (1.10 \times 10^{-16} f n_\ell^2 N_H) \exp \left[\left(\frac{-157780}{T} \right) \left(1 - \left(\frac{1}{n_\ell^2} \right) \right) \right] \quad (3.52)$$

The line-shape factor $b_k(\nu)$ is given by Eq. (3.44). Using the expressions given above, the absorption due to continuum and line transitions over each step is calculated individually. The total absorption over each individual step is a strong function of temperature, and this model is valid for a wide range of temperatures. Further information on the 58-step model is available in [18]. Use of this model is made in evaluating the equilibrium absorption coefficient for the no ablation injection case.

At high temperatures, the frequency dependence of the absorption coefficient is more orderly because of the relative importance of

continuum transitions over line transitions. Under such conditions, it is possible to represent the spectral absorption of the gas by a relatively fewer number of steps. A spectral model consisting of 30 steps is introduced in this study to represent the absorption by the hydrogen species in the spectral range of 0 to 20 eV. The absorption by the helium species is also neglected in this study. The procedure for developing this model is to calculate the spectral absorption coefficient first by employing Nicolet's detailed model. The 30-step model is illustrated in Fig. 2. Further details on this 30-step model are given in [9]. Few results obtained using the various models are presented under results and discussions for comparative purposes.

The methods outlined thus far to evaluate the equilibrium absorption coefficients are applicable for the hydrogen atoms and molecules. This is quite sufficient if no ablation mass injection is considered in the analysis. However, with ablation products in the shock layer, appropriate relations are needed to evaluate the continuum and line contributions to the absorption coefficient by these species. Information for obtaining the absorption cross section for the electronic band systems belonging to diatomic molecules are available in [48,49]. According to this reference, the equilibrium absorption coefficient for a transition from level 0 to level 1 (higher level) is given by

$$\kappa_{\nu}(0,1) = \sigma_{\nu}(0,1) n_0 \quad (3.53)$$

where n_0 is the number density of the absorbing species in level 0 and $\sigma_{\nu}(0,1)$ is the absorption cross section. This equilibrium absorption coefficient has to be corrected for the NLTE transition. The NLTE absorption coefficient is given by [44]

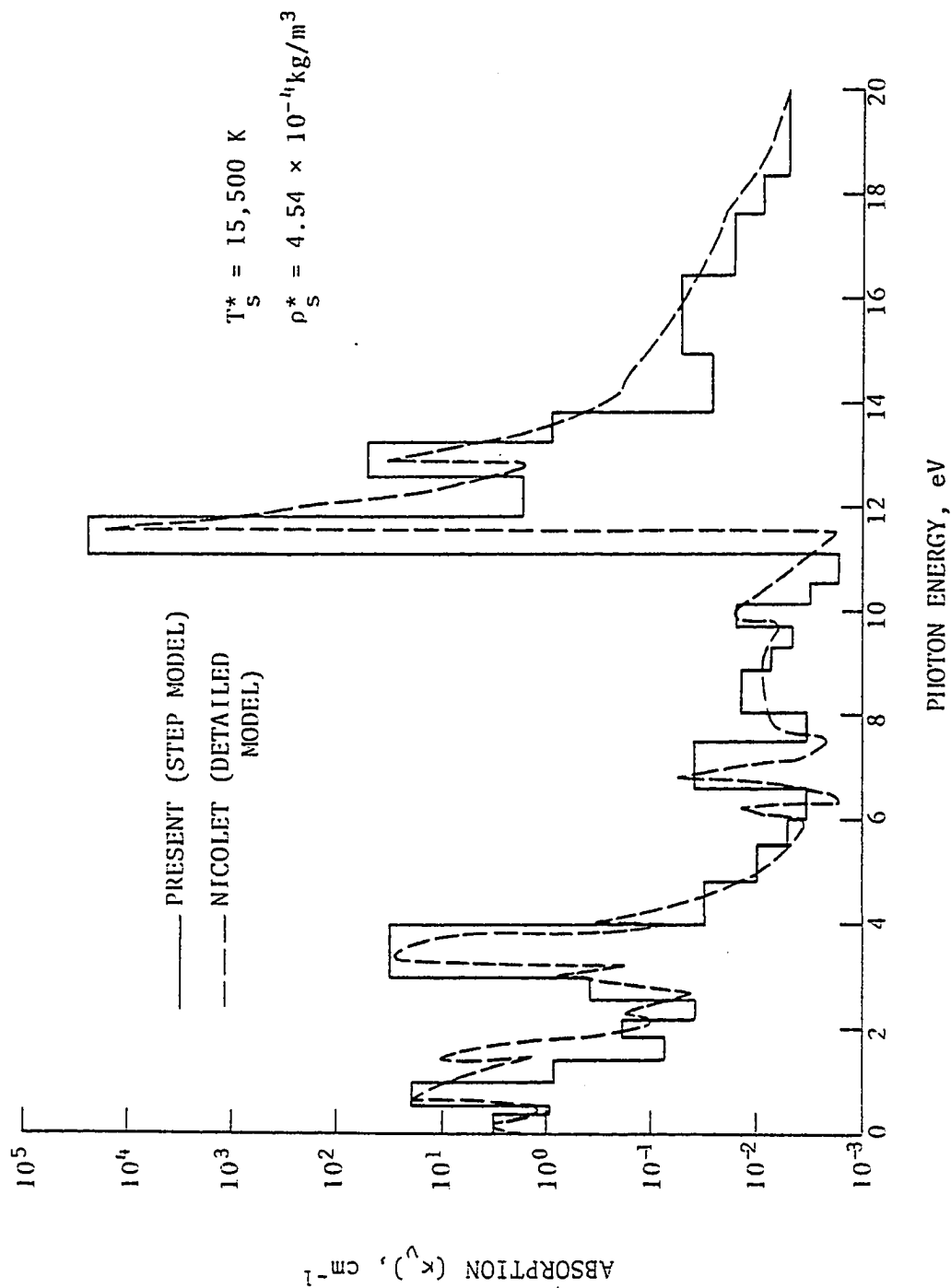


Fig. 2 A 30-Step model to approximate the absorption by Nicolet's detailed model ($T_s = 15,500 \text{ K}$)

$$\kappa_{\nu}^*(\text{NLTE}) = \kappa_{\nu} \left[1 - \left\{ (I_{\Delta\nu} B_{10} + A_{10} + C_{10}) / (C_{01} + B_{01}) \right\} \right] \quad (3.54)$$

where κ_{ν} is the frequency dependent equilibrium absorption coefficient.

By noting that

$$A_{10} = (2h\nu^3 / c^2) B_{10} \quad (3.55a)$$

$$B_{10} = (g_0 / g_1) B_{01} \quad (3.55b)$$

$$C_{10} = (B_{10} / B_{01}) C_{01} \exp(h\nu / kT) \quad (3.55c)$$

$$\eta_c = 1 / C_{10}, \quad \eta_r = 1 / A_{10} \quad (3.55d)$$

Eq. (3.54) becomes

$$\begin{aligned} \kappa_{\nu}^*(\text{NLTE}) = \kappa_{\nu} \left[1 - \left\{ (1 + \eta + \eta / \delta \int_{\Delta\nu} q_{R\nu} d\nu) / (\eta / \delta \right. \right. \\ \left. \left. + \exp(-h\nu / kT)) \right\} \right] \end{aligned} \quad (3.56)$$

Use of this equation is made in evaluation the nonequilibrium absorption coefficients.

It is seen from Eqs. (3.36), (3.39) and (3.56) that for the evaluation of the nonequilibrium absorption coefficients and source function (and hence the nonequilibrium spectral radiative heat flux), one must have information on the collisional relaxation time and the radiative lifetime of the excited states. The procedure for obtaining these is discussed in the next chapter.

4. RADIATIVE LIFETIMES AND COLLISIONAL PROCESSES FOR THE SHOCK-LAYER GASES

For a gaseous medium in local thermodynamic equilibrium, information on the collisions between the various particles and their radiative lifetimes in the excited states are of little importance. To analyze the nonequilibrium phenomena, however, a quantitative study of collisions between various particles is necessary. This study need be extended only to those species whose collisional transition rates (under a given set of physical conditions) are comparable to their radiative transition rates. Nonequilibrium phenomena is important only under these conditions.

For Jovian entry conditions and for the case with no ablation from the probe surface, the NLTE effects are considered only for the hydrogen species in the shock layer. However, for the case of carbon-phenolic ablation injection, the C_2 molecules play a very important role in the radiation blockage. For this case, therefore, contributions of the C_2 molecules are also included in the NLTE analysis. A discussion of the radiative lifetimes and collisional relaxation times of various species considered for the NLTE analysis (in the shock-layer gas) is presented in this chapter.

4.1 Radiative Lifetime of Excited States

The radiative lifetime, η_r , of an excited state is the inverse of the Einstein coefficient for spontaneous emission, A_{10} , and this is given by [50,51] as

$$\eta_r = 1/A_{10} = (c^2/8\pi h\nu^3)/B_{01} \quad (4.1)$$

where B_{01} is the Einstein coefficient for absorption. By using the statistical relation for B_{01} , Eq. (4.1) is written as

$$\eta_r^{-1} = (8\pi\nu^2/c^3) \int_{\Delta\nu} \kappa_\nu d\nu \quad (4.2)$$

For the present study it is more appropriate to use the radiative lifetime in a different form. For a fully allowed electronic transition in the visible or near-ultraviolet region of the spectrum, the radiative lifetime is expressed in terms of the half width of the spectral line, b , as [52]

$$\eta_r = h/(2\pi b) \quad (4.3)$$

Upon inserting the numerical value for the Planck constant h (and converting from ergs to cm^{-1}), the value of η_r is found to be

$$\eta_r = (5.3 \times 10^{-12})/b \quad (4.4)$$

For a Stark-broadened hydrogen line of Lorentz shape, the value of the radiative lifetime is found to be 0.52×10^{-7} sec [7,52]. This value is used in the present study. It should be noted that the radiative lifetime is a function of frequency and, therefore, varies according to the various levels of energy transitions. Considering all radiative transitions probabilities between different energy levels, it is found that the above-mentioned value of η_r corresponds to the shortest time between the ground level (with principal quantum number 1) and the first excited level (with the principal quantum number 2). Since the maximum nonequilibrium effect would correspond to this value of η_r , its use is

justified in the present study.

There are eight known C_2 -band systems in the 0.1 - 7.0 eV (0.2 - 1.2 μm) spectral region. The Swan band system, whose electronic transition is represented by $d^3\pi_g - a^3\pi_u$ (following the notation of Ref. 52), is the strongest radiating system of the C_2 molecules. Freymark band ($E'\Sigma_g^+ - A'\pi_u$) and the Mulliken band ($D'\Sigma_u^+ - x'\Sigma_g^+$) are the next important and radiating systems of the C_2 molecules. Hence, the radiative lifetime of these band systems has to be determined first in order to evaluate their respective NLTE cross sections. For a molecule with an electronic transition, the radiative lifetime is related to the wavelength dependent electronic F-number, the electronic transition moment, and the Einstein coefficient for spontaneous emission $A_{n'n''}$. The measured value for the electronic transition moment is available for the C_2 band systems [53]. The electronic F-number is given in terms of the square of the transition moment $|Re/ea_0|^2$ as

$$F_{el}(\lambda) = (8\pi^2 m_e c / 3 h e^2 \lambda) \sum |Re/ea_0|^2 / A \quad (4.5)$$

where

$$A = (2 - \sigma_{0,\Lambda''}) (2S'' + 1)$$

In the above discussions and relations, the superscript (') denotes the upper state and (") the lower state and S'' represents the spin quantum number of the lower state. The quantity $\sigma_{0,\Lambda} = 1$ for $\Lambda = 0$ and $\sigma_{0,\Lambda} = 0$ for ($\Lambda \neq 0$) and Λ is the resultant angular momentum of electrons. The electronic F-number is related to the band oscillator strength by

$$F_{v',v''} = F_{el} q_{v',v''} \quad (4.6)$$

where $q_{v',v''}$ is the Franck-Condon factor. Now, the radiative lifetime of the v' state can be expressed as

$$(\eta_r)^{-1} = A_{v',v''} = F_{v',v''} \frac{6.67 \times 10^{15}}{\lambda^2} (g''/g') \quad (4.7)$$

Here, g' and g'' are the degeneracies of the upper and lower levels respectively and $g''/g' = 1$. The value of $F_{v',v''}$ measured for the C_2 -Swan (0,0) band is 6.5×10^{-3} [54]. Upon substituting this value of $F_{v',v''}$ and using Eq. (4.7), the radiative lifetime of the C_2 -Swan $3\pi_g$ ($v' = 0$) state is found to be 8.0×10^{-7} seconds. No measured value of the band oscillator strength $F_{v',v''}$ is available for the Freymark and Mulliken band system. However the values of the electronic transition moment are available for these bands and since $F_{v',v''}$ is directly proportional to the electronic transition moment, the radiative lifetime of the $E'\Sigma_g^+$ state of the Freymark (0,1) band is 1.5×10^{-6} seconds and the $D'\Sigma_u^+$ of the Mulliken (0,0) band is 6.95×10^{-6} seconds. These values are used in the present analysis.

4.2 Collisional Relaxation Time

The collisional relaxation time is a strong function of temperature and pressure. At very high temperatures (associated with the ionization mechanism of hydrogen atoms), it is reasonable to assume that most of the NLTE transfer of radiation takes place before the ionization of the hydrogen atom. Hence, for the case with no ablation from the probe surface, it is quite sufficient to consider only the collisional process between H_2 , and H and H^+ . Collisions between two atoms or molecules

may be of the first or second kind. In collisions of the first kind, the kinetic energy (KE) of translation goes into excitation energy according to the process



where A and B are two different (or same) species in the ground state and B^* is the species B in an excited state. Collisions of the second kind are more important for the NLTE analysis at high temperatures. This process is described by



Here, an atom or molecule gives up excitation energy by colliding with another partner. The time taken by a particle to reach the ground state from an excited state is the collisional relaxation time [55].

The collisional relaxation time for collisions between neutral particles (such as atoms and molecules) is given, in general, by the relation

$$\eta_c = 1/f_c = (n\Omega v)^{-1} \quad (4.10)$$

where f_c is the frequency of collisions (sec^{-1}), n is the number density of the colliding particles (cm^{-3}), Ω is the collisional cross section of the colliding particles (cm^2), and v is the most probable velocity of the particles (cm-sec^{-1}). By making use of the gas kinetic relations, the relaxation time (in sec) is expressed in terms of temperature as

$$\eta_c = 4\sqrt{2} \Omega (\pi m/8RT)^{1/2} (1/n) \quad (4.11)$$

where m is the mass of the colliding particles. Information on the collisional cross section for different colliding particles is available in [9,56].

For an extensive study of the NLTE process, a detailed study of the various collisional processes between the particles (present in the radiation field) is necessary. All collisions which are effective in deactivating the excited particles must be considered in the analysis. Relaxation time for the case of collisions between neutral particles of the same kind (i.e., for H_2-H_2 , C_2-C_2 , $H-H$ collisions) can be calculated using Eq. (4.11) with the appropriate values for collisional cross section and mass. On the other hand, the collisions between unlike particles with different masses and cross sections may be equally effective in removing the electronic excitation energy from these particles. In such cases, the effective collisional frequency is calculated by the method explained below. The collisions between H and H_2 is taken as an illustrative example; the procedure is the same for other combinations of molecules and atoms. The number of deactivating collisions made per second between H and H_2 is giving by

$$Z(H - H_2) = 2n_{H_2} \Omega_E [2kT(m_{H_2} + m_H)/\pi m_{H_2} m_H]^{1/2} \quad (4.12)$$

where n_{H_2} is the number density of H_2 , m_{H_2} , and m_H are the masses of a hydrogen molecule and atom respectively. The quantity Ω_E is the effective collisional cross section and is given by the expression

$$\Omega_E = [(\Omega_{H_2} + \Omega_H)/4] + [(\Omega_{H_2} \Omega_H)^{1/2} / 2\pi] \quad (4.13)$$

where Ω_{H_2} and Ω_H are the cross sections of H_2 and H respectively. Hence, the relaxation time (in sec) for H_2 - H collisions is the reciprocal of the collisional frequency $Z(H_2-H)$.

The combined relaxation time for self-collisions and collisions of different kind is given by [57].

$$1/\eta_c(\text{COM}) = X/[\eta_c(H-H)] + (1-X)/[\eta_c(H_2-H)] \quad (4.14)$$

where X represents the mole fraction of hydrogen atoms. In the present study, collisions between $H-H$ and H_2-H are considered in evaluating the combined relaxation time with no ablation injection in the shock-layer. Collisions between H_2-H_2 are neglected because the number density of H_2 is small compared to the number density of atomic hydrogen. Various collisional relaxation times obtained for different collisional processes are shown in Fig. 3 as a function of temperature. With the ablation injection, the important species influencing the collisional deactivation process of the C_2 molecules are H_2 , H , H^+ , C_3 , C , and e^- . The relaxation times obtained by using Eqs. (4.11) - (4.13) for the C_2 - C_2 collisions and the combined collisions are shown in Fig. 4 as a function of temperature. The radiative lifetimes of the Swan (0,0), Freymark (0,1) and Mulliken (0,0) bands are also shown in this figure.

The rate of electronic deexcitation from an upper state to a lower state (by electron impact in a molecule) is given by

$$C_{nm} = \frac{A(T/10,000)^r g_k}{\bar{m}^5 \bar{n}^5 (1/\bar{m}^2 - 1/\bar{n}^2)} \quad (4.15)$$

where \bar{m} and \bar{n} are the principal quantum numbers of the lower and upper states, respectively, and A is the excitation rate constant

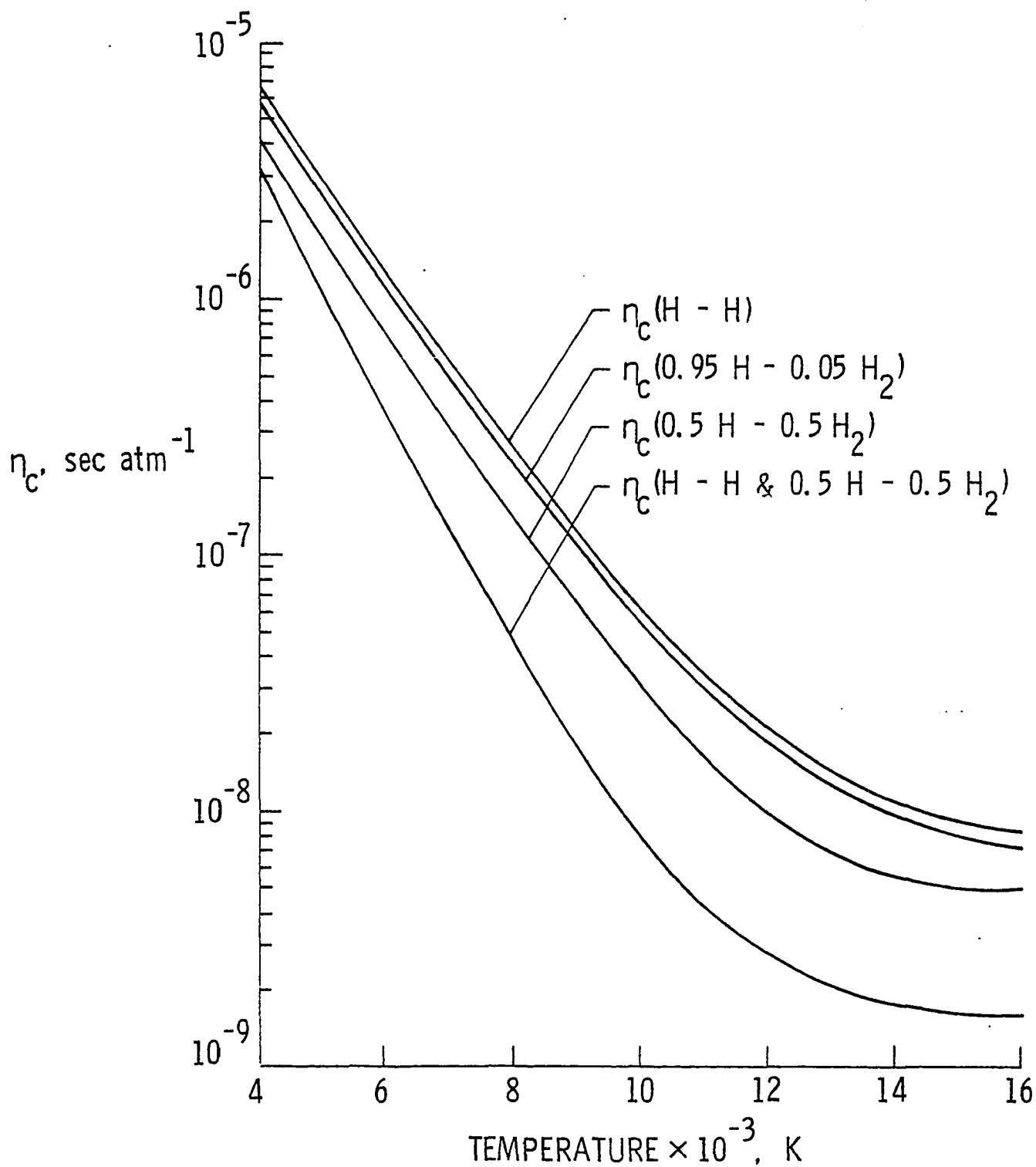


Fig. 3 Collisional relaxation time for atomic and molecular hydrogen species.

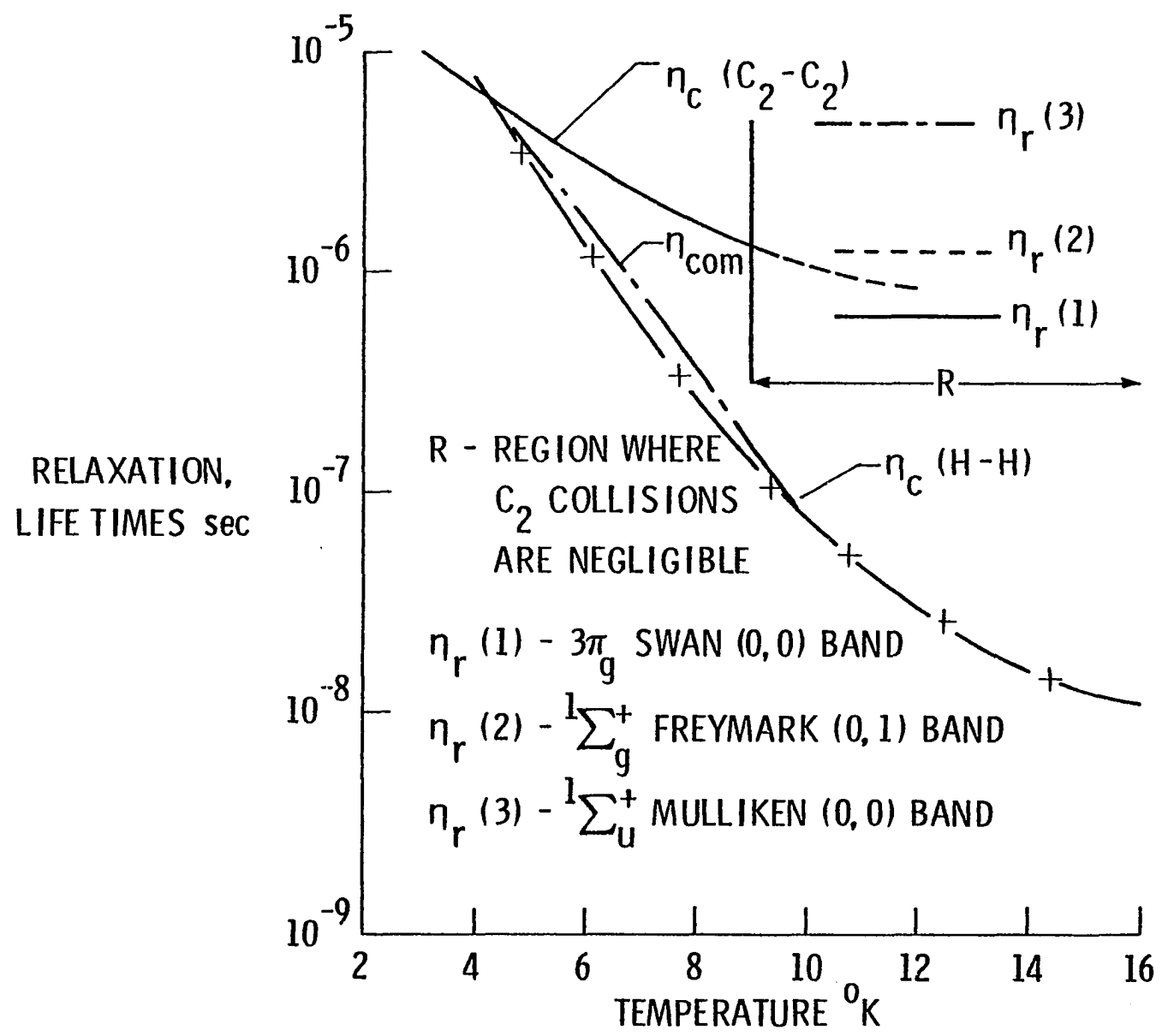


Fig. 4 Variation of collisional relaxation time with temperature.

(different for different molecules). Due to the absence of e^- close to the wall, where the NLTE effect is more pronounced, deexcitation by electronic collisions are not considered. Here, only the collisional deactivation of C_2 by the heavy particles are considered.

The collisional relaxation time for a hydrogen ion is given by the relation [58].

$$\eta_C(H^+) = [m_i^{1/2} (3kT)^{3/2}] / (17.94 n_i e^4 Z^4 \ln \Lambda) \quad (4.16)$$

where m_i represents mass of the ions, n_i is the number density of ions, and Λ is a parameter which is expressed as a function of temperature by

$$\Lambda = (k^3 T^3 / \pi n_i)^{1/2} \quad (4.17)$$

For hydrogen ions, Eq. (4.16) may be simplified further as

$$\eta_C(H^+) = (22.8 T^{3/2}) / n_i \ln \Lambda \quad (4.18)$$

where T is the heavy particle temperature in K. The collisional relaxation times for the hydrogen ions are shown in Fig. 5 for different number densities and temperature values.

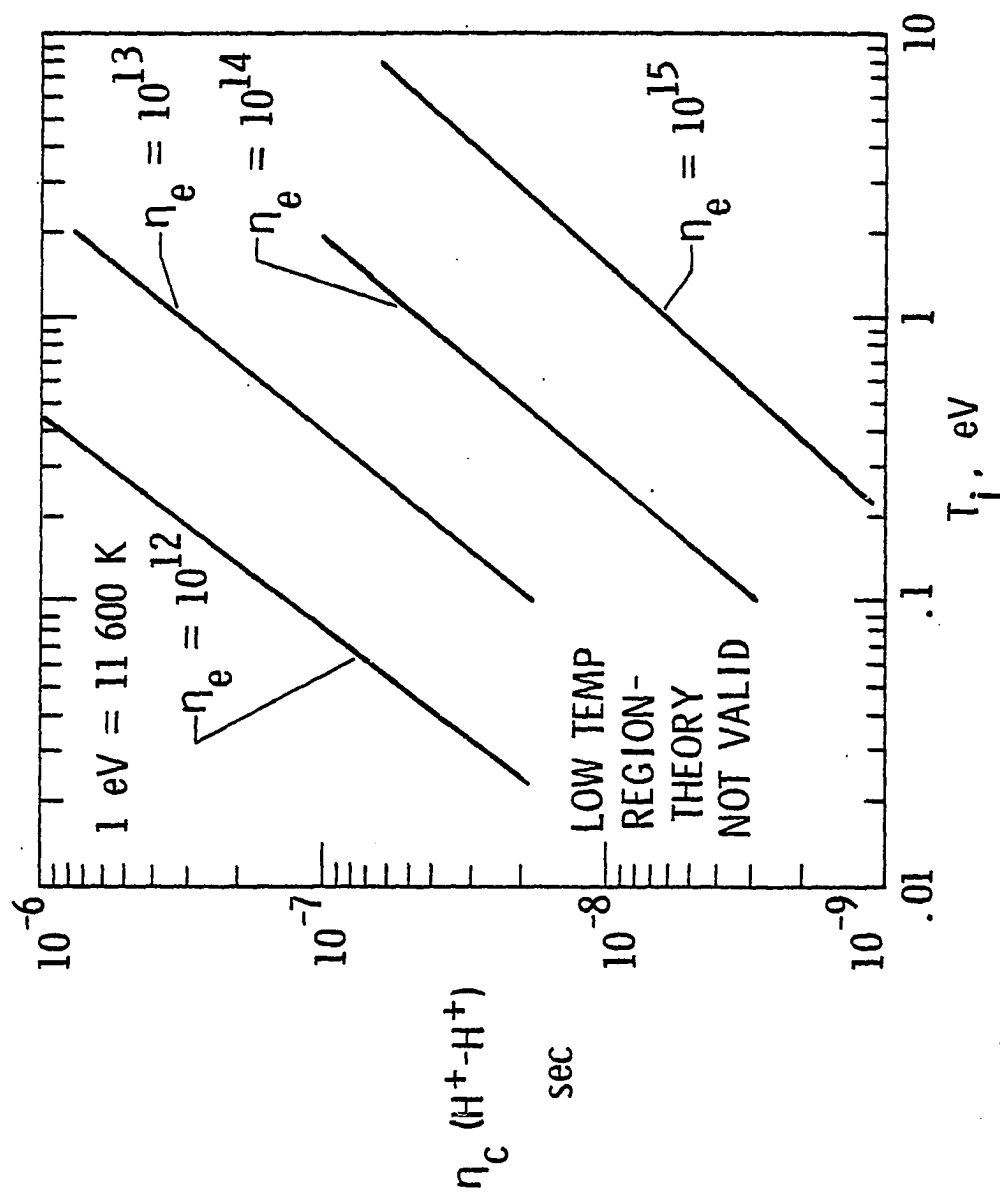


Fig. 5 Collisional relaxation time for hydrogen ions.

5. THERMODYNAMIC AND TRANSPORT PROPERTIES

Thermodynamic properties for specific heat, enthalpy, and free energy, and transport properties for viscosity and thermal conductivity are required for each species considered in the shock-layer. The general expression for total enthalpy, specific enthalpy, and specific heat at constant pressure are given respectively by

$$H_T = h + (u^2 + v^2)/2 \quad (5.1)$$

$$h = \sum C_i h_i \quad (5.2)$$

$$C_p = \sum C_i C_{pi} \quad (5.3)$$

In the present study values for the thermodynamic and transport properties are obtained by using polynomial curve fits. The expressions for h_i and C_{pi} are given by [59,60].

$$h_i = RT [A + (B/2)T + (C/3)T^2 + (D/4)T^3 + (E/5)T^4 + (F/6)T^5 + (G/7)T^6] \quad (5.4)$$

$$C_{pi} = R[A + BT + CT^2 + DT^3 + ET^4 + FT^5 + GT^6] \quad (5.5)$$

where R is the universal gas constant and T is the equilibrium fluid temperature in the shock layer. For different species i , under present investigation, the polynomial coefficients A, B, \dots, G are given in Table 2 and 3. Use of Eqs. (5.1) - (5.3) are made to calculate the enthalpy variation in the shock layer.

For the shock-layer gas, the mixture viscosity and thermal conductivity are obtained by using the semi-empirical formulas of Wilke[61] as;

$$\mu = \sum_{i=1}^N [x_i \mu_i / (\sum_{j=1}^N x_j \phi_{ij})] \quad (5.6)$$

$$K = \sum_{i=1}^N [x_i K_i / (\sum_{j=1}^N x_j \phi_{ij})] \quad (5.7)$$

where

$$\phi_{ij} = [1 + (\mu_i/\mu_j)^{1/2} (M_j/M_i)^{1/4}]^2 / \sqrt{8} [1 + (M_i/M_j)]^{1/2} \quad (5.8)$$

and M_i is the molecular weight of species i . For hydrogen/helium species, specific relations for viscosity and thermal conductivity are given in [62]. The viscosity of H_2 and He, as a function of temperature, can be obtained from Ref. 35 as

$$\mu_{H_2} = (0.66 \times 10^{-6})(T)^{3/2} / (T + 70.5), \text{ N sec m}^{-2} \quad (5.9)$$

$$\mu_{He} = (1.55 \times 10^{-6})(T)^{3/2} / (T + 97.8), \text{ N sec m}^{-2} \quad (5.10)$$

The specific relations for viscosity of other species are given in the reference. The general relation for the thermal conductivity, based on Eq. (5.7), is given as [63].

$$K_i = A + BT$$

The coefficients A and B for different species used in this study are given in Table 4.

The heat transfer to the wall due to conduction and diffusion is referred here as the convective heat flux and is given in terms of the thermal conductivity and viscosity as

$$q_c = -\epsilon^2 [K(\partial T/\partial n) + (\mu Le/Pr) \sum_{i=1}^{N_s} (\partial C_i/\partial n) h_i] \quad (5.12)$$

The values for the Prandtl number Pr and the Lewis number Le are taken as 0.74 and 1.1 respectively. It should be noted that Eq. (5.12) is similar to Eq. (2.23).

Table 2 Coefficients for evaluation of the specific heat at constant pressure for hydrogen/helium species.

Species*	Coefficients						
	A	B	C	D	E	F	G
H	.2500E+01 ¹					.2547E+05	-.4601E+00
	.2500E+01 ²					.2547E+05	-.4601E+00
	.2475E+01 ³	.7366E-04	-.2537E-07	.2386E-11	-.4551E-16	.2523E+05	-.3749E+00
H ₂	.3057E+01 ¹	.2676E-02	-.5809E-05	.5521E-08	-.1812E-11	-.9889E+03	-.2299E+01
	.3100E+01 ²	.5111E-03	.5264E-07	-.3491E-10	.3694E-14	-.8773E+03	-.1962E+01
	.3363E+01 ³	.4656E-03	-.5127E-07	.2802E-11	-.4905E-16	-.1018E+04	-.3716E+01
H ⁺	.2500E+01 ¹					.1840E+06	-.1153E+01
	.2500E+01 ²					.1840E+06	-.1153E+01
	.2500E+01 ³					.1840E+06	-.1153E+01
HE	.2500E+01 ¹					-.7453E+03	.9153E+00
	.2500E+01 ²					-.7453E+03	.9153E+00
	.2500E+01 ³	0.0	0.0	0.0	0.0	-.7453E+03	.9153E+00
HE ⁺	.2500E+01 ¹					.2853E+06	.1608E+01
	.2500E+01 ²					.2853E+06	.1608E+01
	.2500E+01 ³					.2853E+06	.1608E+01
E ⁻	.2500E+01 ¹					-.7453E+03	-.1173E+02
	.2500E+01 ²					-.7453E+03	-.1173E+02
	.2508E+01 ³	-.332E-05	.1364E-08	-.1094E-12	.2934E-17	-.7450E+03	-.1208E+02

* Each species has three sets of values valid over three different temperature range; these are

1 > 300°K 2 > 1000°K 3 > 6000°K

Table 3 Coefficients for evaluating the specific heat at constant pressure for the ablative products.

Species	<u>Coefficients</u>						
	A	B	C	D	E	F	G
C H ₄	.4968E+01	.1727E-01	-.2994E-04	.3246E-07	-.1366E-10	.7545E+05	-.8769E+00
	.6531E+01	.6506E-02	-.2251E-05	.3329E-09	-.1721E-13	.7535E+05	-.7446E+01
	.6531E+01	.6506E-02	-.2251E-05	.3329E-09	-.1721E-13	.7535E+05	-.7446E+01
O	.2946E+01	-.1638E-02	.2421E-05	-.1602E-05	-.1602E-12	.3890E-05	.2963E+01
	.2542E+01	-.2755E-04	-.3102E-08	.4551E-11	-.4368E-15	.2923E+05	.4920E+01
	.2546E+01	-.5952E-04	.2471E-07	-.2798E-11	.9380E-16	.2915E+05	.5049E+01
O ₂	.3526E+01	-.1878E-02	.7055E-05	-.6764E-08	.2155E-11	-.1047E+04	.4305E+01
	.3621E+01	.7361E-03	-.1965E-06	.3620E-10	-.2894E-14	-.1201E+04	.3615E+01
	.3721E+01	.4254E-03	-.2835E-07	.6050E-12	-.5186E-17	-.1044E+04	.3254E+01
O ⁺	.2498E+01	.1141E-04	-.2976E-07	.3224E-10	-.1237E-13	.1879E+06	.4386E+01
	.2506E+01	-.1446E-04	.1244E-07	-.4685E-11	.6554E-15	.1879E+06	.4347E+01
	.2944E+01	-.4108E-03	.9156E-07	-.5848E-11	.1190E-15	.1879E+06	.1750E+01
CO	.3790E+01	-.1619E-02	.3692E-05	-.2031E-08	.2395E-12	-.1435E+05	.2955E+01
	.2984E+01	.1489E-02	-.5789E-06	.1036E-09	-.6935E-14	-.1424E+05	.6347E+01
	.3366E+01	.8027E-03	-.1968E-06	.1940E-10	-.5549E-15	-.1434E+05	.4263E+01
CO ₂	.2400E+01	.8735E-02	-.6607E-05	.2002E-08	.6327E-15	-.4837E+05	.9695E+01
	.4460E+01	.3098E-02	-.1239E-05	.2274E-09	-.1552E-13	-.4986E+05	-.9863E+00
	.4413E+01	.3192E-02	-.1298E-05	.2415E-09	-.1674E-13	-.4894E+05	-.7288E+00

Table 3 Coefficients for evaluation of the specific heat at constant pressure for the ablative products. (Concluded)

Species	<u>Coefficients</u>						
	A	B	C	D	E	F	G
C	.2532E+01	-.1588E-03	.3068E-06	-.2677E-09	.8748E-13	.8524E+05	.4606E+01
	.2581E+01	-.1469E-03	.7438E-07	-.7948E-11	.5890E-16	.8521E+05	.4312E+01
	.2141E+01	.3219E-03	-.5498E-07	.3604E-11	-.5564E-16	.8542E+05	.6874E+01
C ₂	.7451E+01	-.1014E-01	.8587E-05	.8732E-09	-.2442E-11	.9891E+05	-.1584E+02
	.4043E+01	.2057E-03	.1090E-06	-.3642E-10	.3412E-14	.9970E+05	.1277E+01
	.4026E+01	.4857E-03	-.7026E-07	.4666E-11	-.1142E-15	.9787E+05	.1090E+01
C ₃	.5564E+01	-.4687E-02	.1533E-04	-.1509E-07	.5100E-11	.9926E+05	-.2000E+01
	.4394E+01	.2964E-02	-.1541E-05	.3796E-09	-.3010E-13	.9926E+05	.2970E+01
	.2213E+02	-.1759E-01	.5565E-05	-.6758E-09	.2925E-13	.9423E+05	-.1021E+03
C ⁺	.2593E+01	-.4068E-03	.6892E-06	-.5266E-09	.1508E-12	.2166E+06	.3895E+01
	.2511E+01	-.1735E-04	.9504E-08	-.2218E-11	.1862E-15	.2166E+06	.4286E+01
	.2528E+01	.4869E-05	-.7026E-08	.1134E-11	-.3476E-16	.2168E+06	.4139E+01
C ₂ H	.2649E+01	.8491E-02	-.9816E-05	.6537E-08	-.1735E-11	.5627E+05	.7689E+01
	.4420E+01	.2211E-02	-.5929E-06	.9419E-10	-.6852E-14	.5583E+05	-.1158E+01
	.5307E+01	.8966E-03	-.1378E-06	.9251E-11	-.2278E-15	.5809E+05	-.5288E+01
C ₂ H ₂	.1410E+01	.1905E-01	-.2450E-04	.1539E-07	-.4134E-11	.2618E+05	.1139E+02
	.4575E+01	.5123E-02	-.1745E-05	.2867E-09	-.1795E-13	.2560E+05	-.3573E+01
	.6789E+01	.1503E-02	-.2295E-06	.1534E-10	-.3763E-15	.2590E+05	-.1539E+02
C ₃ H	.3344E+01	.1068E-01	-.1331E-04	.1338E-07	-.5698E-11	.6258E+05	.6000E+01
	.3877E+01	.6724E-02	-.2605E-05	.4416E-09	-.2708E-13	.6256E+05	.3826E+01
	.3877E+01	.6724E-02	-.2605E-05	.4416E-09	-.2708E-13	.6256E+05	.3826E+01

1 > 300°K

2 > 1000°K

3 > 6000°K

Table 4 Coefficients for thermal conductivity in Eq. (5.11)

Species	COEFFICIENTS	
	A	B
H	.2496E-04	.5129E-07
H	.3211E-04	.5344E-07
H ⁺	.2600E-03	
HE	.2038E-04	.3249E-07
HE ⁺	.2600E-03	
E ⁻	.2600E-03	
C	.2506E-04	.7479E-08
C	.8590E-05	.6233E-08
C	.6300E-05	.5804E-08
C ⁺	.2600E-03	
C H	.1126E-04	.7439E-08
C H	.1126E-04	.7439E-08
C H	.6300E-05	.5804E-08
C H	.6300E-05	.5804E-08
O	.1250E-04	.7092E-08
O	.1019E-04	.4901E-08
O ⁺	.2600E-03	
CO	.8590E-05	.6233E-08
CO	.8590E-05	.6233E-08

6. METHOD OF SOLUTION

The numerical procedure for solving the inviscid and viscous flow equations are discussed in detail in [5,29]. Tiwari and Szema applied the method outlined in Ref. 29 in their study of the effects of precursor heating on chemical and radiative nonequilibrium viscous flow around a Jovian entry body. A modified form of this procedure is used in this study to obtain solutions of the shock-layer equations under both the equilibrium and nonequilibrium radiative heat transfer conditions. In this method, a transformation is applied to the viscous shock-layer equations in order to simplify the numerical computations. In this transformation most of the variables are normalized with their local shock values. The transformed variables are

$$\begin{aligned}
 \eta &= n/n_s & \bar{p} &= P/P_s & \bar{\mu} &= \mu/\mu_s \\
 \xi &= S & \bar{\rho} &= \rho/\rho_s & \bar{k} &= k/k_s \\
 \bar{u} &= u/u_s & \bar{T} &= T/T_s & C_p &= C_p/C_{ps} \\
 \bar{v} &= v/v_s & \bar{H} &= H/H_s & &
 \end{aligned} \tag{6.1}$$

The transformation relating the differentials are

$$\partial/\partial s () = \partial/\partial \xi (1/n_s)(dn_s/d\xi)\eta \quad \partial/\partial \eta () \tag{6.2a}$$

and

$$\partial/\partial n () = 1/n_s \quad \partial/\partial \eta (), \quad \partial^2/\partial n^2 = 1/n_s^2 \quad \partial^2/\partial \eta^2 () \tag{6.2b}$$

The transformed equation can be expressed in a general form as

$$\partial^2 W / \partial \eta^2 + a_1 \partial W / \partial \eta + a_2 W + a_3 + a_4 \partial W / \partial \xi = 0 \quad (6.3)$$

The quantity \bar{W} represents \bar{u} in the x -momentum equation, \bar{T} in the temperature energy equation, \bar{H} in the enthalpy energy equation, and C_i in the species continuity equations. The coefficients a_1 to a_4 are given in [5]. With radiation included in the study, the coefficient a_3 is different from the expression given in Ref. 5. The modified value for the a_3 in the enthalpy energy equation is

$$\begin{aligned} a_3 = & \frac{p_{r,s} \bar{p}_r n_s^2}{\mu_s \bar{\mu} H_s} \left[\frac{1}{n_s} \frac{\partial \psi}{\partial \eta} + \left(\frac{\kappa}{1 + n_s \eta \kappa} + \frac{\cos \theta}{r + n_s \cos \theta} \right) \psi \right] \\ & + \frac{n_s p_r p_s v_s \bar{v}}{\epsilon^2 \mu_s \bar{\mu} H_s} \frac{\partial p}{\partial \eta} - \frac{n_s \bar{p}_r p_{r,s}}{\epsilon^2 \mu_s H_s \bar{\mu}} \left[\frac{1}{n_s} \frac{\partial q_R}{\partial \eta} \right. \\ & \left. + q_R \left(\frac{\kappa}{1 + n_s \eta \kappa} + \frac{\cos \theta}{r + n_s \cos \theta} \right) \right] \end{aligned} \quad (6.4)$$

where

$$\begin{aligned} \psi = & \frac{\mu_s}{n_s p_{r,s}} \left[\frac{0.1 \bar{\mu}}{p_r} \sum_{i=1}^N h_i \frac{\partial C_i}{\partial \eta} + \frac{u_s^2 \bar{\mu} \bar{u}}{p_r} (p_{r,s} \bar{p}_r - 1) \frac{\partial \bar{\mu}}{\partial \eta} \right] \\ & - \frac{\mu_s \mu_s^2 \kappa \bar{\mu} u^2}{1 + n_s \eta \kappa} \end{aligned} \quad (6.5)$$

other transformed equations are the same as given in [5].

The surface boundary conditions in terms of transferred variables are

$$\bar{\mu} = 0, \bar{v} = 0, \bar{T} = \bar{T}_w \quad (6.5)$$

The transformed shock conditions are found to be

$$\bar{u} = \bar{v} = \bar{T} = \bar{H} = \bar{\rho} = \bar{p} = 1 \quad (6.6)$$

at $n = 1$.

The second order partial differential equations as expressed by Eq. (6.3), along with the surface boundary and shock conditions, are solved by employing an implicit finite difference scheme. The procedure is discussed briefly in Appendix A where flow diagrams for specific computations are also provided.

7. RESULTS AND DISCUSSIONS

The results obtained in the present study extend over a wide range of free stream and flow conditions and probe shapes. The basic shapes considered for the entry probes are sphere cones, hyperboloids and ellipsoids. Most results have been obtained for the entry conditions (i.e., the free-stream conditions at different entry altitudes) given in Table 1. However, some specific results have been obtained also for other entry conditions. The shock-layer gas has been assumed to be in chemical equilibrium for the entire study. Different spectral models for radiative transfer in the gas have been considered and various results obtained by these models are compared. The NLTE analysis has been carried out first by considering only the hydrogen/helium species in the shock-layer gas. Later, the contributions of ablative products are included also in the NLTE analysis. Thus, in accordance with the four areas of this study, the results are presented in the following four sections: (1) Significance of radiation models on the flow-field solutions, (2) Influence of NLTE radiation without ablation injection, (3) Importance of NLTE radiation with ablation injection, and (4) Effect of probe shape change on the flow phenomena. The physical model and flow conditions for which the results were obtained are given in each section.

7.1 Significance of Radiation Models on the Flowfield Solutions

By employing the three different absorption models discussed in sec. 3.2, results were obtained for the flowfield variables and the wall

radiative heat flux distribution for different entry conditons and body configurations. Inviscid as well as viscous results were obtained for a 55-degree half angle sphere cone, while only viscous results were obtained for a 50-degree hyperboloid. Comparison of inviscid and viscous results is presented for a 55-degree sphere cone entering the Jovian atmosphere at an altitude of $Z = 116$ km. Next, a series of viscous results are presented for the 55-degree sphere cone at different entry conditions. Finally, viscous results for a 50-degree hyperboloid are presented.

7.1.1 Comparison of Inviscid and Viscous Results

Inviscid and viscous results obtained by employing the detailed and 30-step radiation models are compared in this section. The temperature distribution along the stagnation streamline is illustrated in Fig. 6a. The agreement between inviscid and viscous results is seen to be fairly good except near the body, where viscous boundary-layer effects are predominant (see Fig. 6b). The difference between the detailed and 30-step model results is lower for the inviscid case than the viscous case. This is due to relatively higher temperature across the shock layer for the inviscid analysis. As pointed out earlier, the step model is more accurate at higher temperatures.

The shock standoff distance as function of body location is illustrated in Fig. 7. The first three curves illustrate the inviscid results for the three different radiation models. The fourth curve, obtained by employing the Nicolet's detailed radiation model, is for the viscous case, and is drawn here for comparison. The shock standoff distance is slightly larger for the present 30-step model as compared

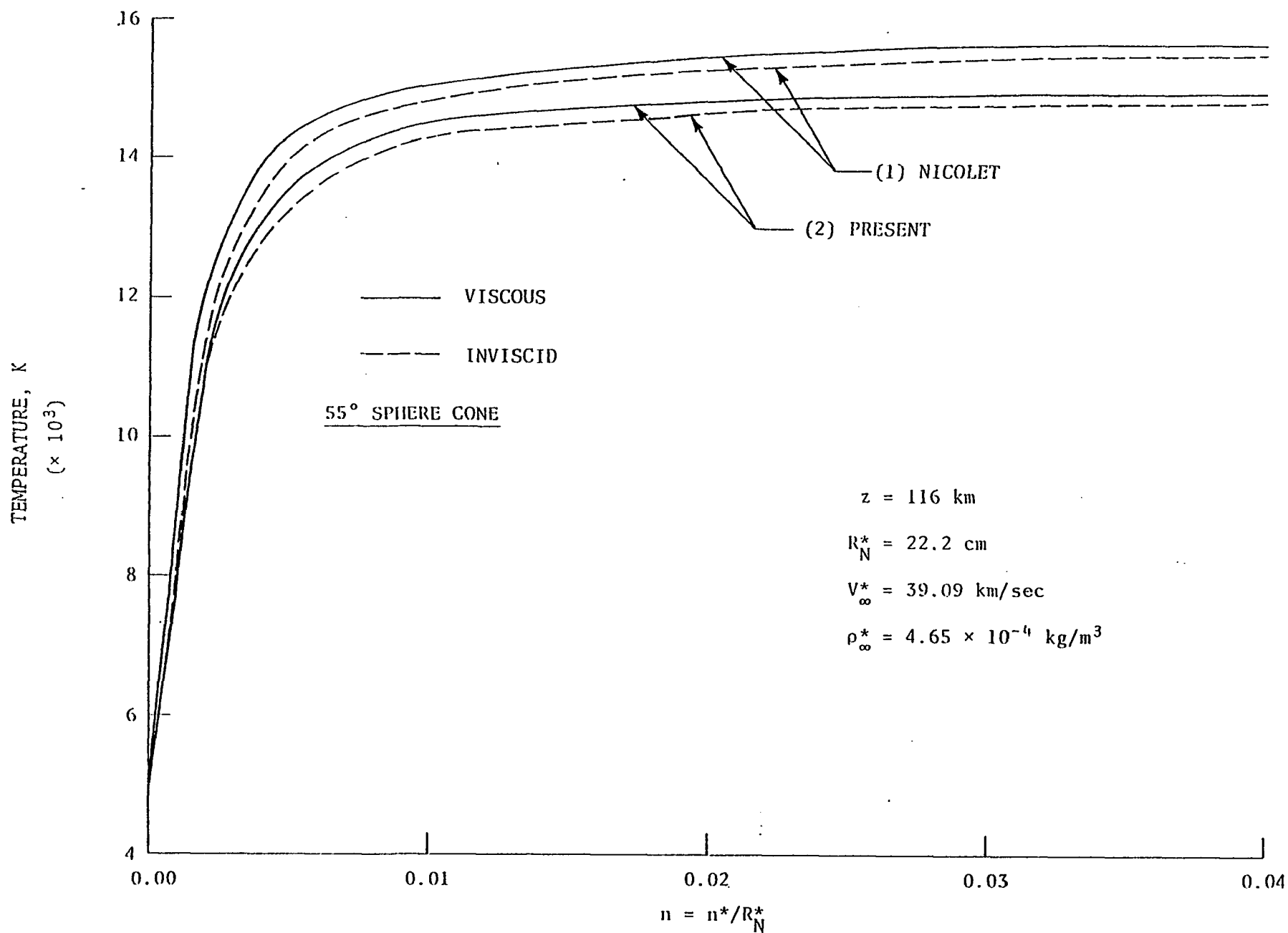


Fig. 6a Temperature distribution along the stagnation streamline for inviscid and viscous analysis (55-degree sphere cone, $Z = 116 \text{ km}$).

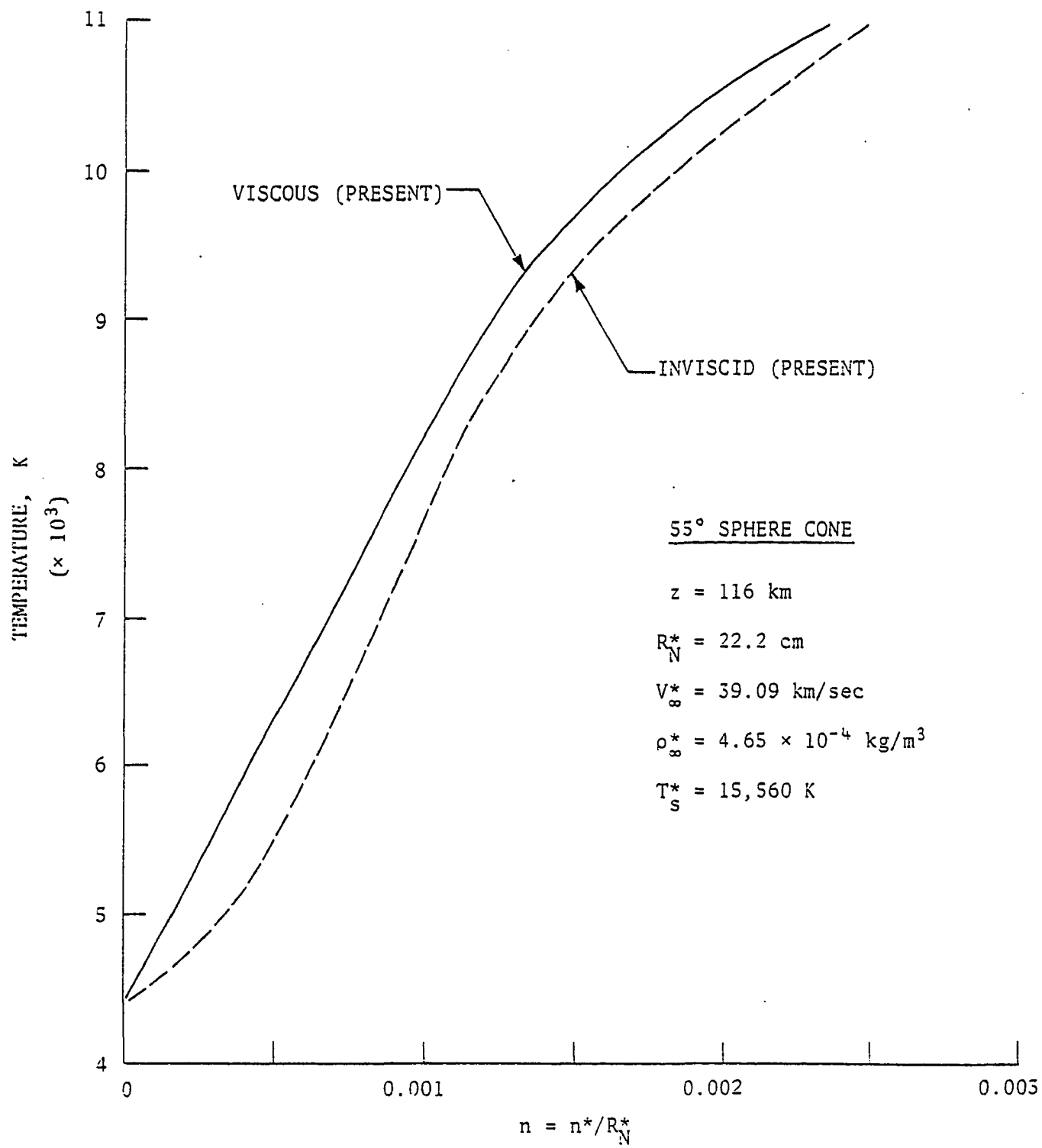


Fig. 6b (Concluded)

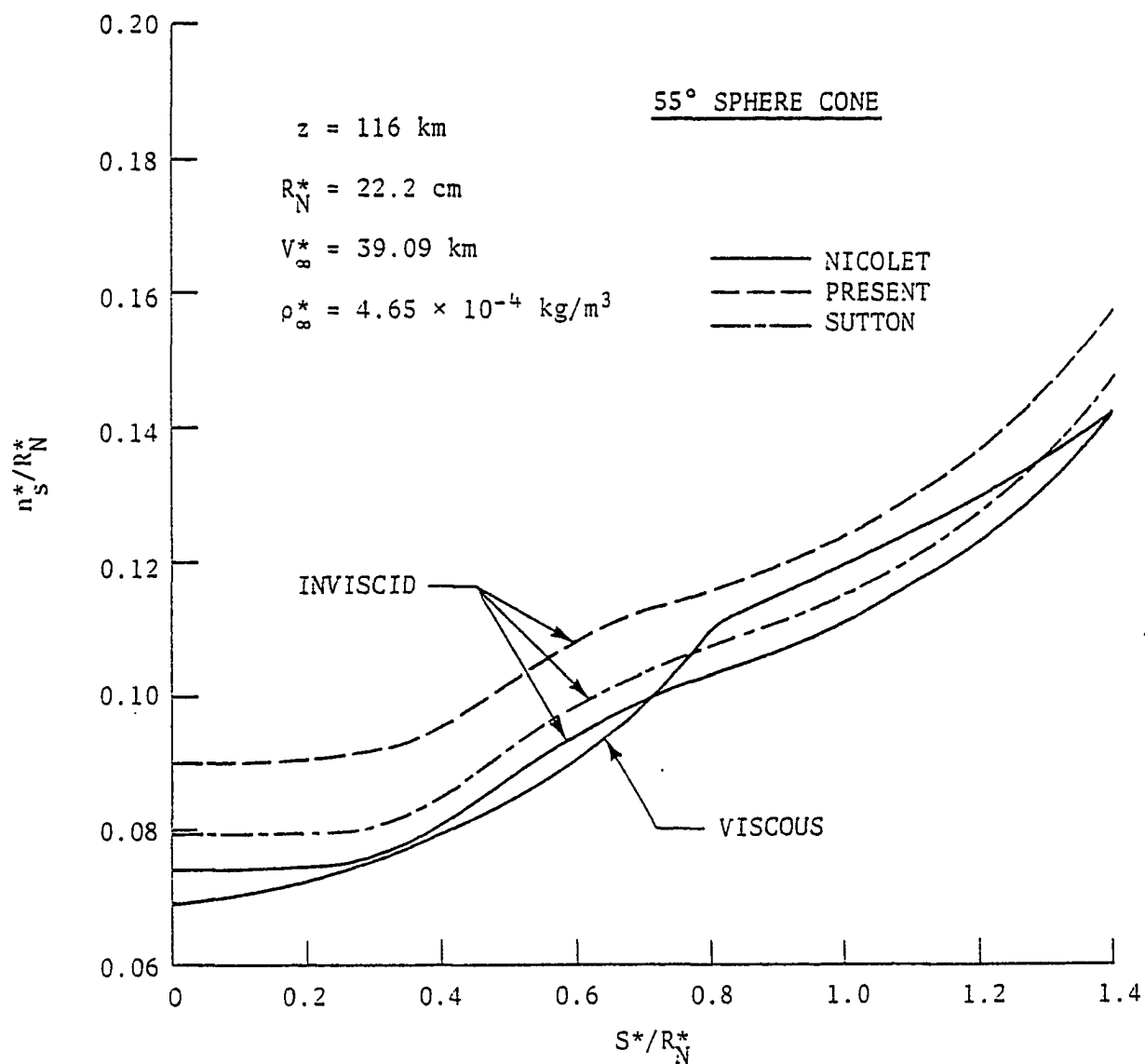


Fig. 7 Shock standoff variation with distance along the body surface for inviscid and viscous analysis (55-degree sphere cone, $Z = 116 \text{ km}$).

with the results of the detailed and Sutton's 58-step models. Although the difference between inviscid and viscous results is seen to be quite small, use of the viscous analysis is recommended for more realistic and accurate calculations.

Results of radiative heating along the body are illustrated in Fig. 8. While inviscid results are seen to be slightly higher at the stagnation point, viscous results are relatively higher at other body locations (up to $s^*/R_N^* = 0.6$). This is a direct consequence of viscous boundary-layer effects. Discussion on viscous results of different radiation models is given in the next subsection.

7.1.2 Viscous Results for a 55-Degree Sphere Cone

Viscous results for a 55-degree cone (with a nose radius of 22.2 cm) is presented in this subsection for different entry conditions. Results of various radiation models are compared in order to establish the validity of the present 30-step radiation model.

In the shock layer, the temperature distribution along the stagnation streamline is illustrated in Fig. 9 for two different free-stream (density) conditions. It is found that the present 30-step model underpredicts the shock-layer temperature by a maximum of 11 percent in comparison to Nicolet's detailed model and by about 4.5 percent when compared with Sutton's 58-step model. For free-stream conditions resulting in higher shock temperature, the agreement between the results is even better. This is because the higher temperature absorption spectrum can be approximated more accurately by the present step-model.

From the results presented in Figs. 6 and 9, it is noted that there exists a steep temperature gradient in the regions close to the body.

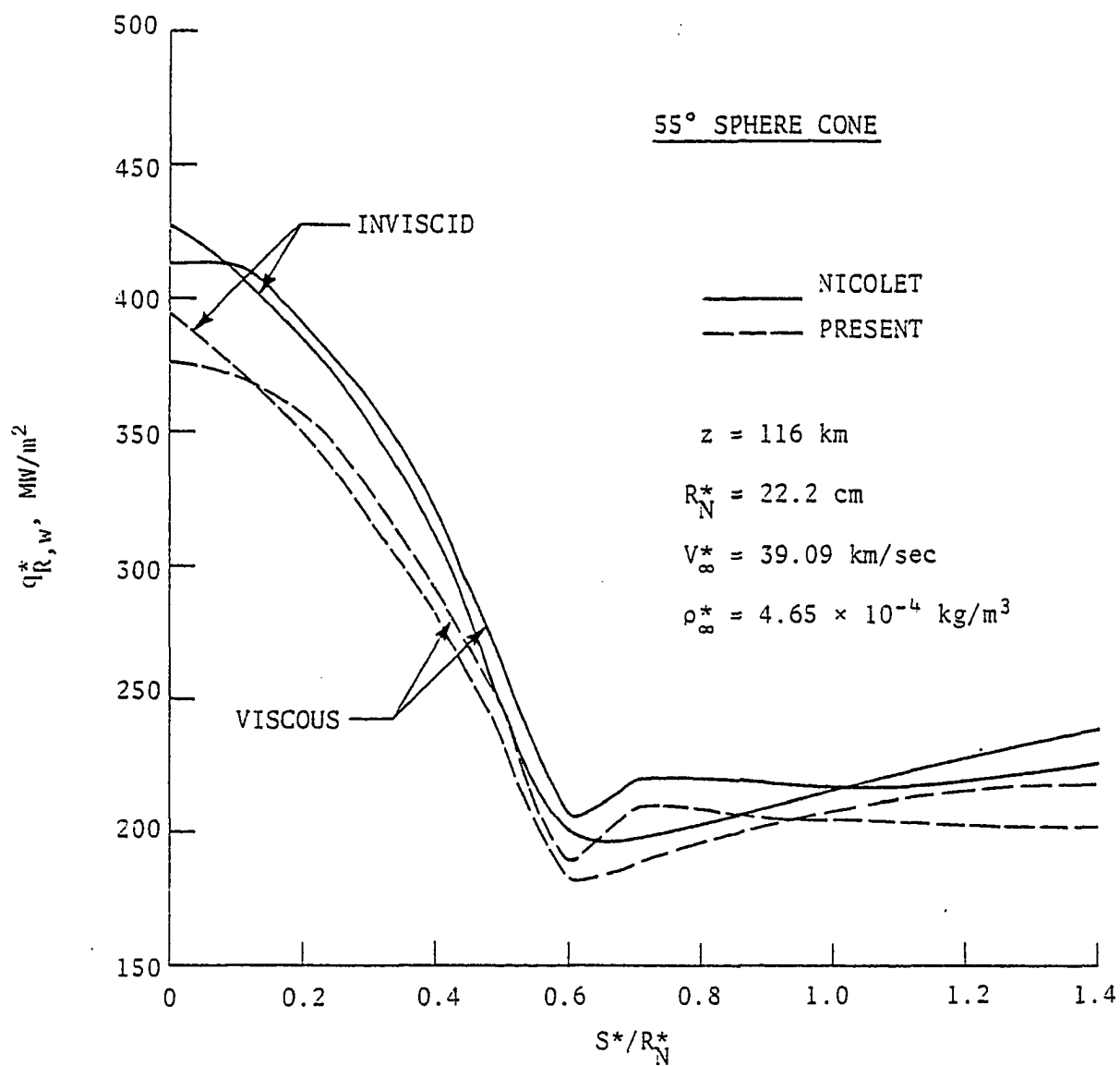


Fig. 8 Radiative heating along the body for inviscid and viscous analysis (55-degree sphere cone, $Z = 116 \text{ km}$).

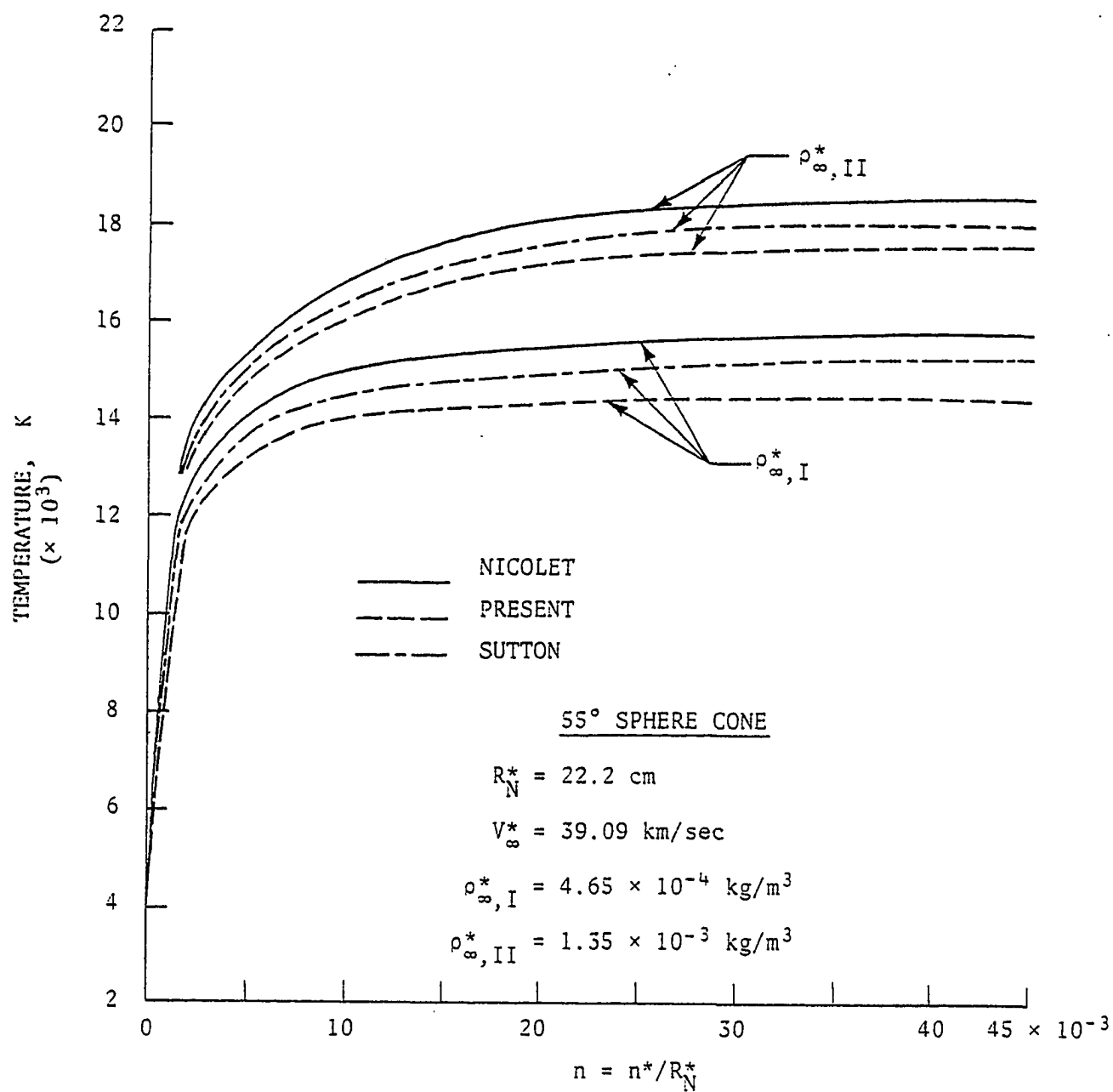


Fig. 9 Temperature distribution along the stagnation streamline for two different free-stream densities (55-degree sphere cone).

At locations about five times the nose radius (normal to the body), only a slight variation in the shock-layer temperature is noticed. This fact was utilized in dividing the shock layer into different temperature zones for evaluating the absorption coefficient. In a preliminary study, two methods were used to account for the temperature dependence of the absorption coefficient. In the first method, the absorption coefficient was calculated at the shock temperature, T_s^* . This value was used in analyzing the flow field in the entire shock layer. Results obtained by this method are designated here as "present-approximate" results. In the second method, the shock layer is divided into three different temperature zones, two of which are closer to the body (because of the steep gradient near the body). For each temperature zone, a different 30-step model for absorption is obtained. These are read as input in the computer program while evaluating the flow variables in the particular temperature zone. Results obtained by this method are denoted here as "present" results.

The variation in temperature just behind the shock (at location $n = 0.05$) with distance along the body surface is illustrated in Fig. 10 for entry conditions at $Z = 116$ km. The results of the present model are found to be about six percent lower than the results of Nicolet's model. This difference is seen to be fairly uniform along the body.

Figure 11 shows the shock standoff variation with distance along the body surface for entry conditions at $Z = 116$ km. Results of Sutton's model are found to be in general agreement with the results of Nicolet's model. The present model is seen to overestimate the results by a maximum of 8.6 percent when compared with the results of Nicolet's model. This is mainly because the present model underpredicts the shock-layer density.

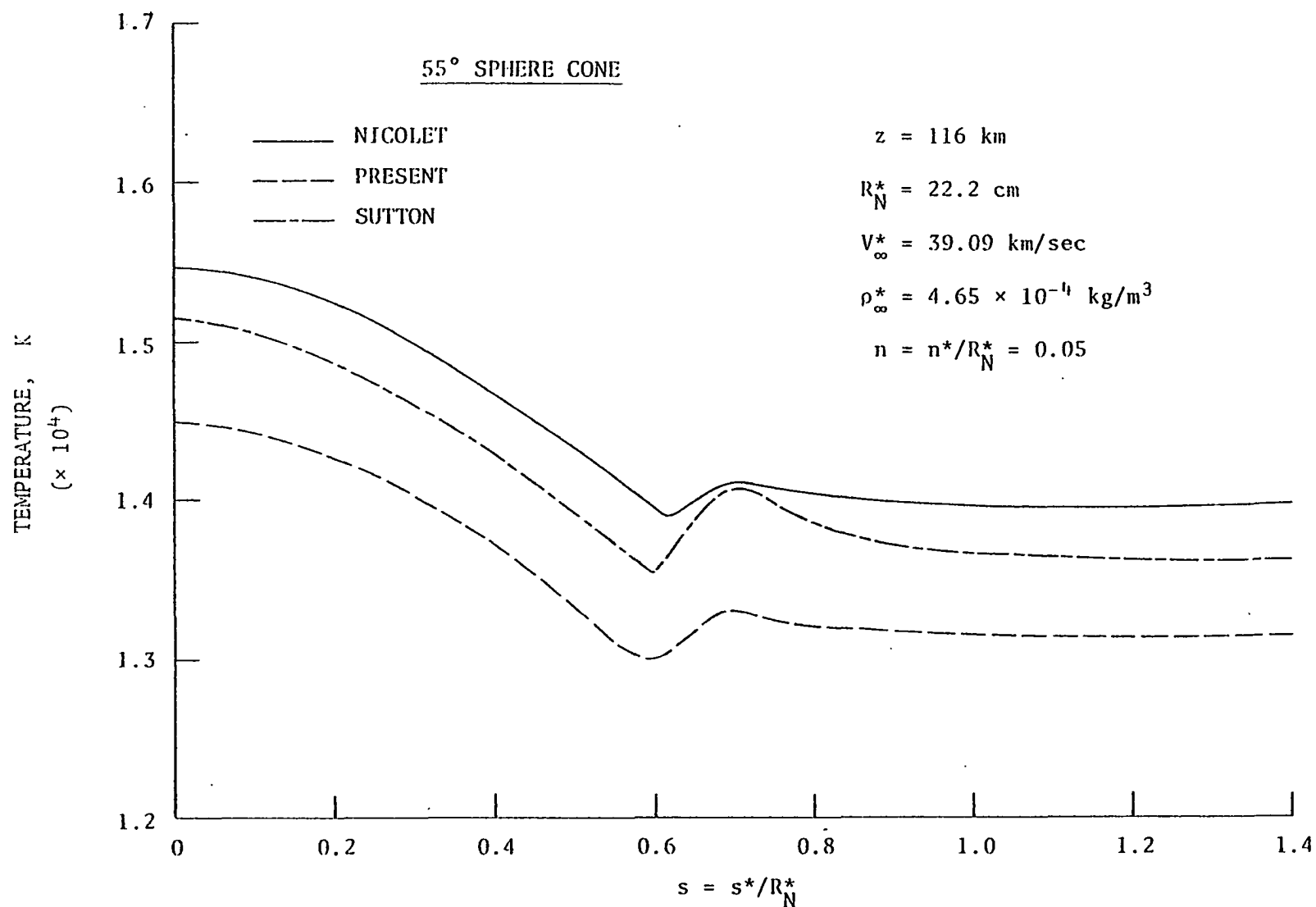


Fig. 10 Temperature variation just behind the shock ($n = 0.05$) with distance along the body surface (55-degree sphere cone, $Z = 116 \text{ km}$).

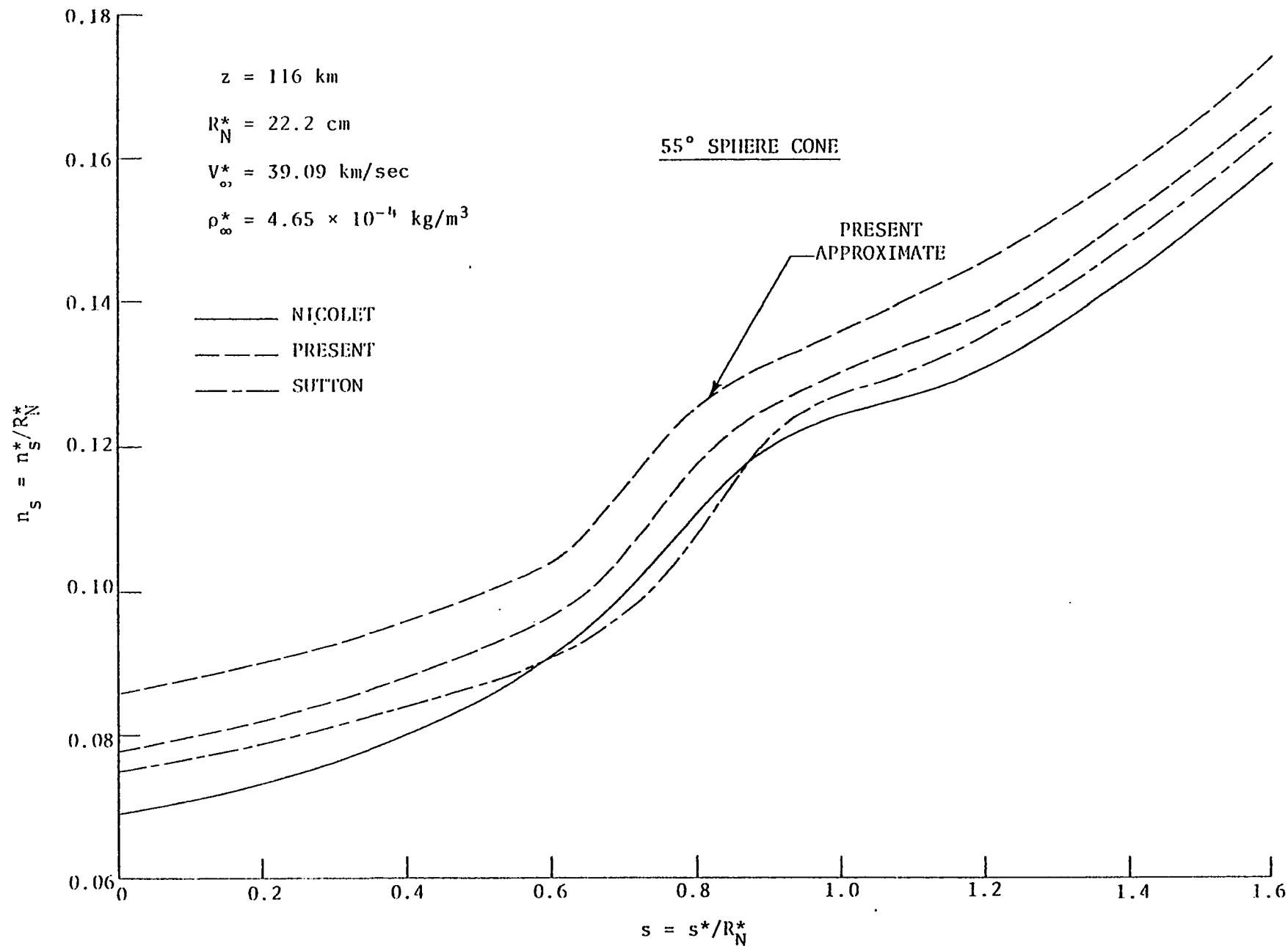


Fig. 11 Shock standoff variation with distance along the body surface (55-degree sphere cone, $Z = 116 \text{ km}$).

The radiative heating rate along the body surface is illustrated in Figs. 12 and 13 for different entry conditions. As would be expected, in all cases, the maximum heating occurs at the stagnation point. For $Z = 116$ km, results presented in Fig. 12 show that the present model underpredicts the heating rate by a maximum of 13.6 percent when compared with Nicolet's model. For the case of higher free-stream density (and hence a higher shock temperature), differences in the results of the present and other models are seen to be smaller. Figure 13 shows the results of radiative heating for 131-km entry conditions. For this higher altitude, the heat transferred to the body is lower because of lower free-stream density and pressure. For this case, differences in the results of the present and Nicolet's model are seen to be slightly higher.

7.1.3 Viscous Results for a 50-Degree Hyperboloid

Viscous results for a 50-degree hyperboloid (with a nose radius of 22.2 cm) are presented in this subsection for different entry conditions. The temperature distribution in the shock layer (along the stagnation streamline) is illustrated in Fig. 14 for entry conditions at $Z = 116$ km. The results of the three radiation models are seen to follow the same general trend as for the 55-degree sphere cone. A maximum difference of about 4.5 percent is seen between the present model and Nicolet's model. This difference is near the body (at $n = 0.0095$). Agreements between the results are better towards the shock.

The variation in temperature just behind the shock (at location $n = 0.07$) with distance along the body surface is illustrated in Fig. 15 for entry conditions at $Z = 116$ km. The results indicate very good

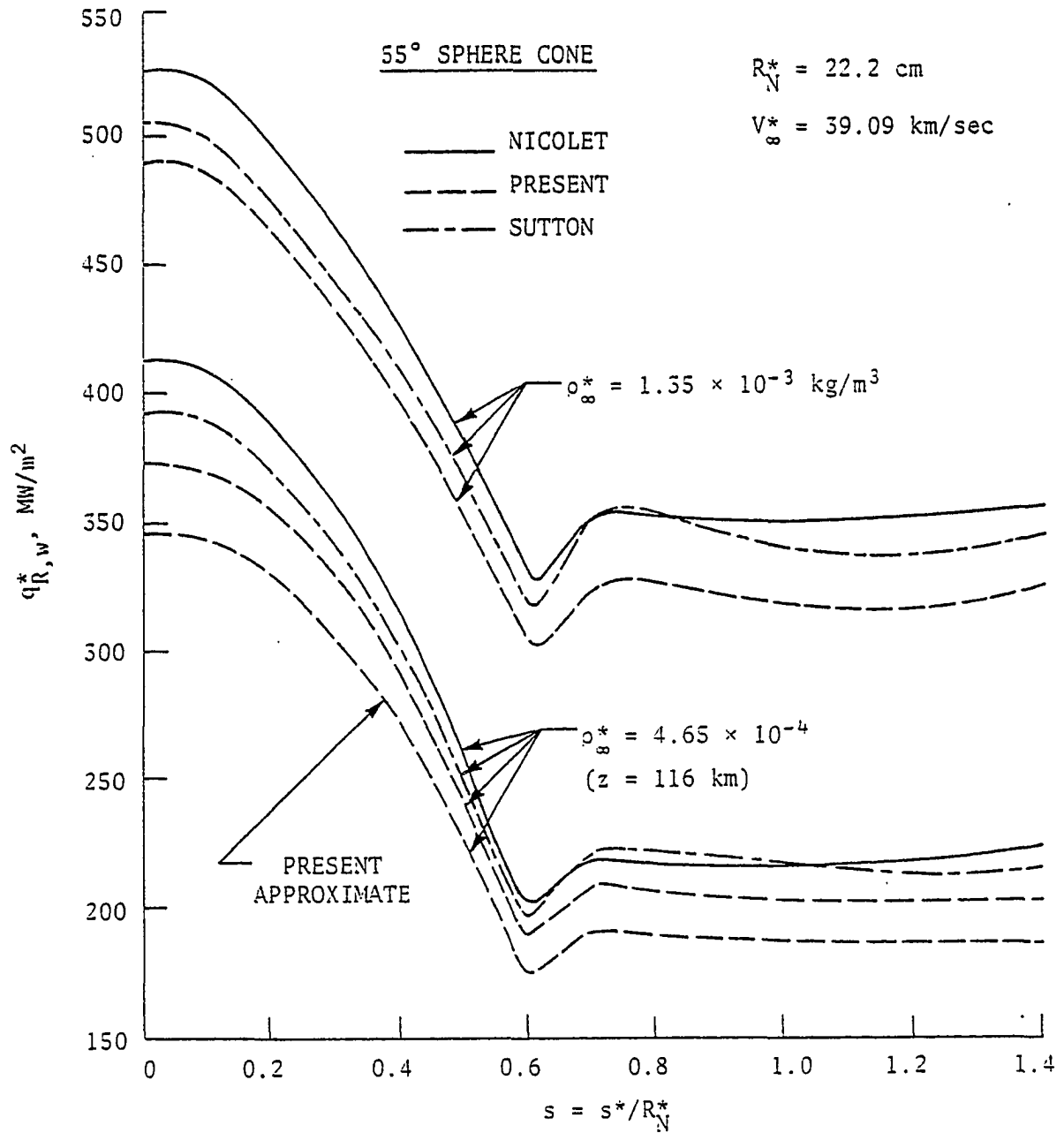


Fig. 12 Radiative heating along the body for two different free-stream densities (55-degree sphere cone).

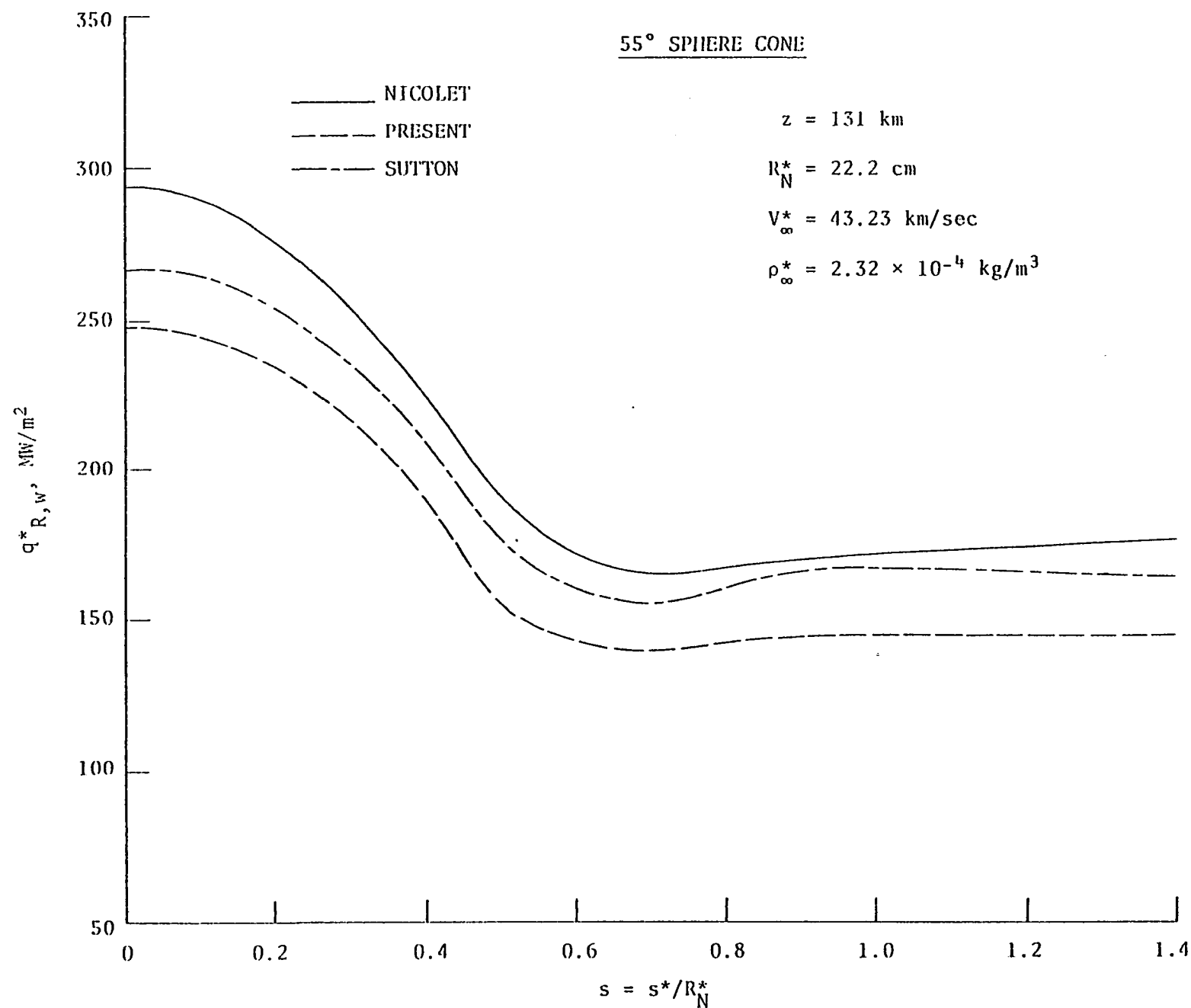


Fig. 13 Radiative heating along the body for entry conditions at $Z = 131 \text{ km}$ (55-degree sphere cone).

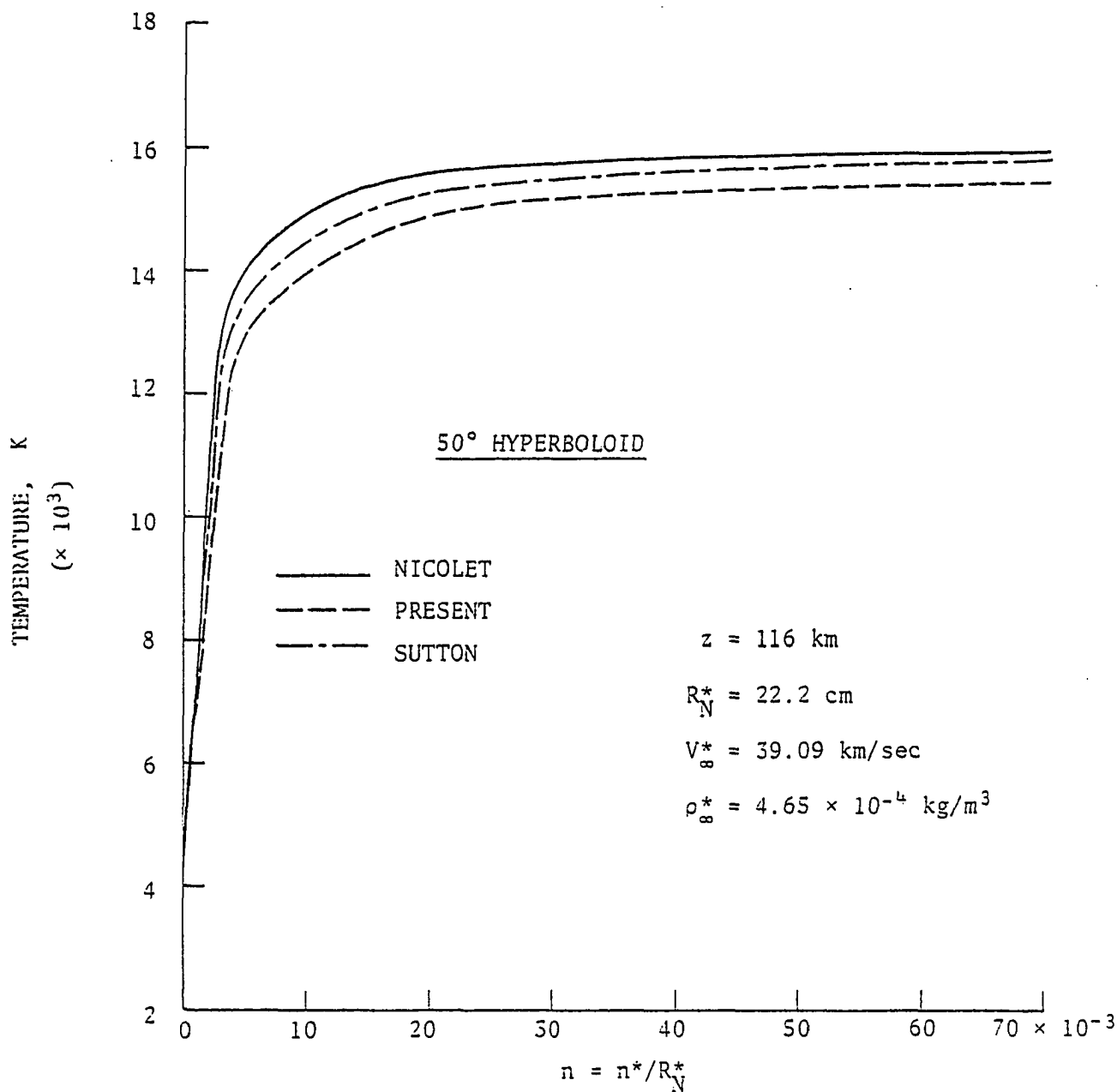


Fig. 14 Temperature distribution along the stagnation streamline (50-degree hyperboloid, $Z = 116 \text{ km}$).

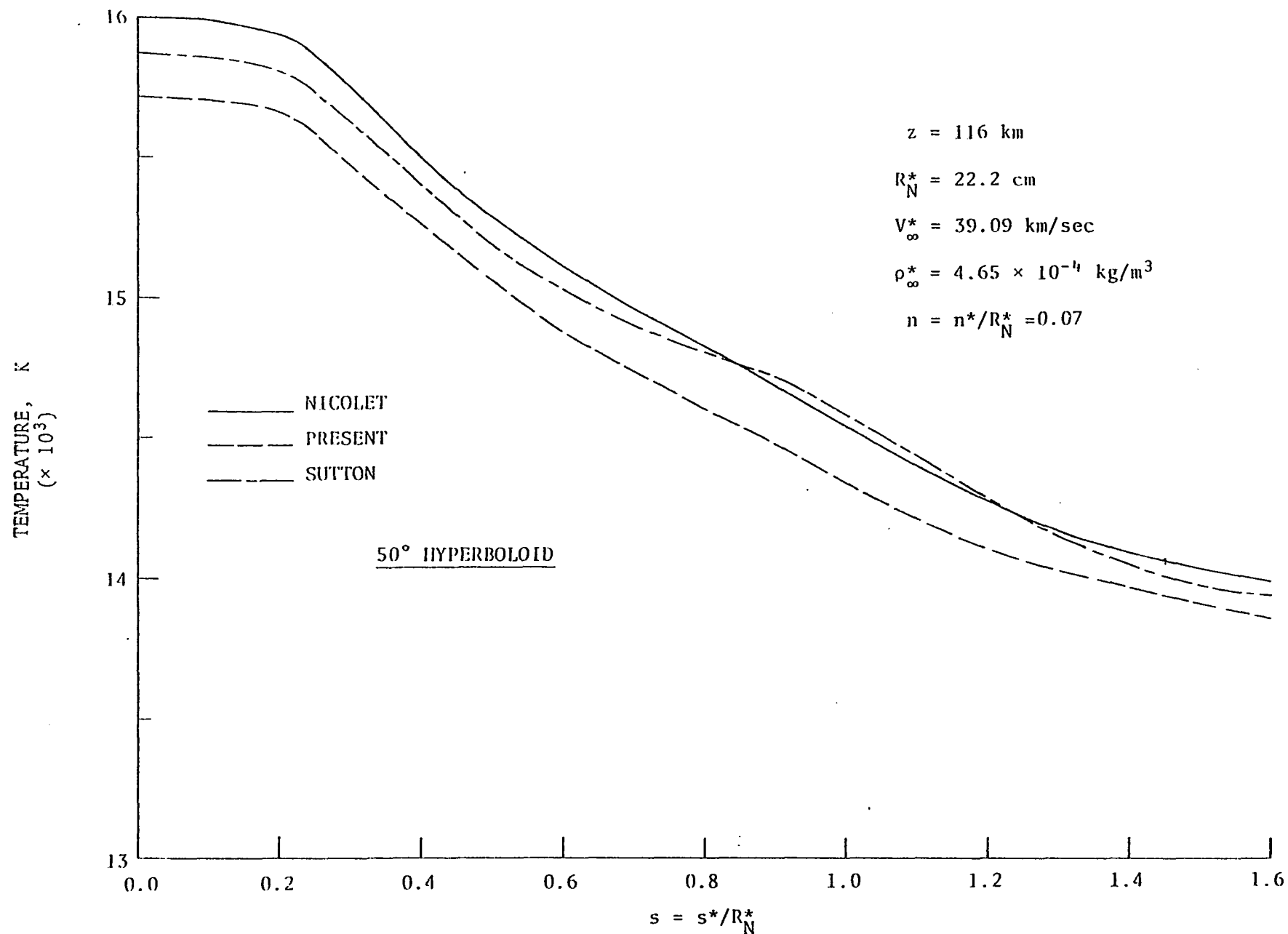


Fig. 15 Temperature distribution just behind the shock ($n = 0.07$) with distance along the body surface (50-degree hyperboloid, $Z = 116 \text{ km}$).

agreement between the three radiation models. The results of the present model are within 1.4 percent of the results of Nicolet's model. As would be expected, maximum difference in results occurs at the stagnation streamline.

The shock standoff variation with distance along the body surface for entry conditions at $Z = 116$ km is shown in Fig. 16. As was the case with the 55-Degree sphere cone, the present model is seen to over-estimate the results in comparison to the other models.

The radiative heating rate along the body surface is illustrated in Figs. 17 to 19 for different entry conditions. For this body geometry also, the maximum heating occurs at the stagnation point. For $Z = 116$ km, results presented in Fig. 17 indicate that the present model underpredicts the heating rate by a maximum of about 13 percent when compared with Nicolet's model. For higher free-stream density, the results presented in Fig. 18 show smaller differences in the results of various radiation models. For entry conditions at $Z = 131$ km, results presented in Fig. 19 indicate that heat transferred to the body is significantly lower. This is because of lower free-stream density and pressure. As was the case with the 55-degree sphere cone at this altitude, the difference between the present and Nicolet's results is relatively higher.

It is found that use of the present model reduces the computational time significantly. The use of this model is recommended for simple parametric study. However, the use of the present model has its limitations. For problems with varying shock-layer compositions and large temperature variations, a suitable empirical correlation has to be developed from the detailed model to make the present model more versatile and accurate.

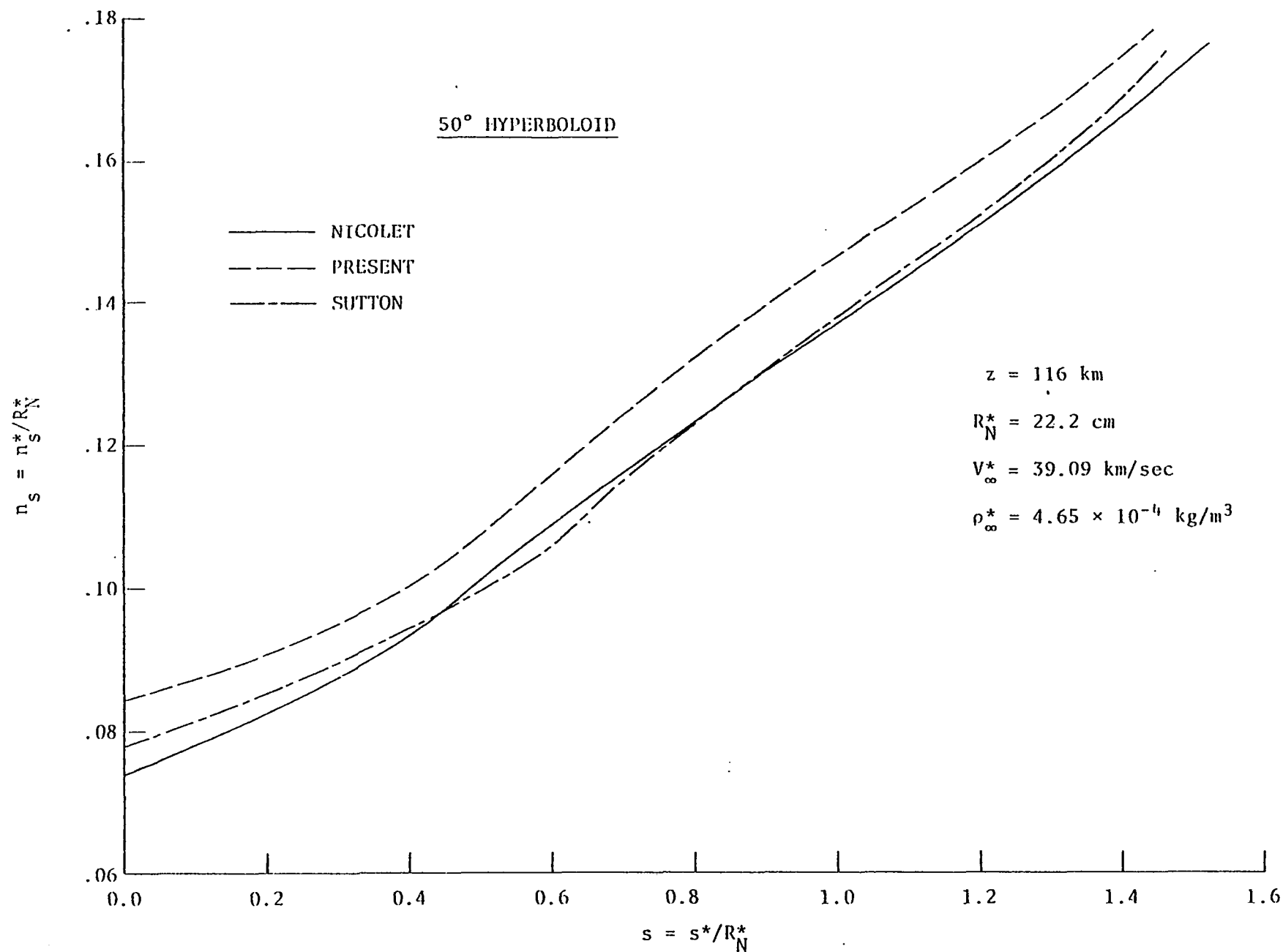


Fig. 16 Shock standoff variation with distance along the body surface (50-degree hyperboloid, $Z = 116 \text{ km}$).

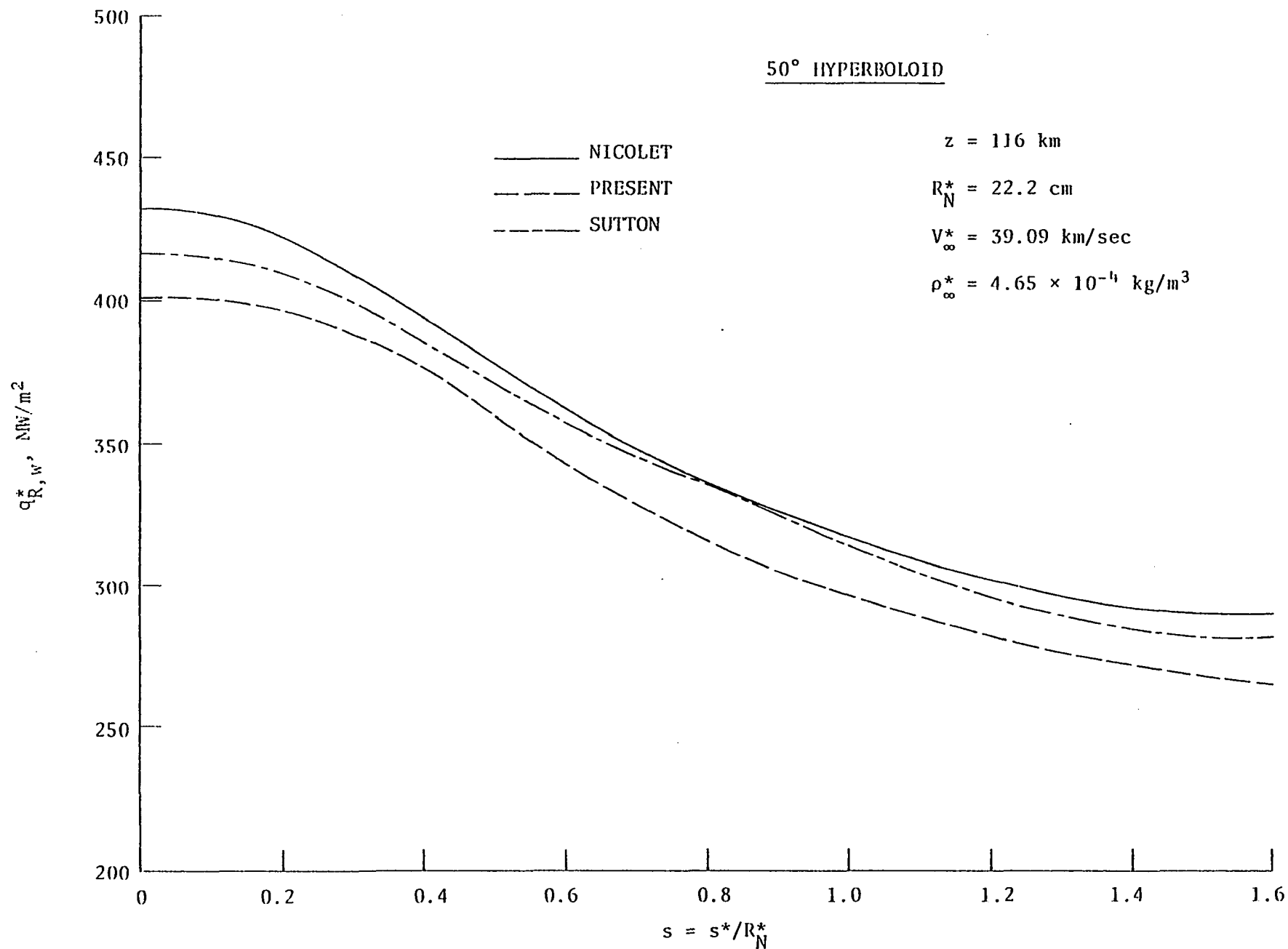


Fig. 17 Radiative heating along the body for entry conditions at $Z = 116 \text{ km}$ (50-degree hyperboloid).

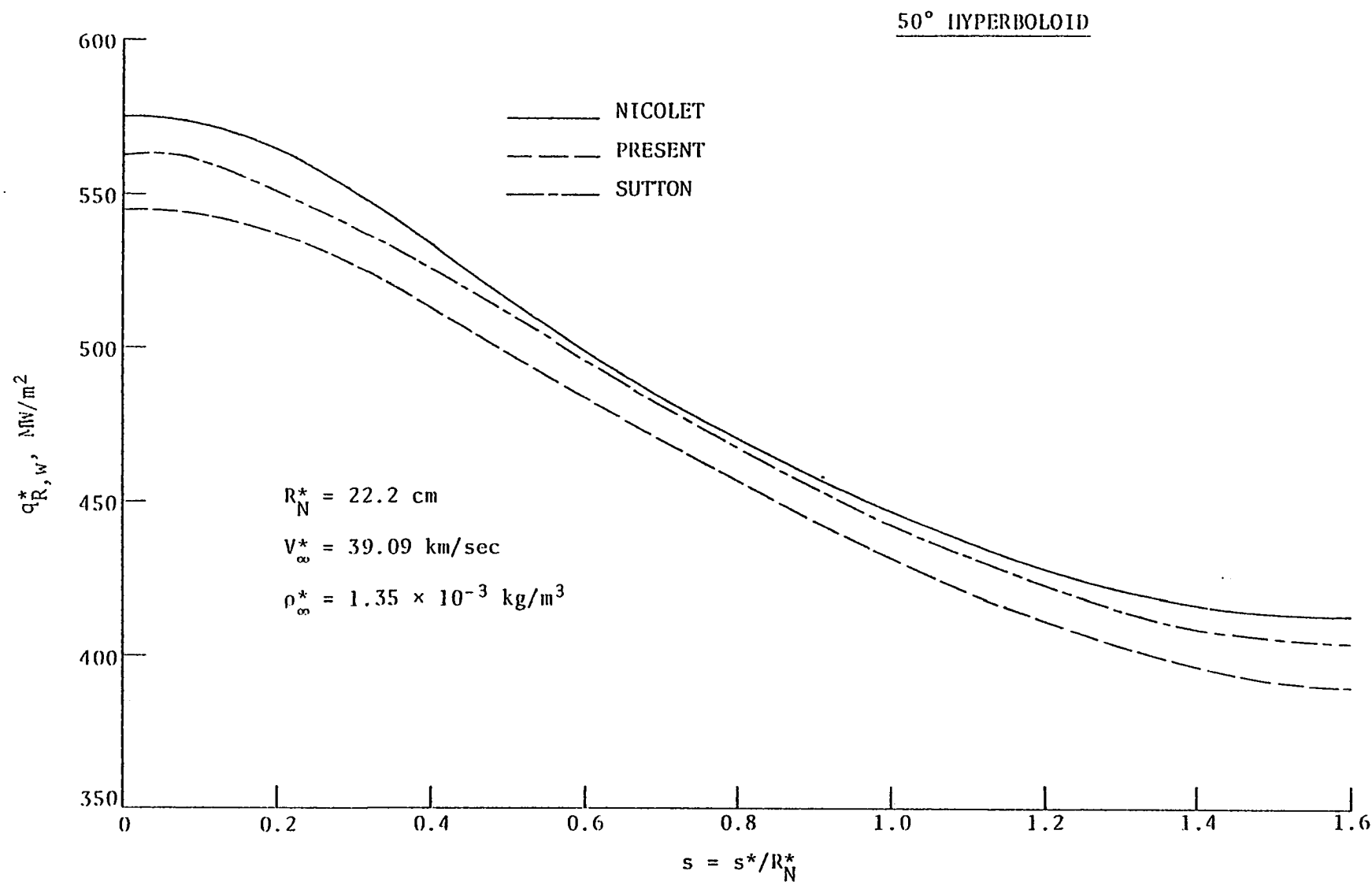


Fig. 18 Radiative heating along the body for free-stream conditions at $Z = 116 \text{ km}$ (50-degree hyperboloid).

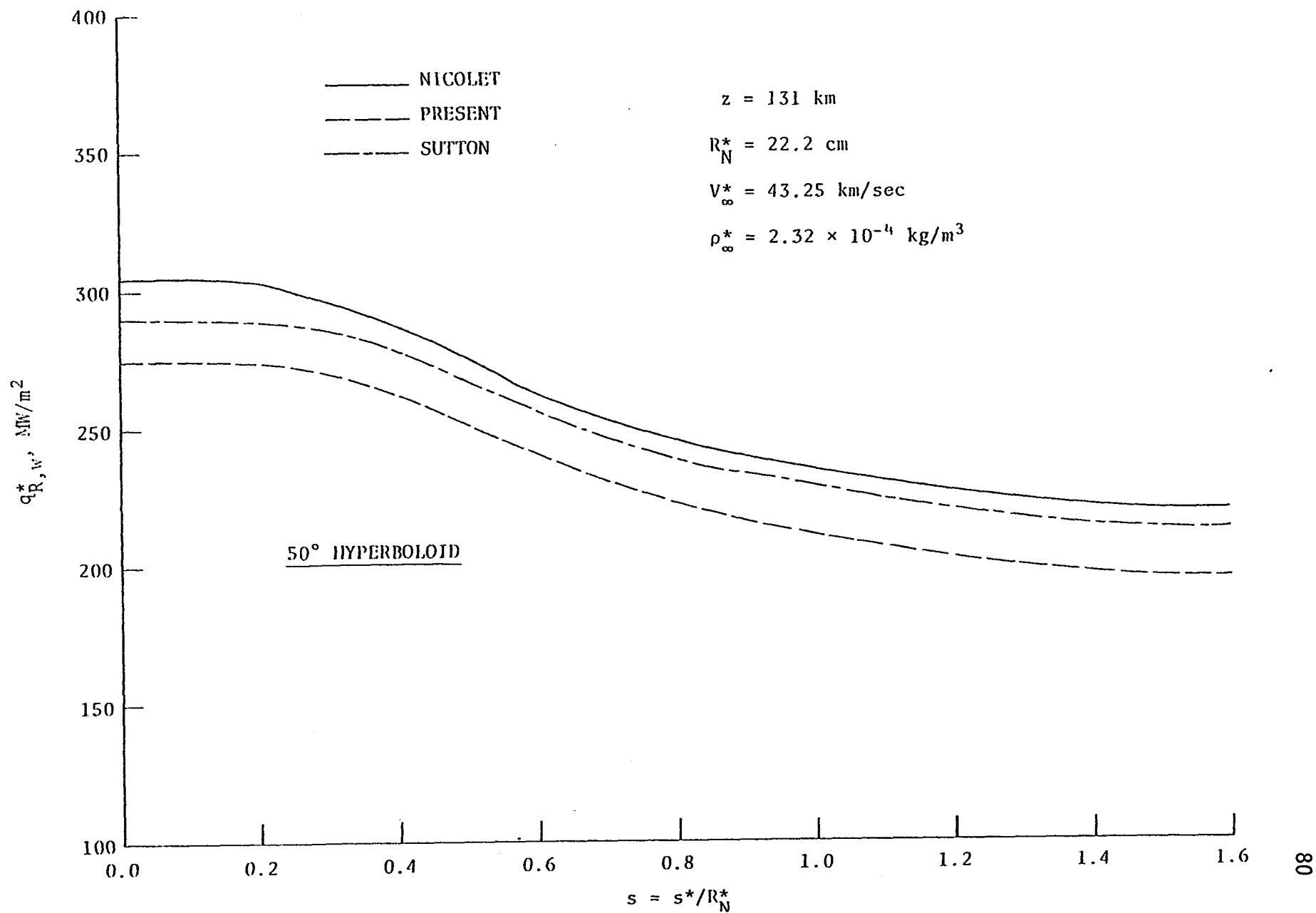


Fig. 19 Radiative heating along the body for entry conditions at $Z = 131 \text{ km}$ (50-degree hyperboloid).

7.2 Influence of NLTE Radiation Without Ablation Injection

Specific results obtained by using the NLTE formulation for the radiative transport, as described by Eqs. (3.40) - (3.42), are presented in this section. The governing Eqs. (2.6) - (2.13) were used to solve the shock-layer flow which was considered to be viscous and in chemical equilibrium. The effect of ablation mass injection into the flow was neglected. In this section, equilibrium radiative transport solutions are presented along with the NLTE results for comparative purpose. For this study, the entry bodies considered are a 50-degree hyperboloid and a 55-degree sphere cone which enter the Jovian atmosphere at zero-degree angle of attack. In both cases, the body nose radius, R_N^* , is taken to be 22.2 cm. The body surface is assumed to be gray having a surface emittance of 0.8, and the wall temperature, T_w , is taken to be constant at 4,200 K. The variation of the nonequilibrium absorption coefficient (as compared to the equilibrium values) is shown in Fig. 20 at a temperature of 15,950 K. Within the confines of assumptions made in this study, the equilibrium and nonequilibrium absorption coefficients are found to be the same beyond 10 eV. The shaded portion in the figure represents the decrease in the absorption coefficient values as a result of increase in the population of higher energy levels.

7.2.1 NLTE Results for a 50-Degree Hyperboloid

The variation of collisional relaxation time across the shock layer is shown in Figs. 21a to 21c for three different entry conditions. Figure 21a shows the results for combined H-H and 0.5 H - 0.5 H₂ and H⁺ - H⁺ collisions, the results indicate that in all three cases the

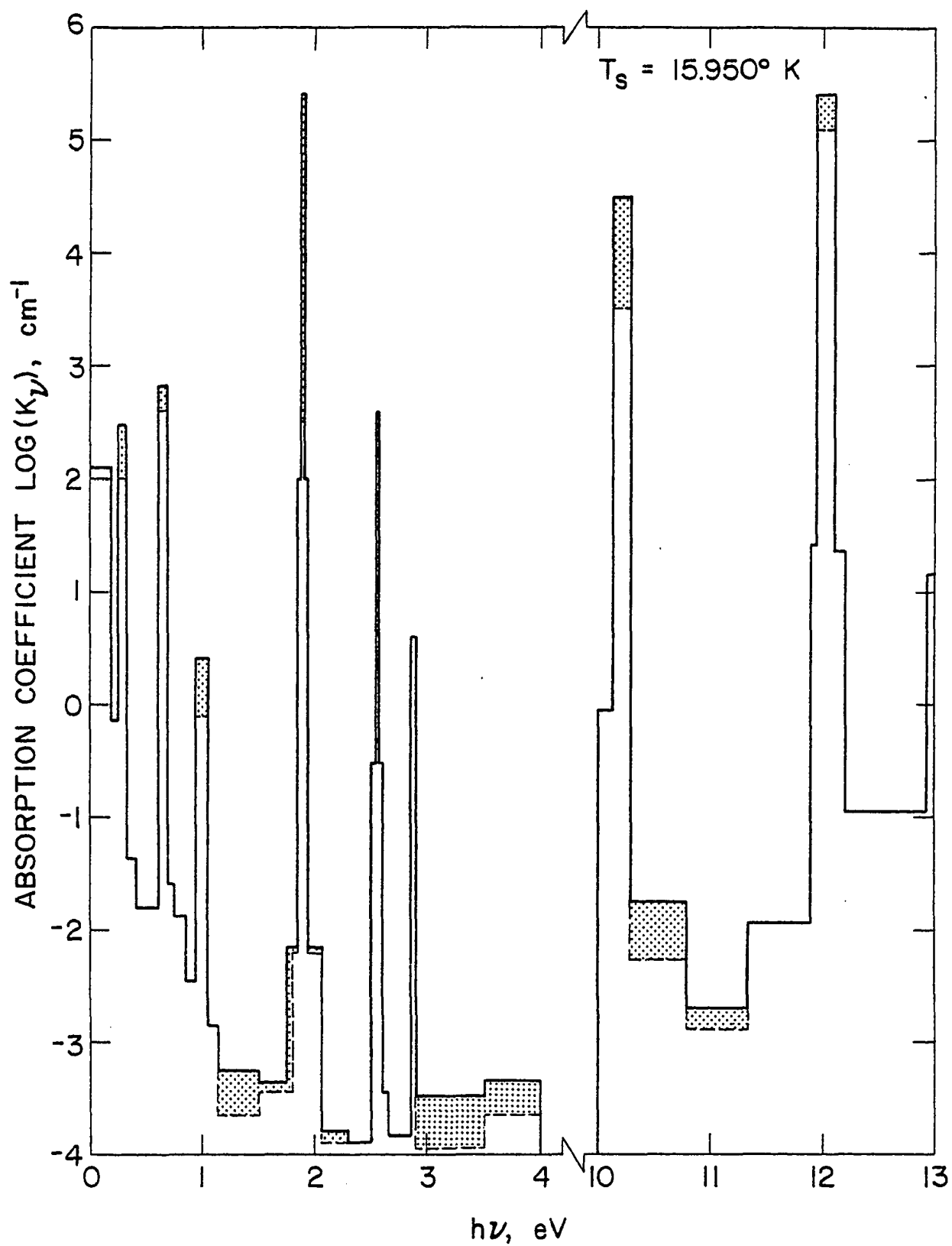


Fig. 20 Equilibrium and nonequilibrium absorption coefficients for two-level energy transitions.

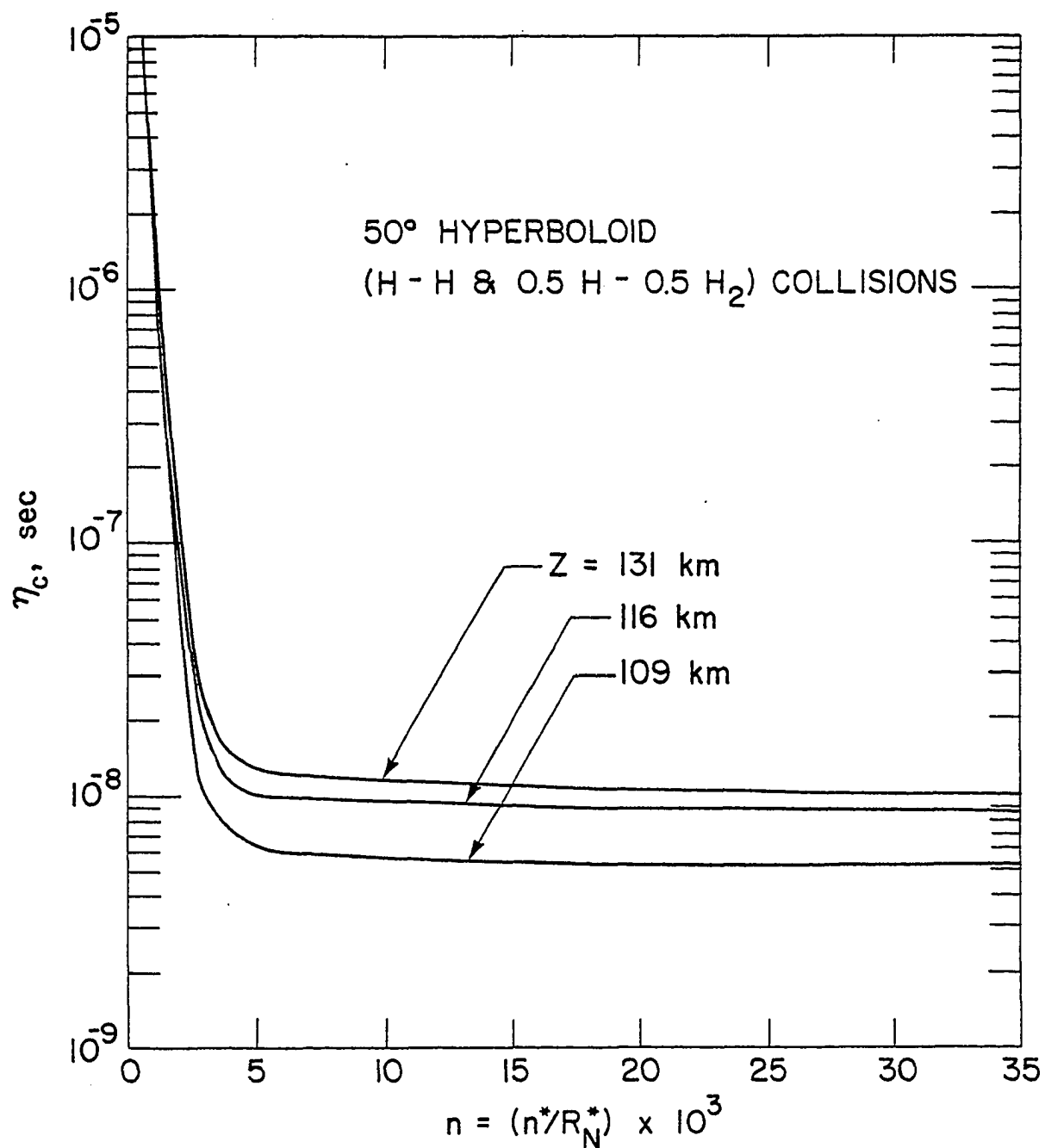


Fig. 21a Variation of relaxation time across the shock-layer for H-H and 0.5 H - 0.5 H₂ collisions.

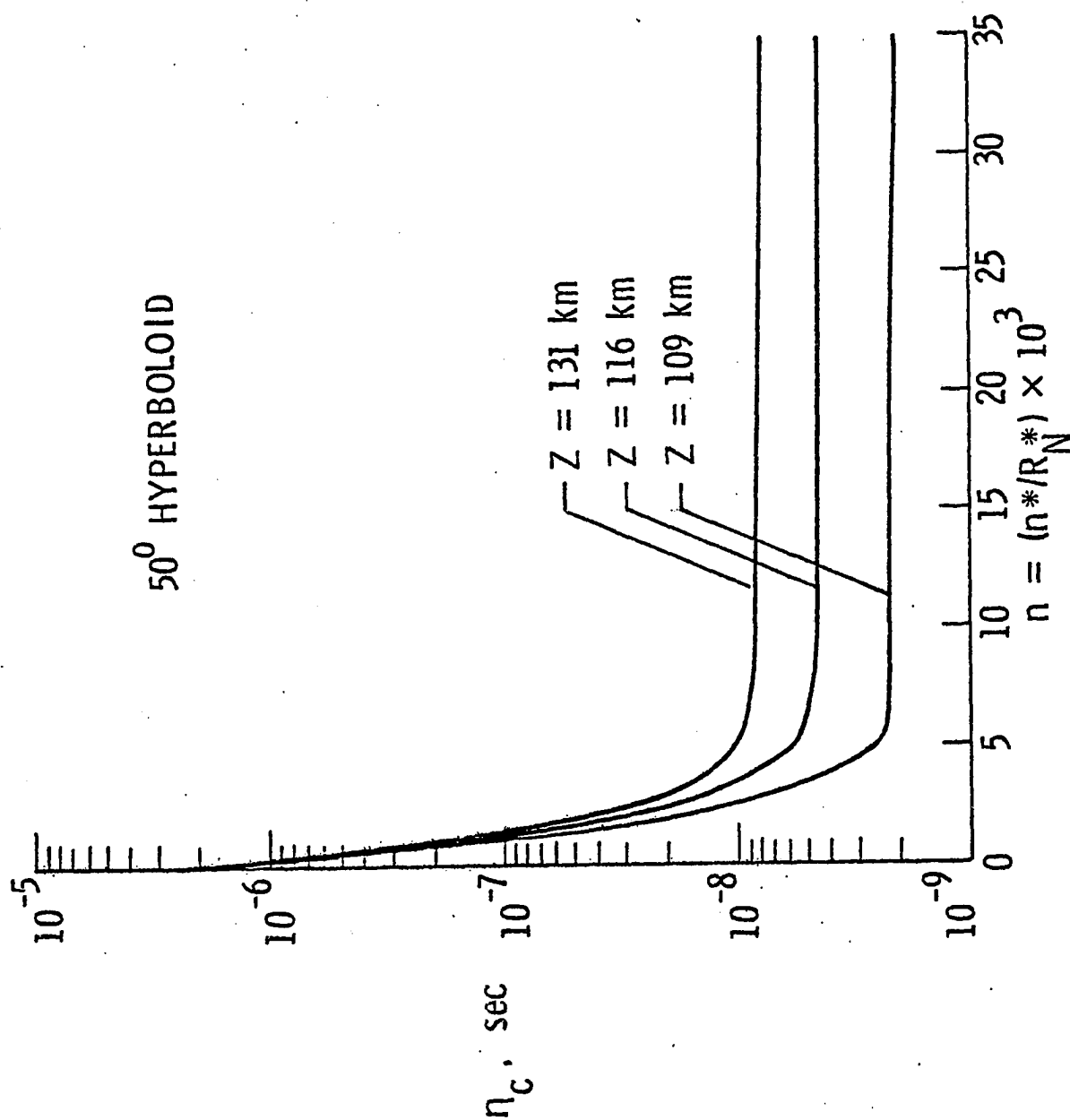


Fig. 21b Variation of relaxation time across the shock-layer for H-H and $H^+ - H^+$ collisions.

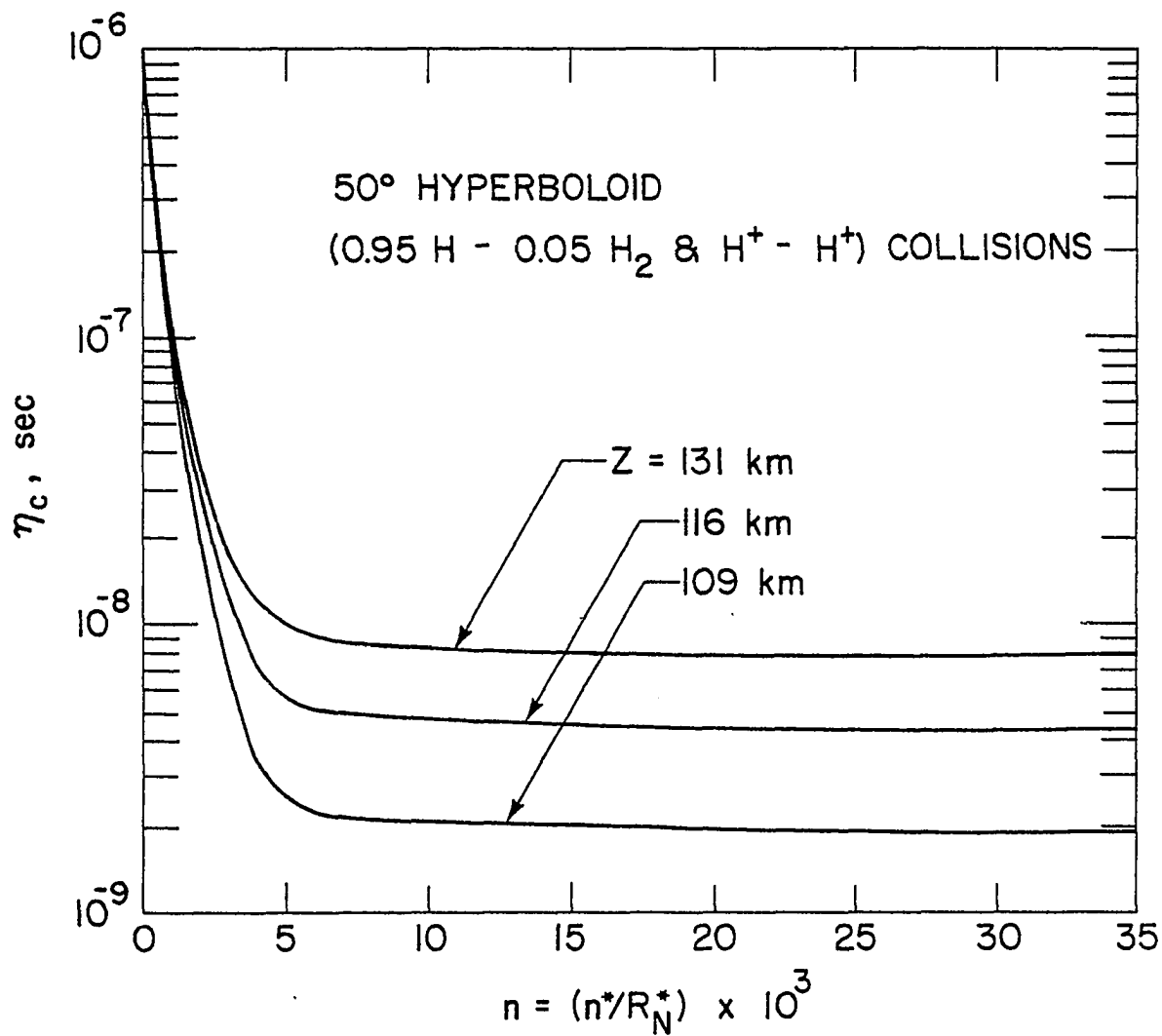


Fig. 21c Variation of relaxation time across the shock-layer for 0.95 H - 0.05 H₂ and H⁺ - H⁺ collisions.

relaxation time does not vary significantly across the shock layer except very close to the body. Thus, higher NLTE effects will be expected in regions closer to the wall where the assumption of chemical equilibrium usually is justified [8]. Since relaxation times are comparatively longer for higher entry altitudes, one would expect the NLTE effects to be greater at higher altitudes. The results presented in Fig. 21a for combined H-H and $0.5 \text{ H} - 0.5 \text{ H}_2$ collisions, of course, are not representative of the results for the actual shock-layer collisional processes; they are presented here only for comparative purposes. The results of the other two collisional processes are found to be very close (Figs. 21b and 21c), and they do represent very nearly the results of actual shock-layer collisional processes.

For the entry condition at $Z = 116 \text{ km}$, the temperature distribution along the stagnation streamline is illustrated in Figs. 22a and 22b. The results in Fig. 22a are for combined H-H and $\text{H}^+ - \text{H}^+$ collisions and in Fig. 22b for $0.95 \text{ H} - 0.05 \text{ H}_2$ and $\text{H}^+ - \text{H}^+$ collisions; the two sets of results are found to be almost identical. The results clearly indicate that the NLTE temperature distribution is consistently lower than the equilibrium temperature. This implies that the shock-layer gas absorbs less energy under NLTE conditions than under equilibrium conditions. This is because under NLTE conditions (where the population ratios of the energy levels deviate from the equilibrium Boltzmann distribution) the number of particles (capable of absorbing the incoming radiation) in the ground state is comparatively less than under equilibrium conditions. The differences between LTE and NLTE results are seen to be lower toward the shock than the body. This is mainly due to direct dependence of the collisional deactivation process on the temperature. The maximum NLTE

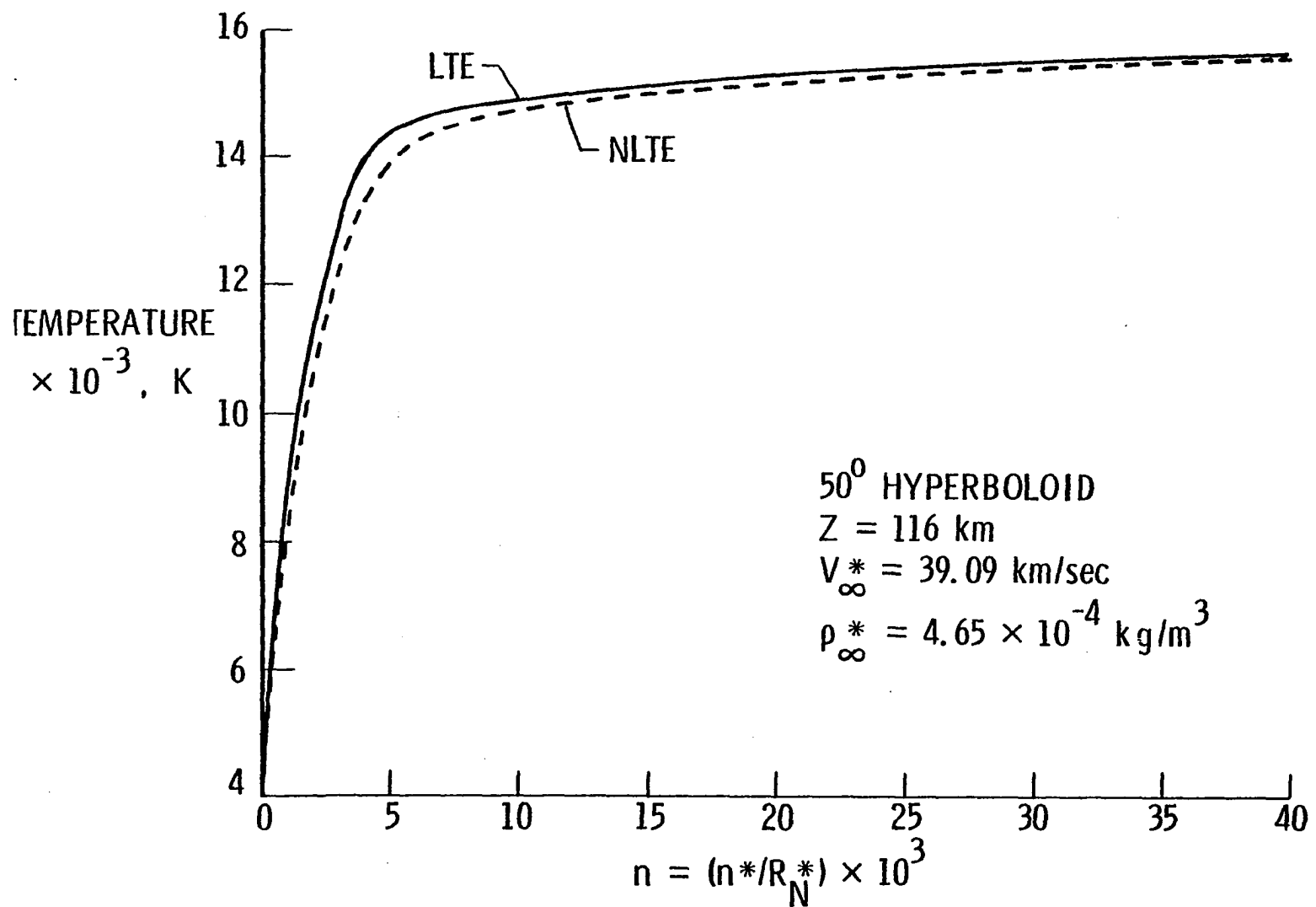


Fig. 22a. Temperature variation across the shock layer for H-H and H⁺ - H⁺ collisions.

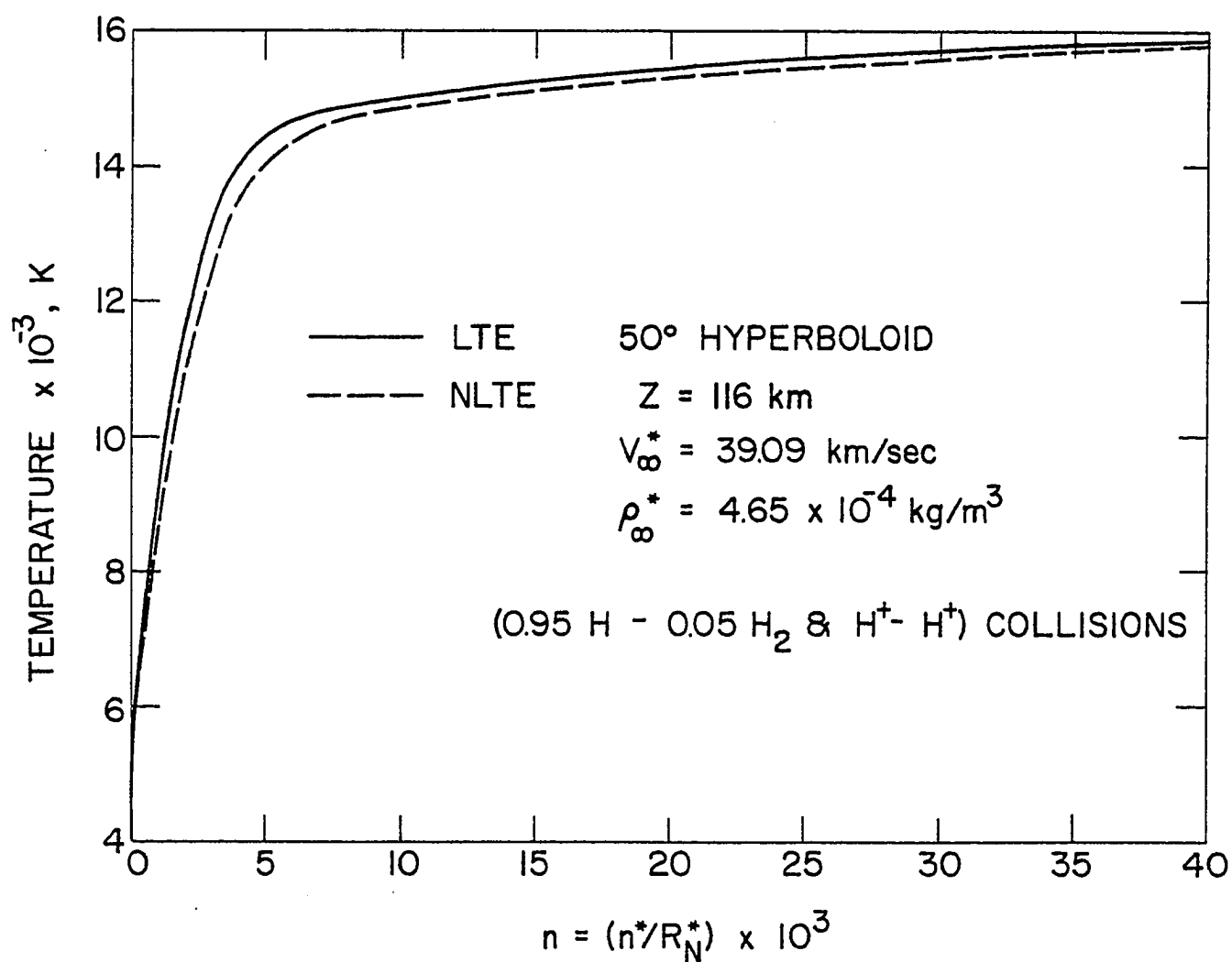


Fig. 22b. Temperature variation across the shock layer for 0.95 H - 0.05 H₂ and H⁺ - H⁺ collisions.

effect, therefore, will occur near the body surface where the collisional deactivation process is slower because of the lower temperature (see also the results presented in Fig. 21).

For the entry conditions at $Z = 116$ km, the temperature distributions along the body are shown in Fig. 23 for two locations in the shock layer. The NLTE results were obtained by considering the combined $H-H$ and H^+-H^+ collisional process. In the region close to the shock ($n = 0.068$), the differences between the LTE and NLTE temperatures are negligible (less than 0.1 percent). On the otherhand, at a location closer to the body ($n = 0.00012$), the differences are significantly larger: a difference of about 6.8 percent is noted at the stagnation point. Since temperature decreases in the direction of the s coordinate, the NLTE influence is found to be greater at locations away from the stagnation streamline.

For the entry conditions at $Z = 116$ km, the shock-standoff variation with distance along the body surface is shown in Fig. 24. Since the shock-standoff distance is mainly influenced by the entry conditions and the shape of the entry body, the conditions of NLTE in the shock layer do not have any effect on its variation.

For entry conditions at $Z = 109$ km, the LTE and NLTE radiative heating along the body are illustrated in Fig. 25. The NLTE results were obtained by considering the combined $H-H$ and H^+-H^+ collisional process. The results simply indicate that the NLTE heating is consistently lower than the LTE heating all along the body. Since the number density of participating particles is relatively higher at lower altitudes, larger NLTE effects would be expected at altitudes higher than $Z = 109$ km.

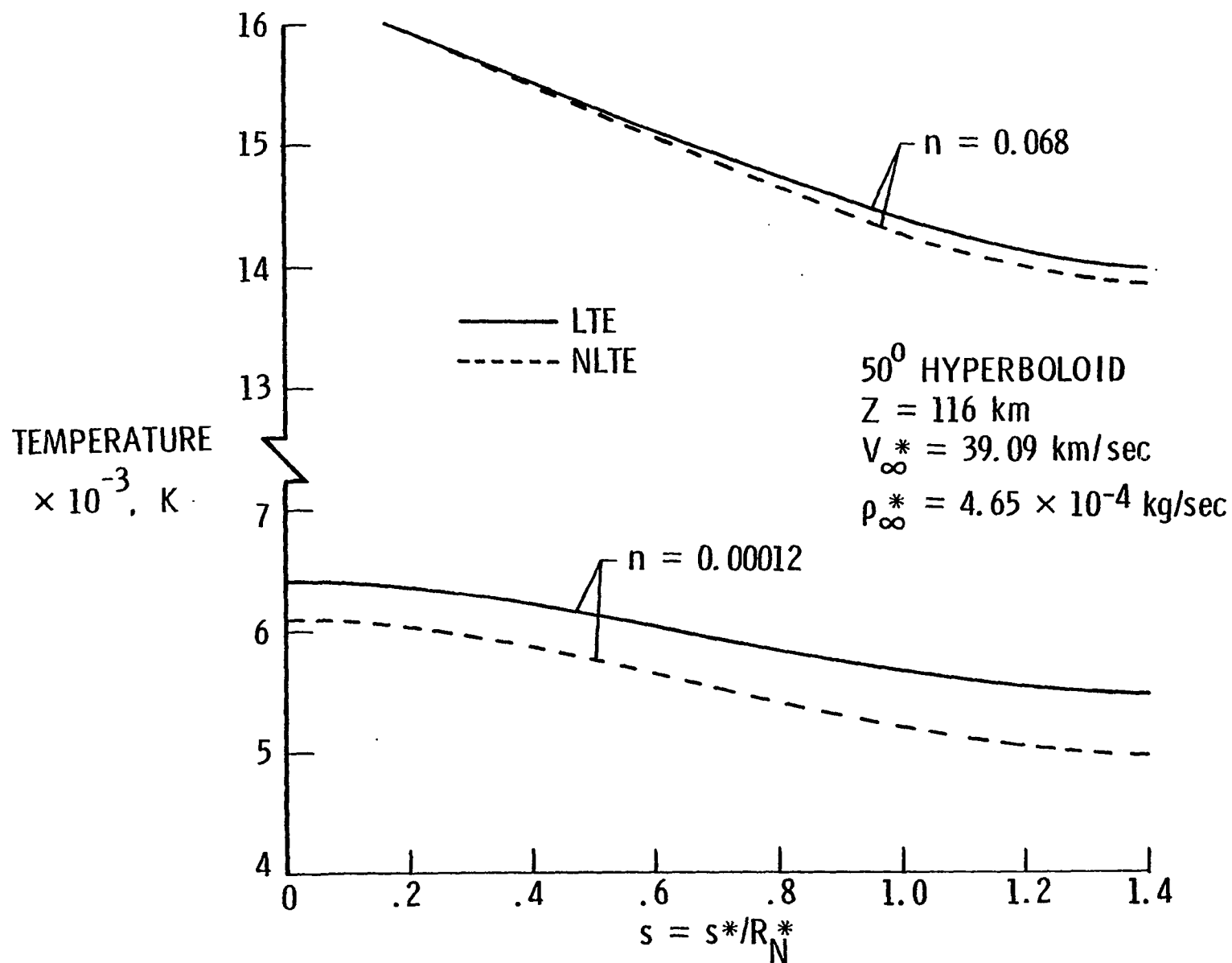


Fig. 23 Temperature variation along the body for two locations in the shock layer, H-H and $H^+ - H^+$ collisions.

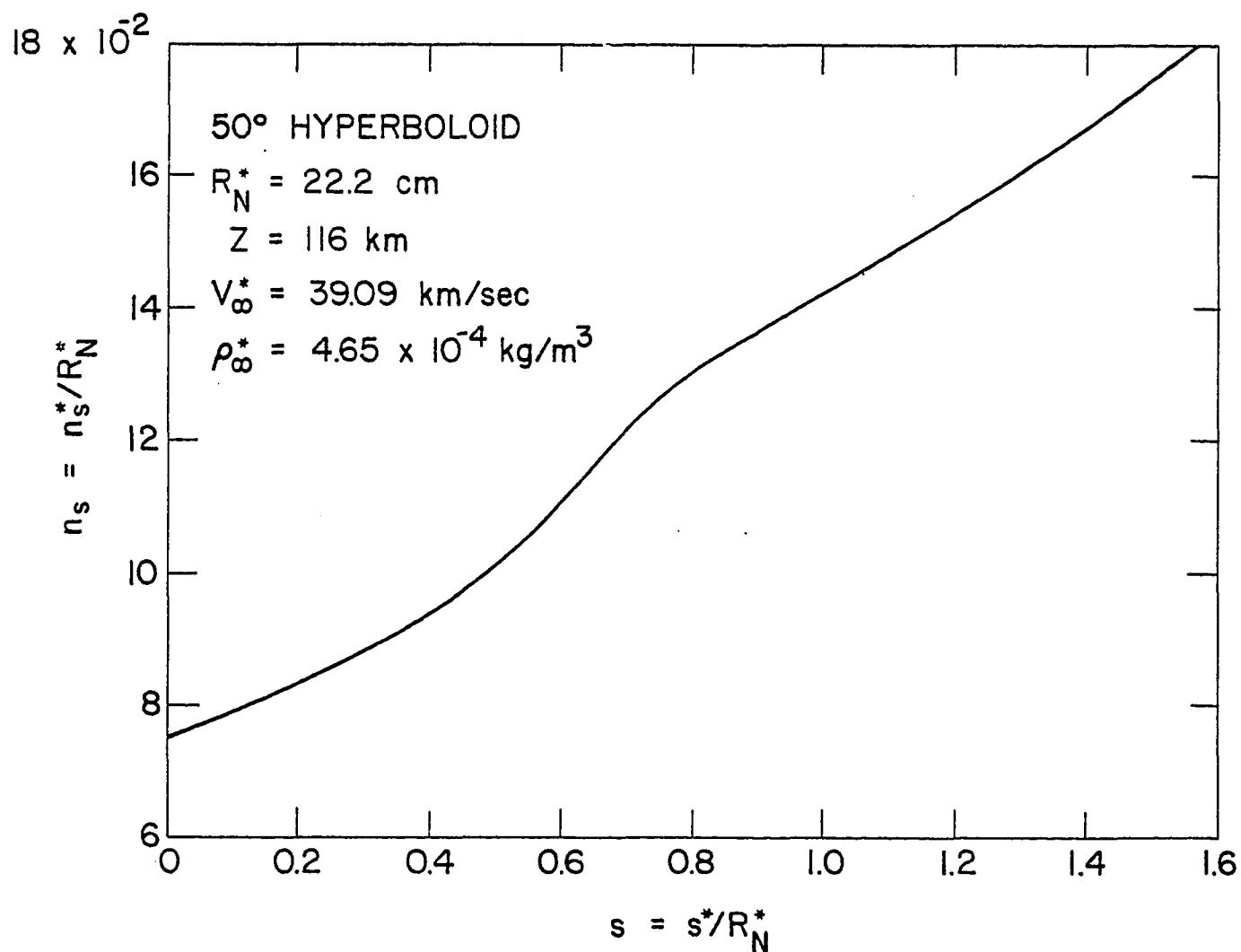


Fig. 24 Shock-standoff variation with distance along the body surface.

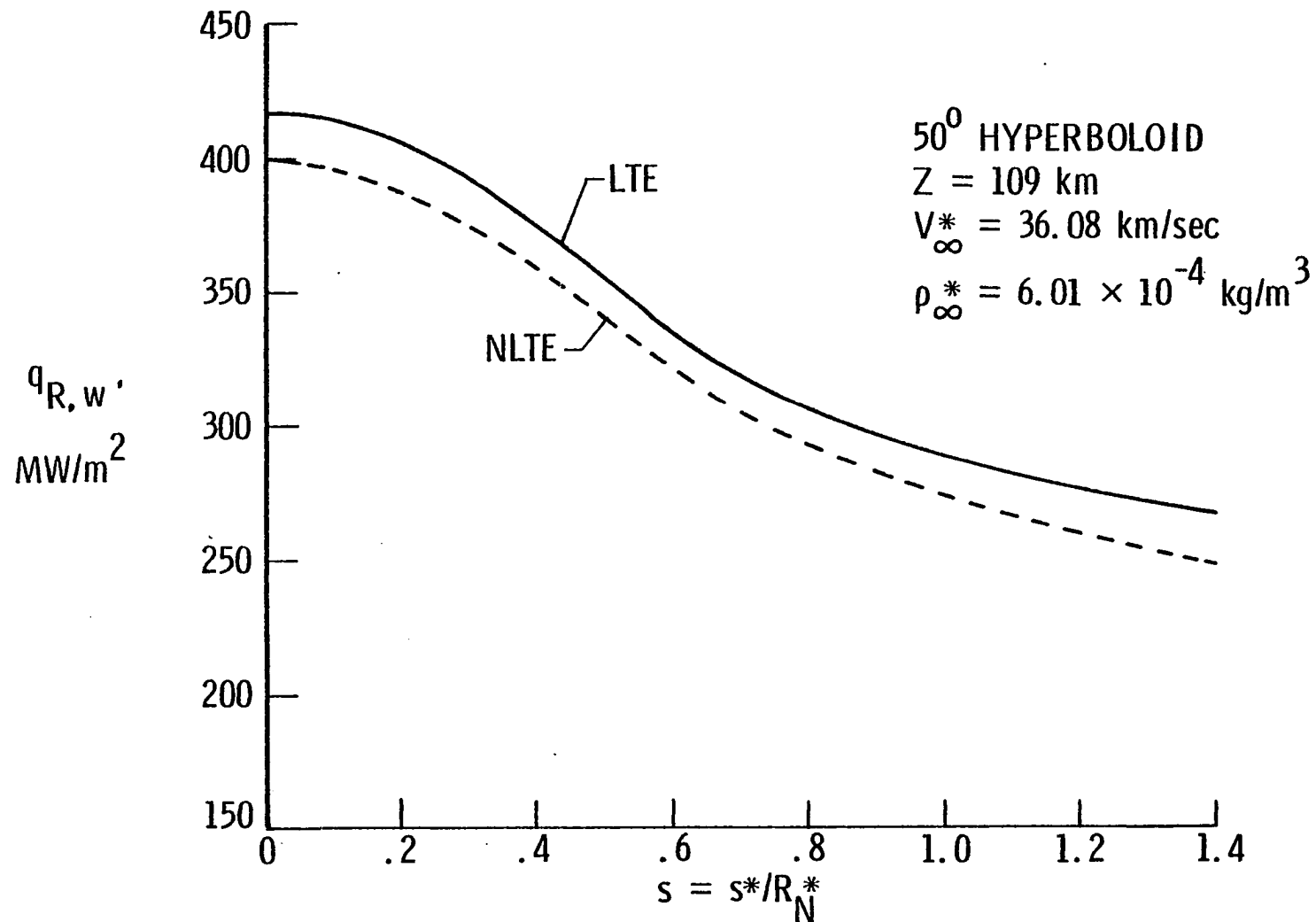


Fig. 25 Radiative heating along the body for entry conditions at $Z = 109 \text{ km}$, H-H and $\text{H}^+ - \text{H}^+$ collisions.

For the peak heating entry conditions (i.e., for $Z = 116$ km), the LTE and NLTE results of radiative heating along the body are illustrated in Fig. 26. In order to assess the influence of various deactivation processes, the NLTE results have been obtained by considering five different collisional relaxation times. This is essential because the exact nature of the collisional deactivation process, which actually occurs in the shock-heated gas, is not known. It is evident from the figure that the NLTE results obtained by considering only the H^+-H^+ collisions are very close to the LTE results. Consequently it may be concluded that in a fully ionized plasma the assumption of LTE is justified. The NLTE results obtained by considering only the $0.5 H - 0.5 H_2$ collisions are seen to be significantly lower than the LTE results. This, however, does not represent a physically realistic situation for the shock-layer gas (because of a very low number density of hydrogen molecules); the results are presented here only for comparative purpose. Probably the more realistic collisional process for the shock-layer gas may be represented by the combined $H-H$ and H^+-H^+ or $H-H_2$ collisions. The NLTE results obtained by considering the combined relaxation times of these collisions are seen to be much lower than the LTE results all along the body. The maximum NLTE effects are found to be for the case of combined $H-H$ and $0.95 H - 0.05 H_2$ collisions. The difference between LTE and NLTE results for this case is 11 percent at the stagnation point. The case of the combined $H-H$ and H^+-H^+ collisional process (which is very close to the case of the combined $0.95 H - 0.05 H_2$ and H^+-H^+ process), however, appears to be more physically convincing. For this case, a comparison of results presented in Figs. 25 and 26 reveals that NLTE effects are significantly higher at $Z = 116$ km than at $Z = 109$ km.

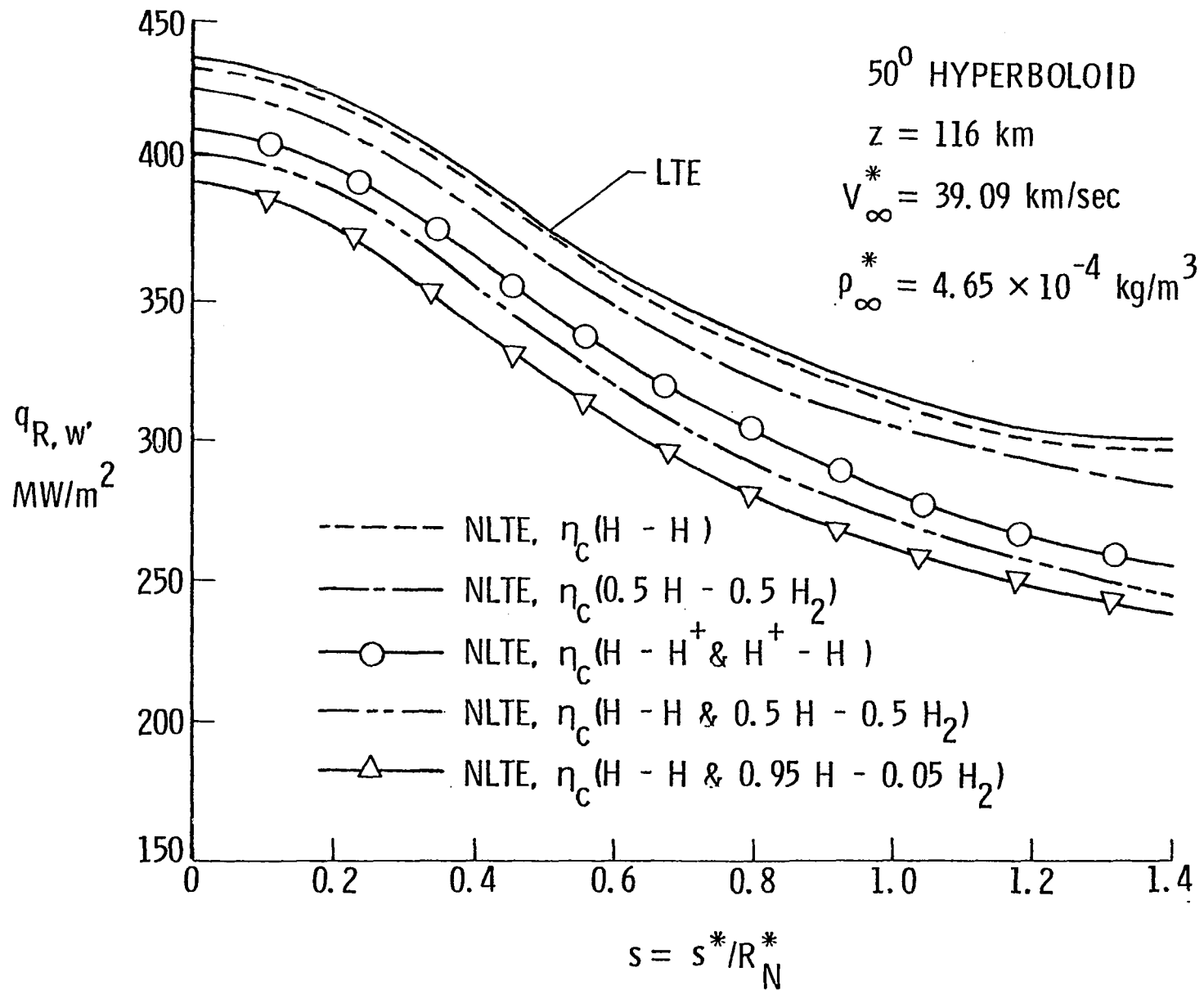


Fig. 26 Radiative heating along the body for entry conditions at $Z = 116 \text{ km}$.

Figure 26 shows a nine percent reduction in radiative heating for this case at the stagnation point. Perhaps an even more convincing process to consider will be the combined $H-H$, H^+-H^+ , and $0.95 H - 0.05 H_2$ collisional process. However, at present no theory is available to calculate the relaxation times of such collisions. The effects of such collisions, of course, will be lower than those for the combined $H-H$ and $0.95 H - 0.05 H_2$ collisions; the results are expected to be closer to the results of the combined $H-H$ and H^+-H^+ collisions.

For entry conditions at $Z = 131$ km, the results of radiative and convective heating along the body are illustrated in Fig. 27. The NLTE results were obtained by considering the combined $H-H$ and H^+-H^+ collisional process. For radiative heating, NLTE results are shown also for two-level energy transitions. The results clearly indicate that, although differences between LTE and NLTE results are small for the convective heating, they are considerably large for the radiative heating. The contributions of higher level energy transitions on NLTE results are seen to be quite small (less than 1.7 percent). Since NLTE affects the convective heating only through a different temperature distribution, the effects are seen to be quite small away from the stagnation point.

Results of LTE and NLTE radiative heating at the stagnation point are shown in Fig. 28 for entry conditions at different altitudes. The NLTE results again are obtained by considering the combined $H-H$ and H^+-H^+ collisions. Once again the NLTE results for two-level energy transitions are presented for comparative purposes. The results show that differences between LTE and NLTE heating rates are larger at higher altitudes. As mentioned earlier, this is because the densities of

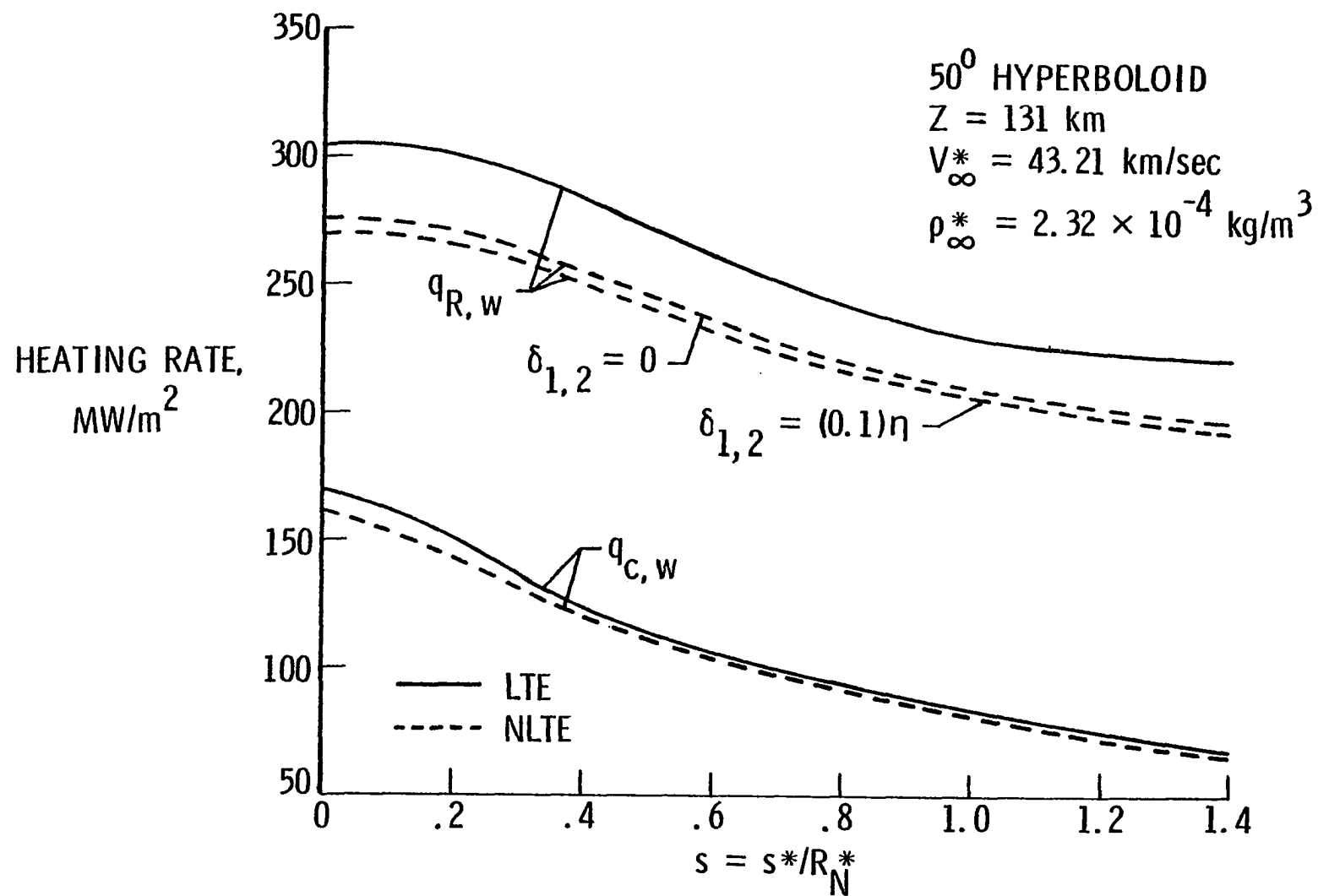


Fig. 27 Radiative and convective heating along the body for entry conditions at $Z = 131 \text{ km}$, H-H and $\text{H}^+ - \text{H}^+$ collisions

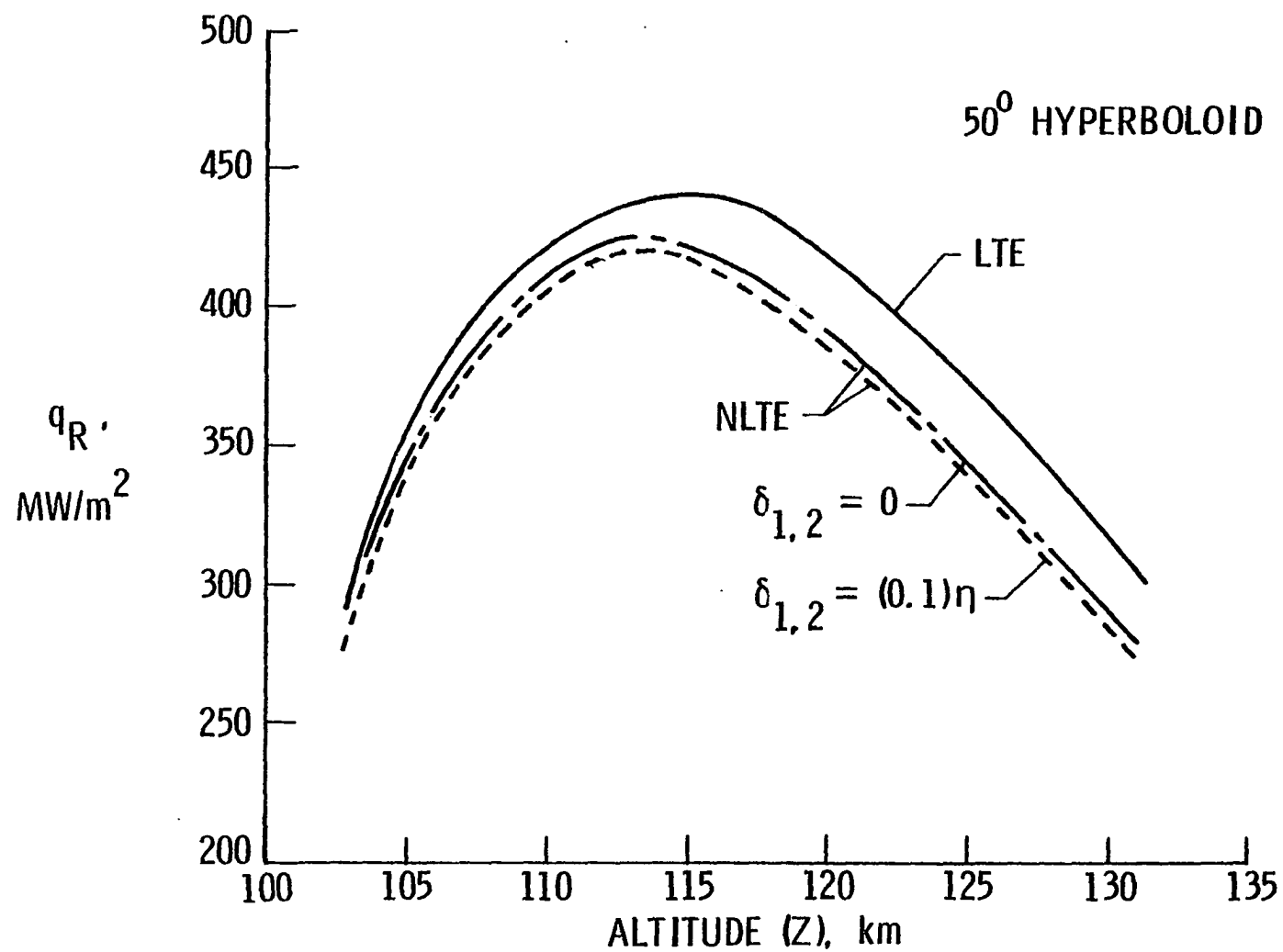


Fig. 28 Stagnation-point radiative heating for different entry altitudes, H-H and H⁺ - H⁺ collisions.

participating species are relatively lower at higher altitudes (lower pressures), and this, in turn, results in longer collisional deactivation times.

7.2.2 NLTE Results for a 55-Degree Sphere Cone

For the 55-degree sphere cone, the radiative heating results for the peak heating conditons are illustrated in Fig. 29. The NLTE results were obtained by considering the combined $H-H$ and H^+-H^+ collisional process. Because of the numerical instability it was possible to obtain accurate NLTE results only up to the tangency point. Obviously, further work is needed to improve the numerical procedure for obtaining the NLTE results toward the downstream regions. In the stagnation region, the results for the sphere cone show essentially the same trend as for the hyperboloid. At the stagnation point, the difference between the LTE and NLTE results for the sphere cone is about the same as for the hyperboloid. This clearly indicates that the NLTE results are not influenced significantly by the changes in forebody shapes. However, further work is needed to make this a definite recommendation because the LTE heating rates are influenced by the shape change [64].

The results presented in this section indicate that, although the relaxation times for collisions between neutral particles decreases with increasing temperature, the reverse is true for the charged particles. It is also noted that the physically realistic collisional process for the shock-layer gas (in the absence of ablative products) is the combined $H-H$ and H^+-H^+ deactivation process. Specific results indicate that NLTE effects are greater closer to the body than near the shock. This is because the NLTE results are influenced strongly by the temperature

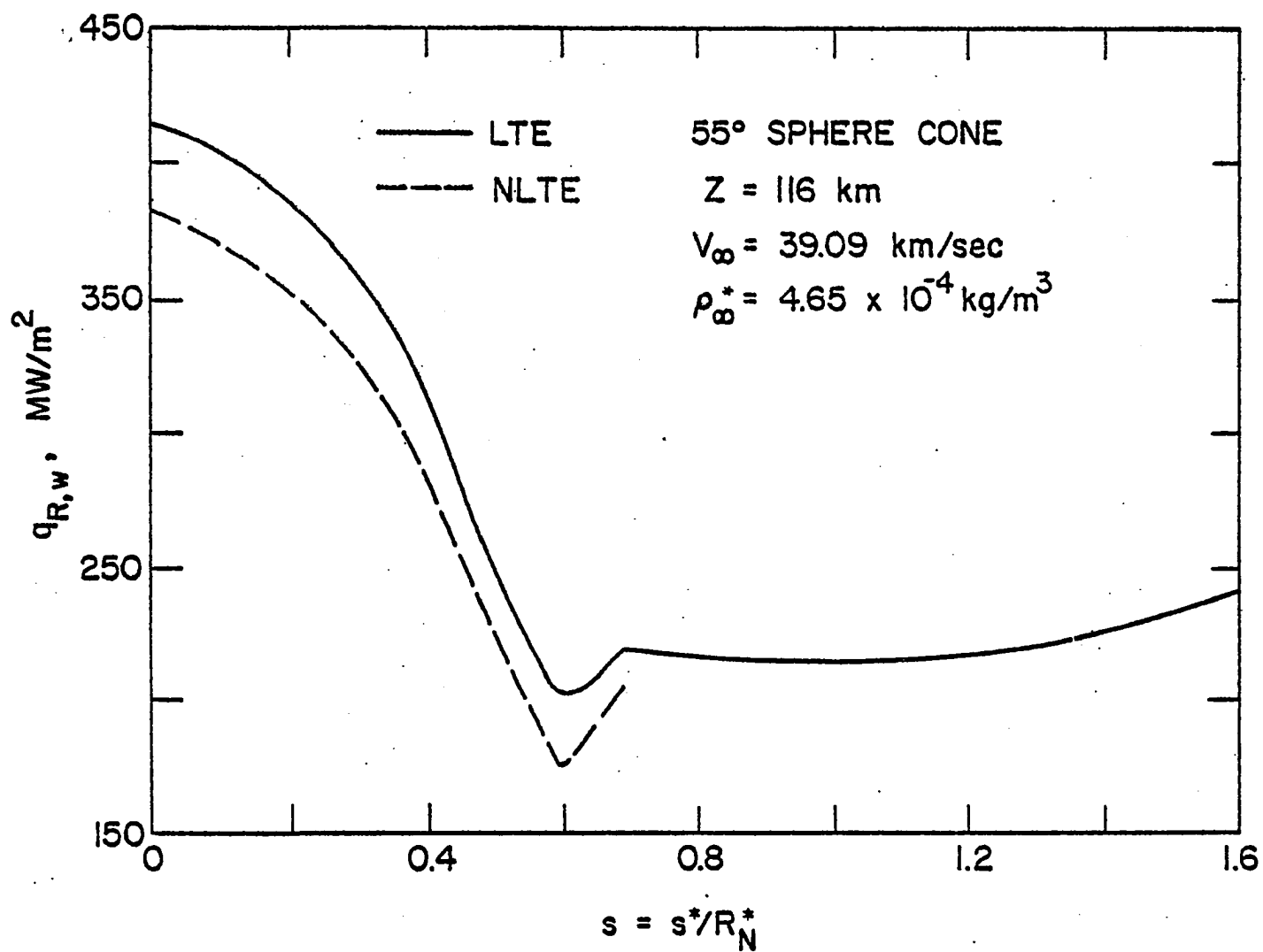


Fig. 29 Radiative heating along the body (55-degree sphere cone) for entry conditions at $Z = 116$ km, H-H and $H^+ - H^+$ collisions.

distribution in the shock layer and the effects are lower at higher temperatures. It is further noted that the contribution of higher level energy transitions on the NLTE results is relatively small for all entry conditions. It is found that the influence of NLTE, in general, reduces the convective and radiative heating to the entry body. Although this effect is small for the convective heating, the radiative heating is influenced significantly. The NLTE effects are greater for higher altitude entry conditions. From a qualitative comparison of the results for a 50-degree hyperboloid and a 55-degree sphere cone (under identical physical and entry conditions), it is noted that the NLTE results are not influenced significantly by the change in the forebody configurations of the entry probe.

7.3 Importance of NLTE Radiation with Ablation Injection

For peak-heating entry conditions, the viscous shock-layer results obtained for a 35-degree hyperboloid (with coupled ablation mass loss from a carbon-phenolic heat shield) are presented in this section. The LTE results for this case are available in [64-68]. For NLTE study, however, it is essential to know the nature of the collisional deexcitation processes and the relaxation time of different shock-layer species in presence of the ablative products. Figure 30 illustrates the important species concentration near the wall influencing the C_2 collisional process. The variation of collisional relaxation time is obtained using Eqs. (4.11) - (4.14) and this is shown in Fig. 4. The radiative lifetimes of the bands that are considered to be in NLTE are also shown in this figure. Unlike the collisional relaxation time, the radiative lifetime is invariant with temperature.

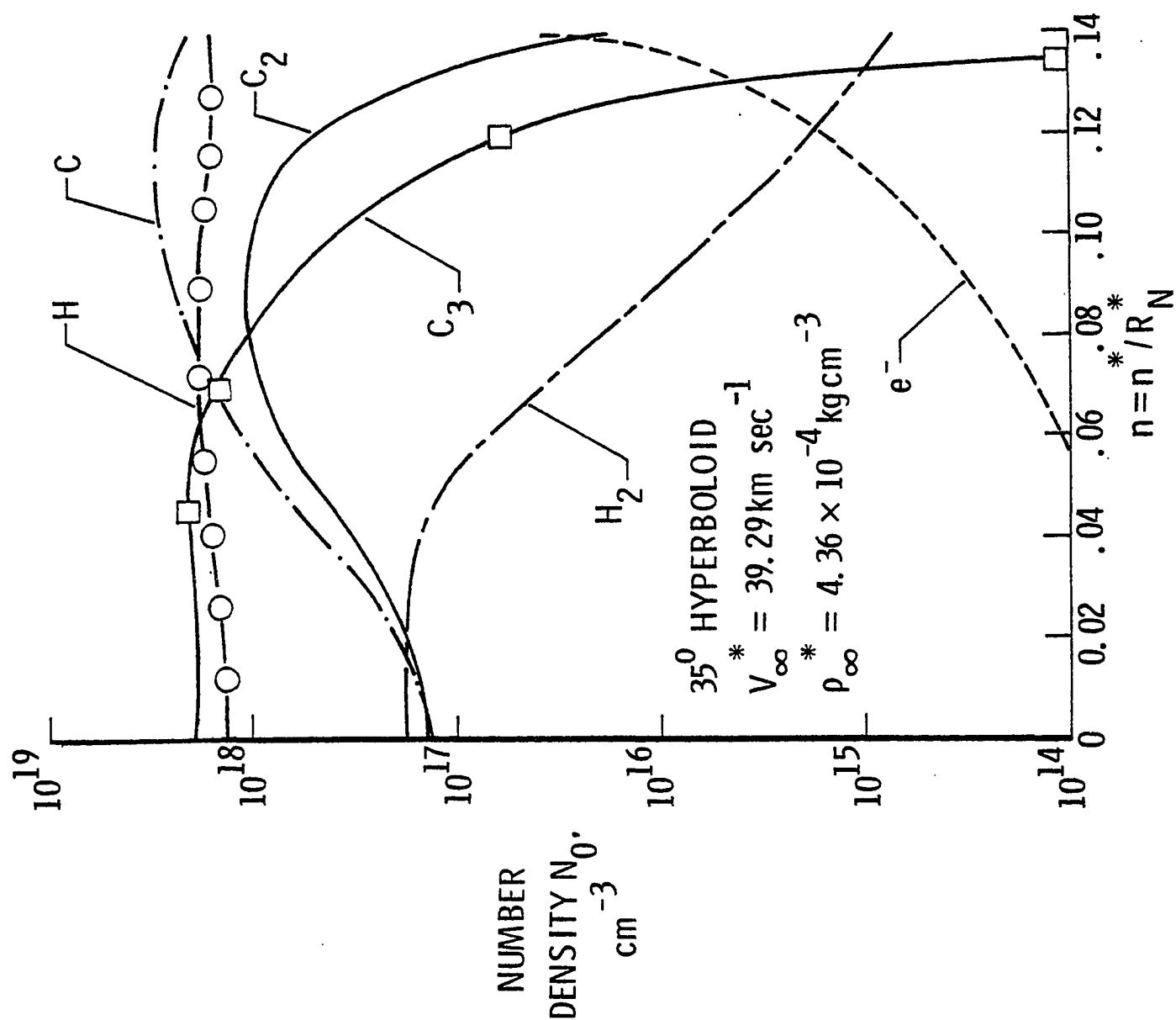


Fig. 30 Species concentration in the vicinity of the wall.

The temperature variation across the shock layer (for location $s = 0$) is shown in Fig. 31 for both LTE and NLTE conditions. Results obtained in the previous section with no mass injection are also shown here for comparison. As would be expected, the shock-layer temperature, in general, are lower in the vicinity of the body in the presence of the ablative products [64,68]. It is seen that the NLTE temperature distribution is lower than the equilibrium values throughout the shock layer. A maximum difference of 5.48 percent is noticed between the two values at $n = 0.13$. The C_2 molecules in the ablation layer (a region in the vicinity of the wall), which absorb less under NLTE conditions, possess less energy than the equilibrium value. This, in turn, results in lower temperature values in the ablation layer and the trend continues in the entire shock layer.

Figure 32 illustrates the density and enthalpy variations across the shock layer for LTE and NLTE conditions. The enthalpy variation has a similar trend as the shock-layer temperature shown in Fig. 31. It was found that NLTE essentially had no influence on the pressure distribution in the shock layer. The density, however, is seen to be significantly higher for the NLTE case. This is a direct consequence of relatively lower NLTE temperatures in the shock layer. A maximum increase in density of about 5.5 percent is noticed at $n = 0.15$. The shock standoff variation with distance along the body surface is shown in Fig. 33 for LTE and NLTE conditions. It is noted that the NLTE results are comparatively higher than the LTE results. A possible reason for this behavior is the combination of enthalpy and density variation in the shock-layer along with the energy loss at the shock for nonequilibrium condition.

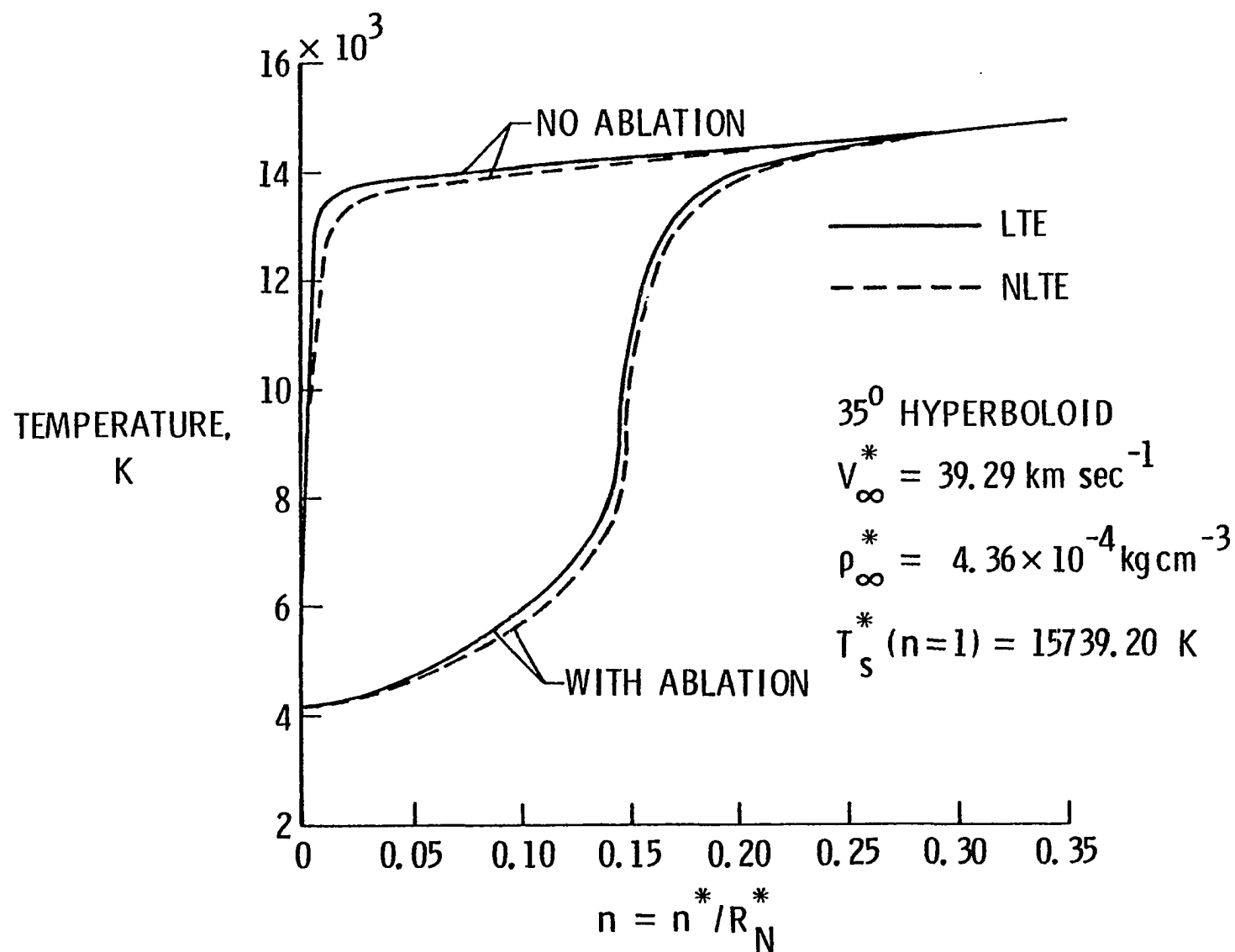


Fig. 31 Temperature distribution across the shock-layer.

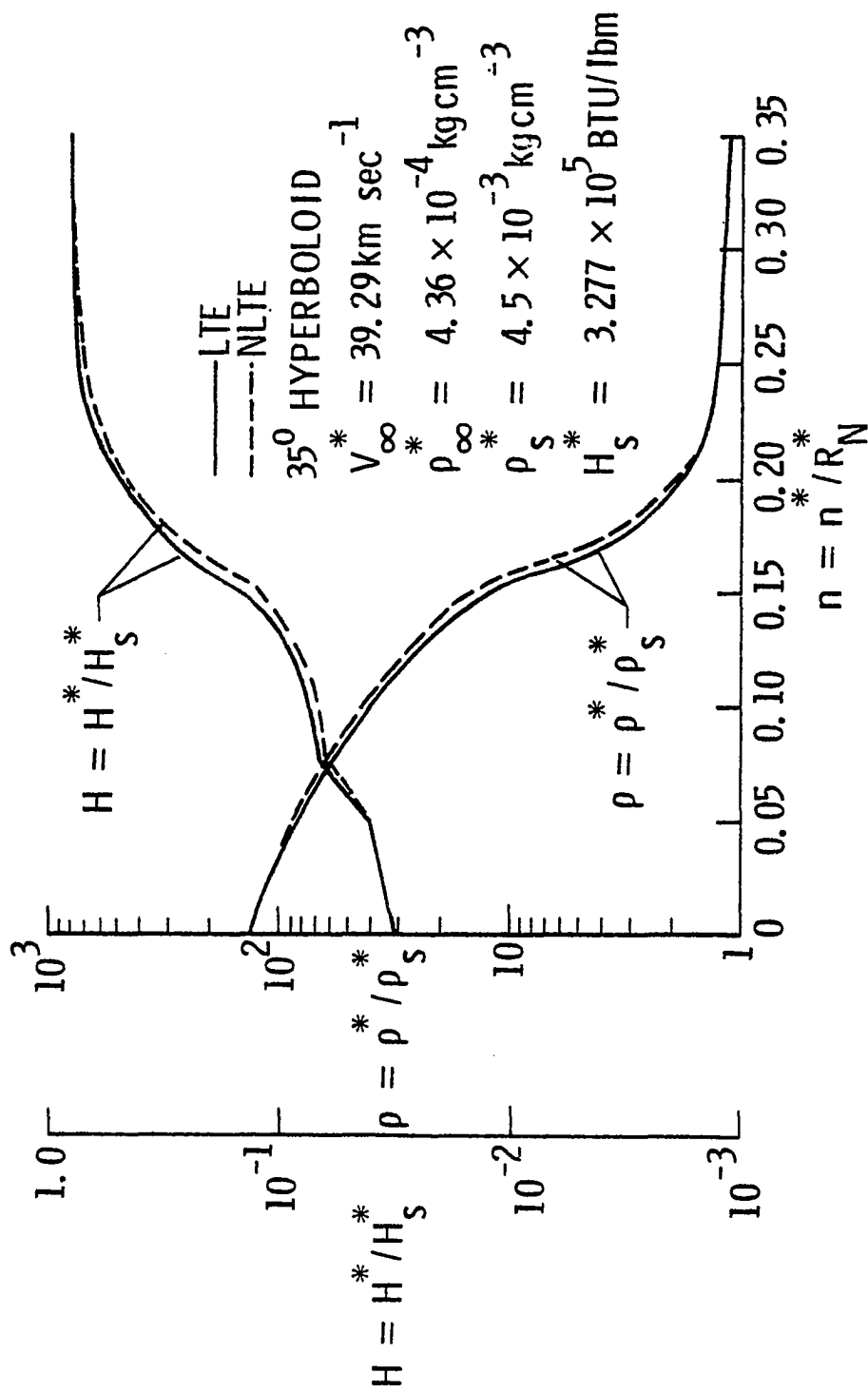


Fig. 32 Enthalpy and density variations across the shock layer

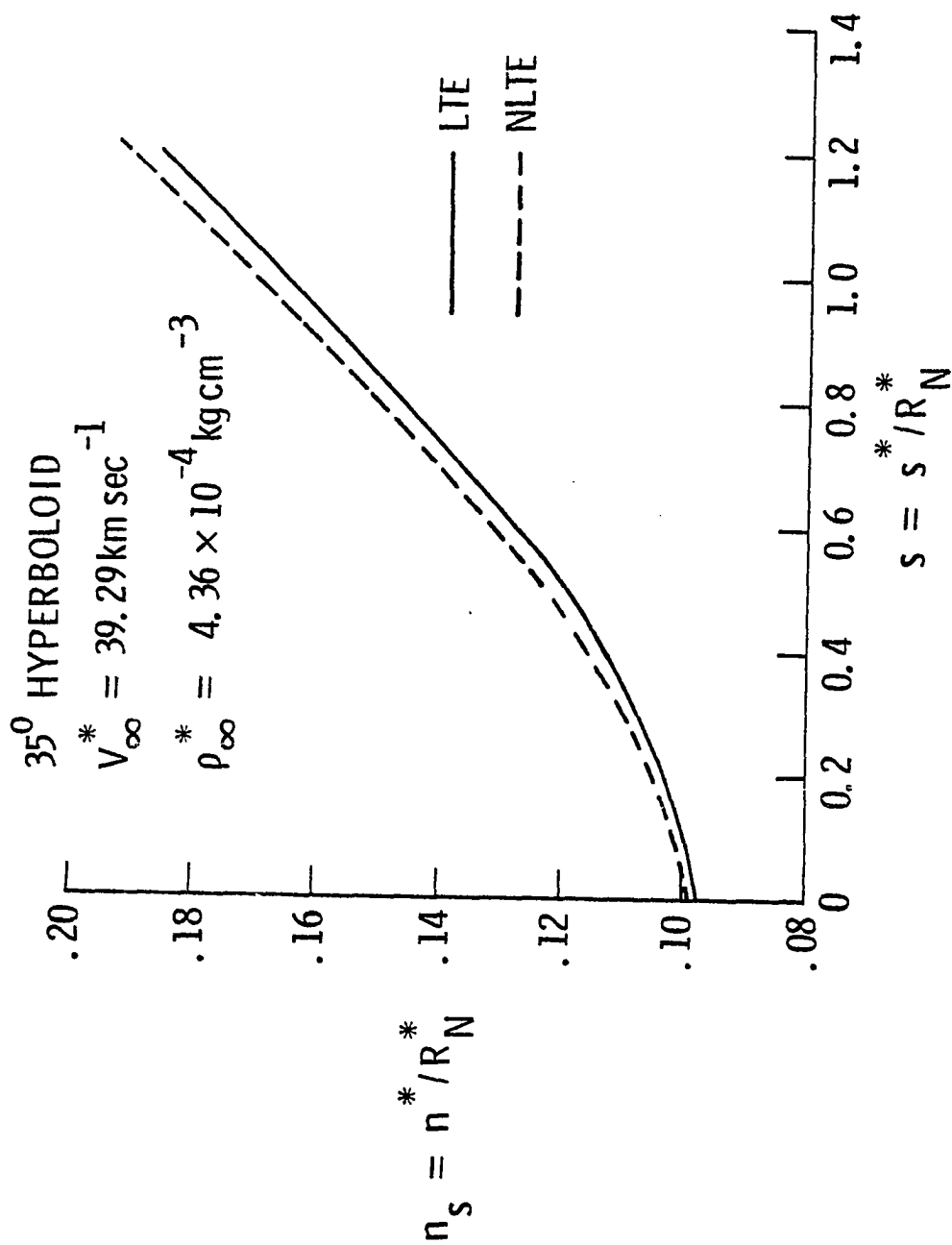


Fig. 33 Shock standoff variation with distance along the body surface.

Variations in the nondimensional surface pressure and heating rate along the forebody of the probe are illustrated in Fig. 34. These quantities are nondimensionalized by their respective stagnation values of $p_{w,0}^* = 6.309 \text{ atm}$, $q_{w,0}^* (\text{LTE}) = 201.849 \text{ MW/m}^2$, and $q_{w,0}^* (\text{NLTE}) = 208.927 \text{ MW/m}^2$. It is seen that NLTE virtually has no influence on the pressure distribution. However, the total heating rate (convective plus radiative) is increased under NLTE conditions. The main contribution to the total surface heating was found to be the radiative heating and this is illustrated in Fig. 35. It is seen that, as a result of the NLTE, the radiative heating rate is increased by about 4 percent at the stagnation point. However, the increase is small at other body locations. The reason for this increase in NLTE radiative heating can be given as follows. Under NLTE conditions, the number of C_2 molecules in the unexcited ground level (that are capable of absorbing the incoming radiation from the shock-layer gases) is less as compared to the LTE values (i.e., the number based on the Boltzmann distributions). This increases the transparency of the ablation layer which, in turn, results in higher heating of the entry body. It is important to point out here that, in the absence of ablative products in the shock-layer gas, the results presented in the previous section indicate that the NLTE reduces the net radiative heating to the entry body. This study indicates that the situation is reversed when contributions of the ablative products are included in the NLTE analysis. This is an important result of the present study. The ablation mass loss rate from the body surface is shown in Fig. 36. As would be expected, the mass loss rate is higher under the NLTE condition (because of the increased heating rates to the body).

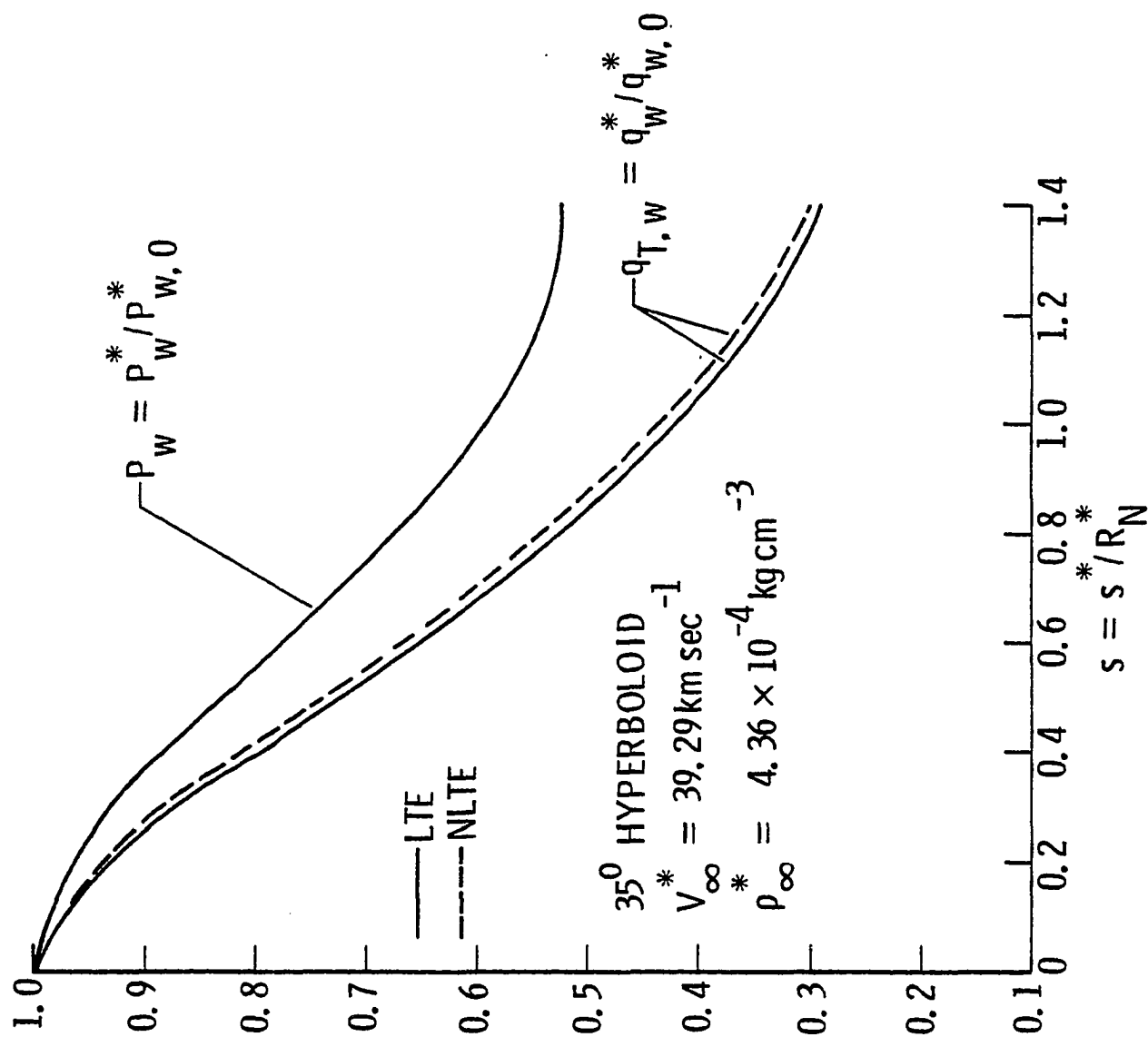


Fig. 34 Pressure and heating rate variations along the body surface.

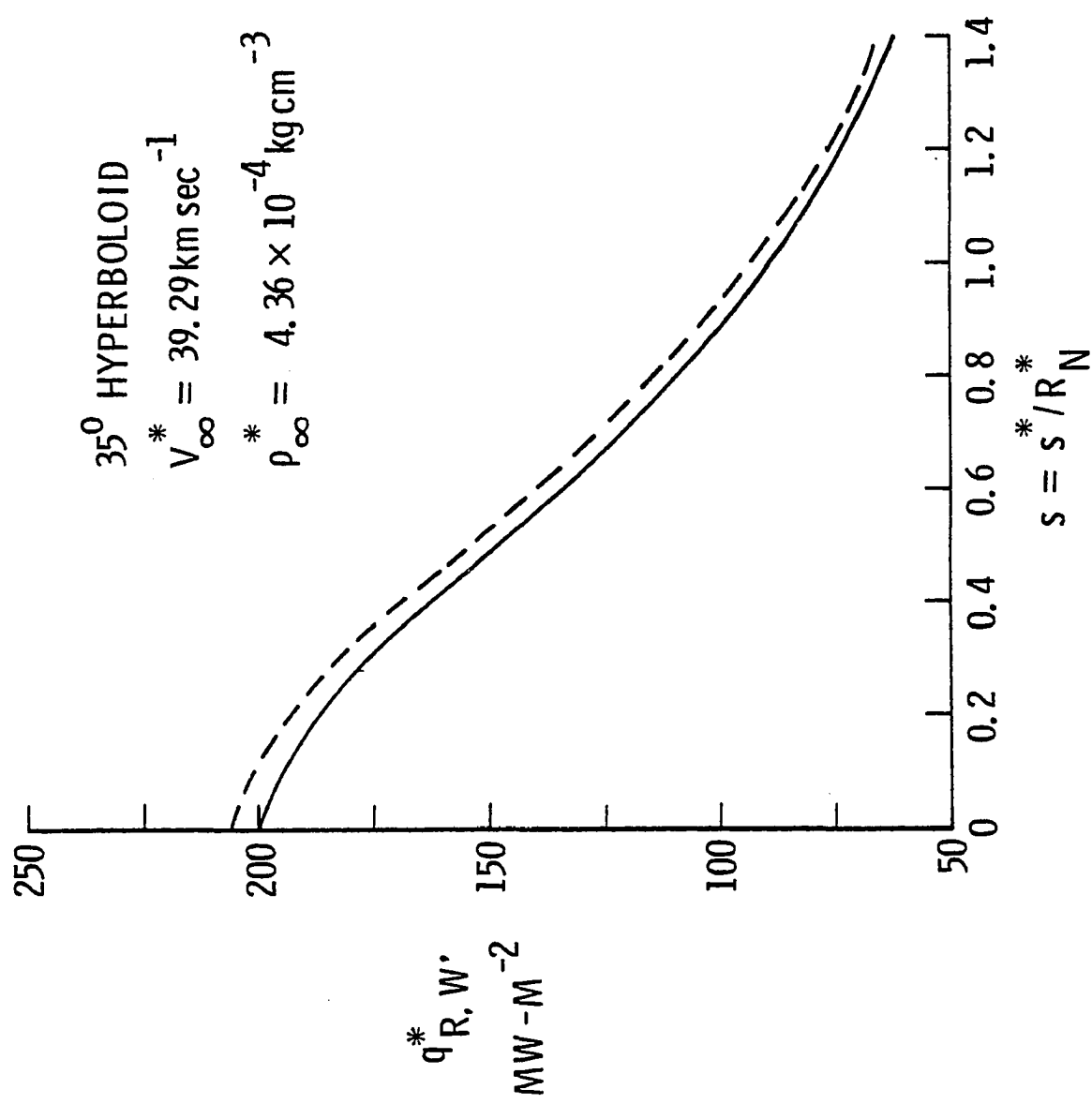


Fig. 35 Variation of heating rate along the body surface.

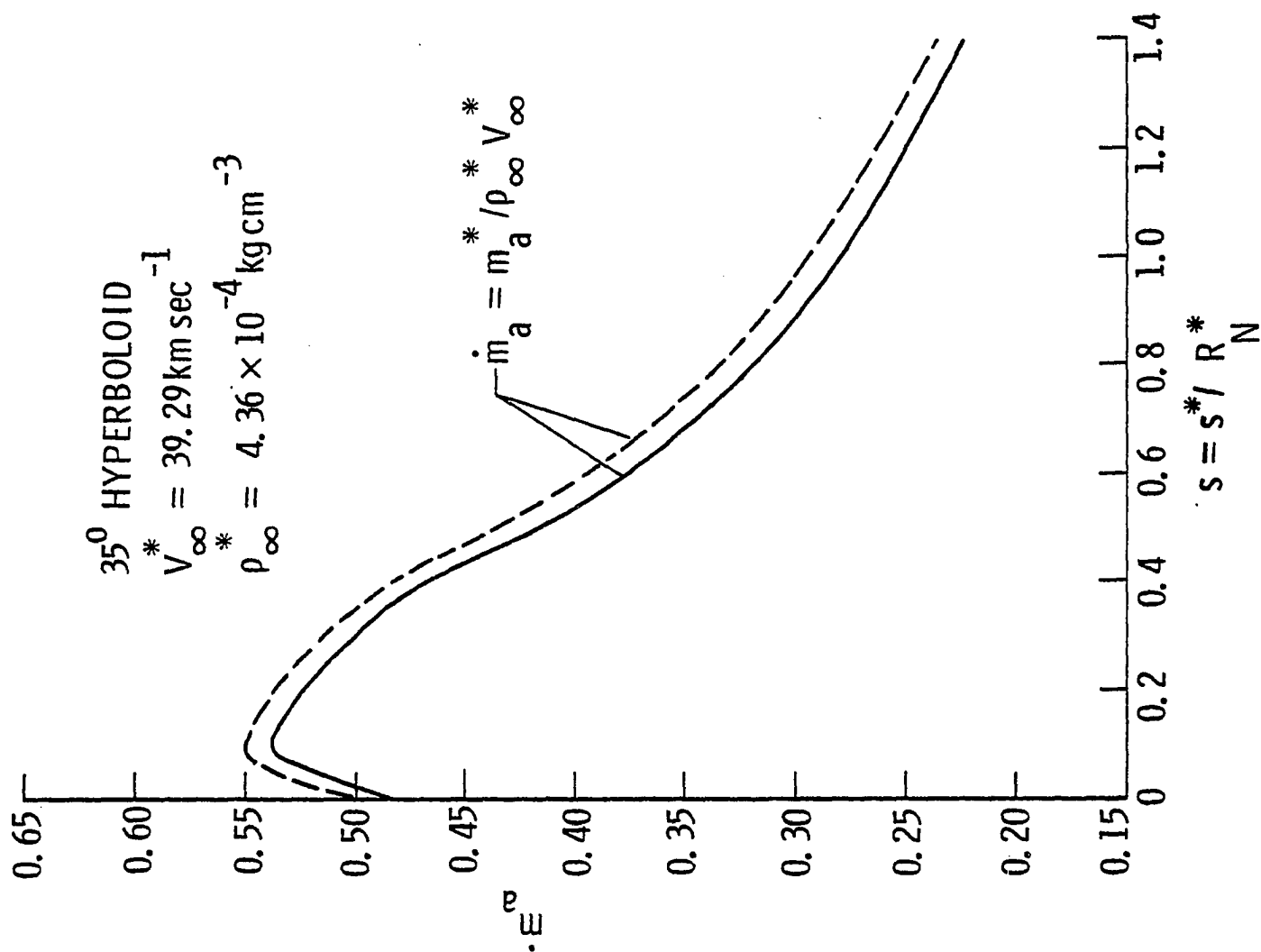


Fig. 36. Ablation mass loss rate along the body surface.

In conclusion, the results presented in this section indicate that the temperature and enthalpy distribution in the shock layer are lower under NLTE conditions. The NLTE increases the density in the shock layer but it has no influence on the pressure variation. The radiative heating to the entry body is increased significantly because of NLTE and this, in turn, results in increased mass loss from the body.

7.4 Effect of Probe Shape Change on the Flow Phenomena

The shock shape and shock-standoff distance are influenced greatly by the shape of the entry body. To study the influence of shape change on flow phenomena around the entry body, it is essential to specify several speculative profiles that will emerge from mass loss and recession of the heat shield just after the peak heating phase of the entry mission. This is important because the main data collection phase of the mission starts after the heating phase. As this stage, it is essential to consider the actual shape of the probe rather than the initial shape in investigating the flow field and aerodynamic stability of the entry body. It is necessary, therefore, to have analytic expressions that are capable of generating such desired shapes. A general relation for the shape change can be given by a quadratic form as

$$y^2 = 2 R_N x - B x^2 \quad (7.1)$$

where B represents the bluntness factor which determines the body shape. For negative values of B , the resulting shapes are a family of hyperbolas. For $B = 1$, circular or spherical shapes are obtained. A family of parabolas is obtained for $B = 0$, and positive values of B give elliptical shapes.

Use of Eq. (7.1) is made in generating different shapes for the entry probe. The initial body shapes considered for this study are a 45-degree sphere cone (i.e., a 45-degree half angle, spherically capped, conical body), a 35-degree hyperboloid (i.e., a hyperbolic forebody shape with an asymptotic angle of $\theta = 35^\circ$), and a 45-degree ellipsoid. The reason for selecting a 35-degree hyperboloid (instead of a 45-degree hyperboloid) is that the mass losses for this and the 45-degree sphere cone and 45-degree ellipsoid are comparable. For all initial shapes, the nose radius considered is 31.12 cm and the base radius is taken to be twice the nose radius. The final shape after the heating phase will depend upon the extent of absorption of incoming radiation by the ablative products. If no radiation blockage is assumed, then it is possible to have severe recession of the forebody as well as of the afterbody. A 25 or 50 percent radiation blockage will result in relatively less severe blunting of the entry probe. It is possible to generate these speculative profiles with help of Eq. (7.1).

The numerical procedure employed by Sutton et al. (Ref. 26) for inviscid radiating flow is basically used in this study also. For the initial profile, the x and y coordinates, the distance along the body, and the radius of curvature are specified at 14 selected stations along the body. For the changed profiles, the distance along the body, the radius of curvature, and the body angle are calculated at each station by using a subroutine with x and y coordinates as inputs. A three-point central differencing scheme is used for calculation of the s location, and a two-point backward differencing scheme is used for calculation of the curvature.

The three initial body shapes and the corresponding body profiles that emerge if the influence of shape change is considered are shown in Figs. 37a to 37c. Figure 37a shows the forebody configurations of the 45-degree sphere cone in which profile 1 represents the initial shape and profile 2 is the corresponding blunted profile. Profile 2 represents a case where the entry body has experienced a severe blunting near the stagnation region as compared to the downstream region. Specifically, this represents a shape where the initial body has undergone a severe mass loss near the nose after absorbing about 50 percent of the incoming radiation. Profiles 3 and 4 in Fig. 37a represent two arbitrary blunted shapes for which the mass loss is assumed to be uniform all along the body. For all the forebody profiles shown in Fig. 37a, the afterbody shape is a 45-degree half-angle cone.

Different configurations for the 35-degree hyperboloid are shown in Fig. 37b. In this case also, the severely blunted profile is represented by the curve 2. This corresponds to the case of severe stagnation region mass loss with assumed radiation blockage of about 50 percent. Profile 3 in Fig. 37b represents the shape for approximately 40 percent radiation blockage with uniform mass loss along the entire body. Different configurations for the 45-degree ellipsoid are shown in Fig. 37c, and they correspond to exactly the same conditions as for the 35-degree hyperboloid.

The condition of LTE for the radiative transport was assumed while obtaining the results using different probe configurations. Since NLTE is a condition of the absorbing/emitting gases, it is assumed that the shape change will not influence the NLTE phenomena. The results have been obtained for different entry conditions and they are presented here

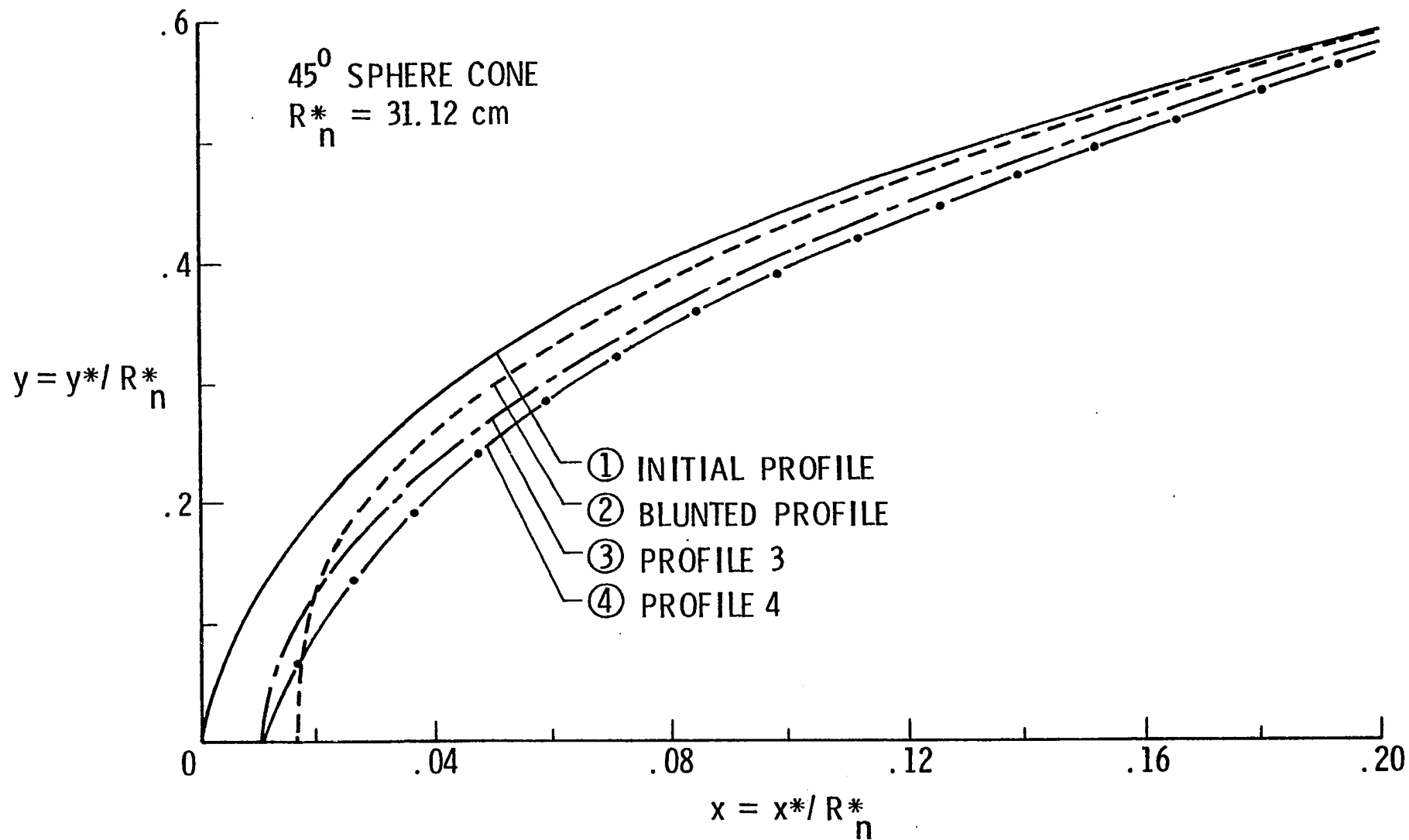


Fig. 37a Forebody configurations for 45-degree sphere cone.

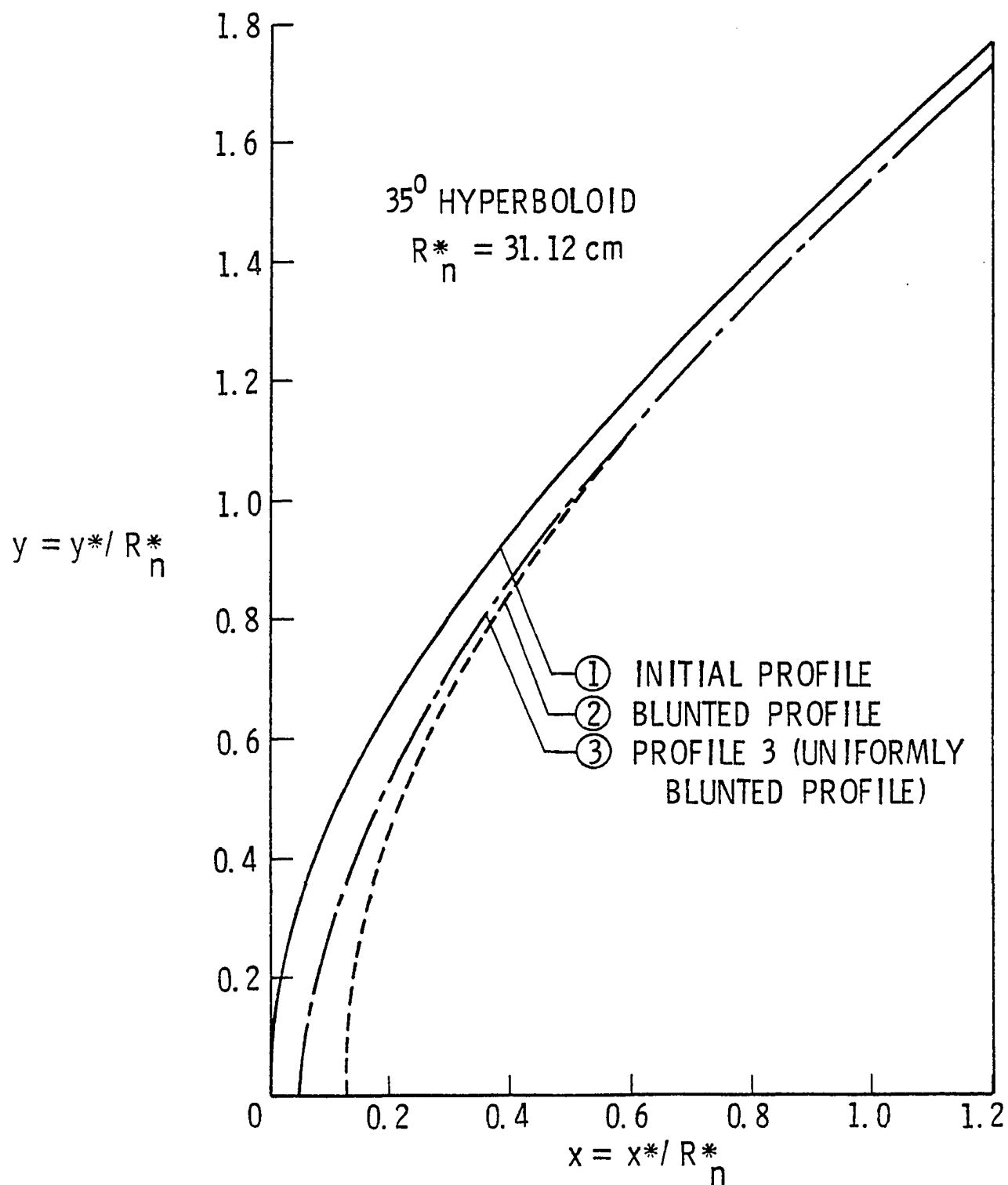


Fig. 37b Configuration for 35-degree hyperboloid.

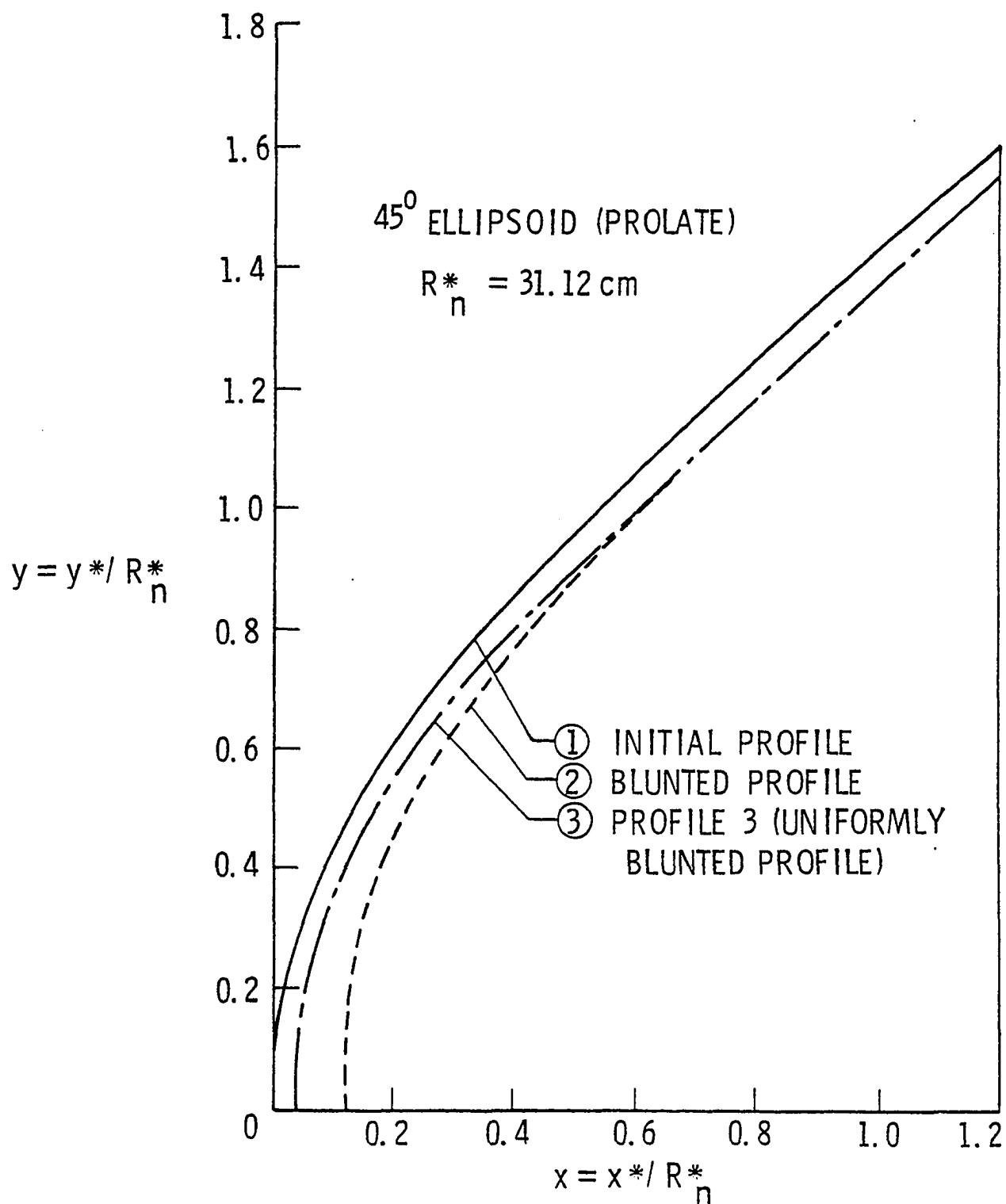


Fig. 37c Configuration for 45-degree ellipsoid.

first for the 45-degree sphere cone and then for the 35-degree hyperboloid. Finally, the peak heating results for the 45-degree sphere cone and 35-degree hyperboloid are compared with peak heating results of the 45-degree ellipsoid.

7.4.1 Results for 45-Degree Sphere Cone

Different results obtained for the 45-degree sphere cone are illustrated in Figs. 38 to 45. The shock standoff variation with distance along the body surface is shown in Figs. 38 and 39. For peak heating conditions (i.e., for $Z = 116$ km), results obtained for the four profiles indicated in Fig. 37a are illustrated in Fig. 38. Results obtained for the initial and blunted profiles are compared in Fig. 39. for the three entry conditions considered. The results indicate that blunting of the nose region increases the shock-layer thickness not only near the stagnation region but all along the body, although there is no significant change in the body shape near the flank region. It is evident from Fig. 38 that profiles 3 and 4 do not influence the shock-standoff distance appreciably. This is because the uniform mass loss tends to preserve the original configuration of the entry body. As would be expected, the shock-standoff distance, in general, increases with decreasing altitude, and near the stagnation region the influence of nose blunting is greater at lower altitudes.

Variation of the shock temperature (i.e., the temperature just behind the shock) with distance along the body surface is shown in Fig. 40 for the three entry conditions considered. For these conditions, the shock temperature, in general, is found to be for higher entry altitudes. The effect of blunting is seen to increase the shock

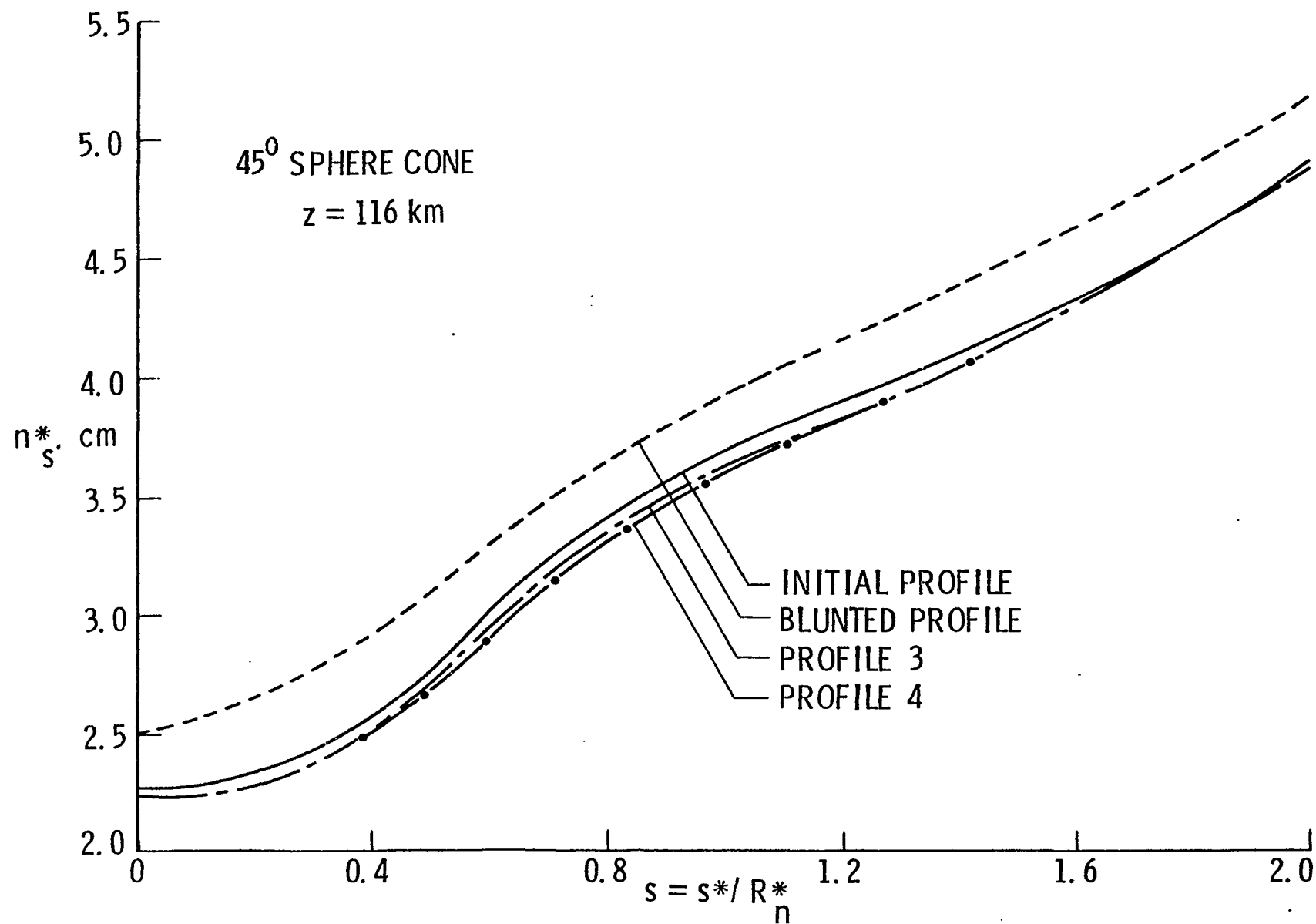


Fig. 38 Shock-standoff variation for 45-degree sphere cone, $z = 116$ km.

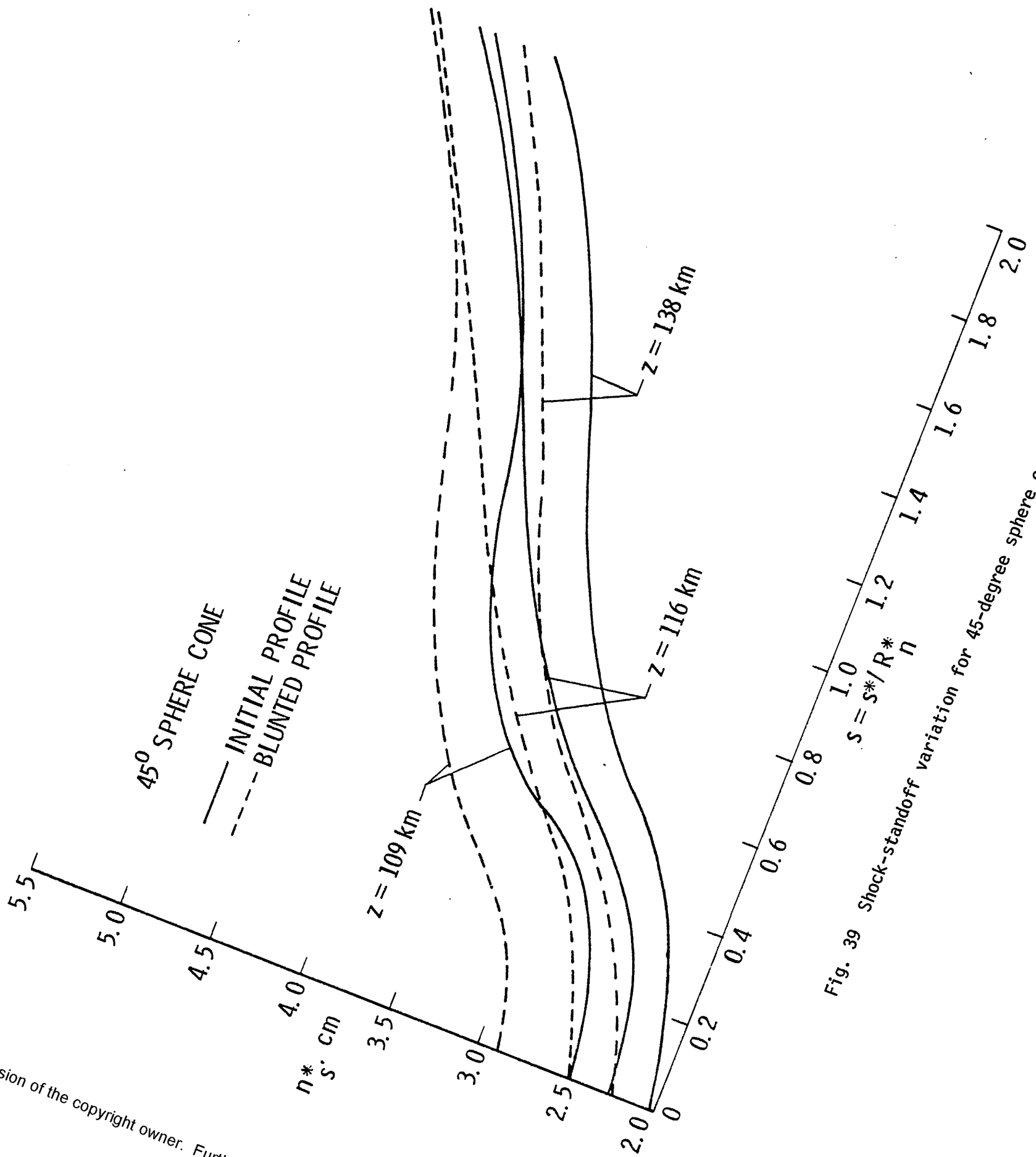


Fig. 39 Shock-standoff variation for 45-degree sphere cone.

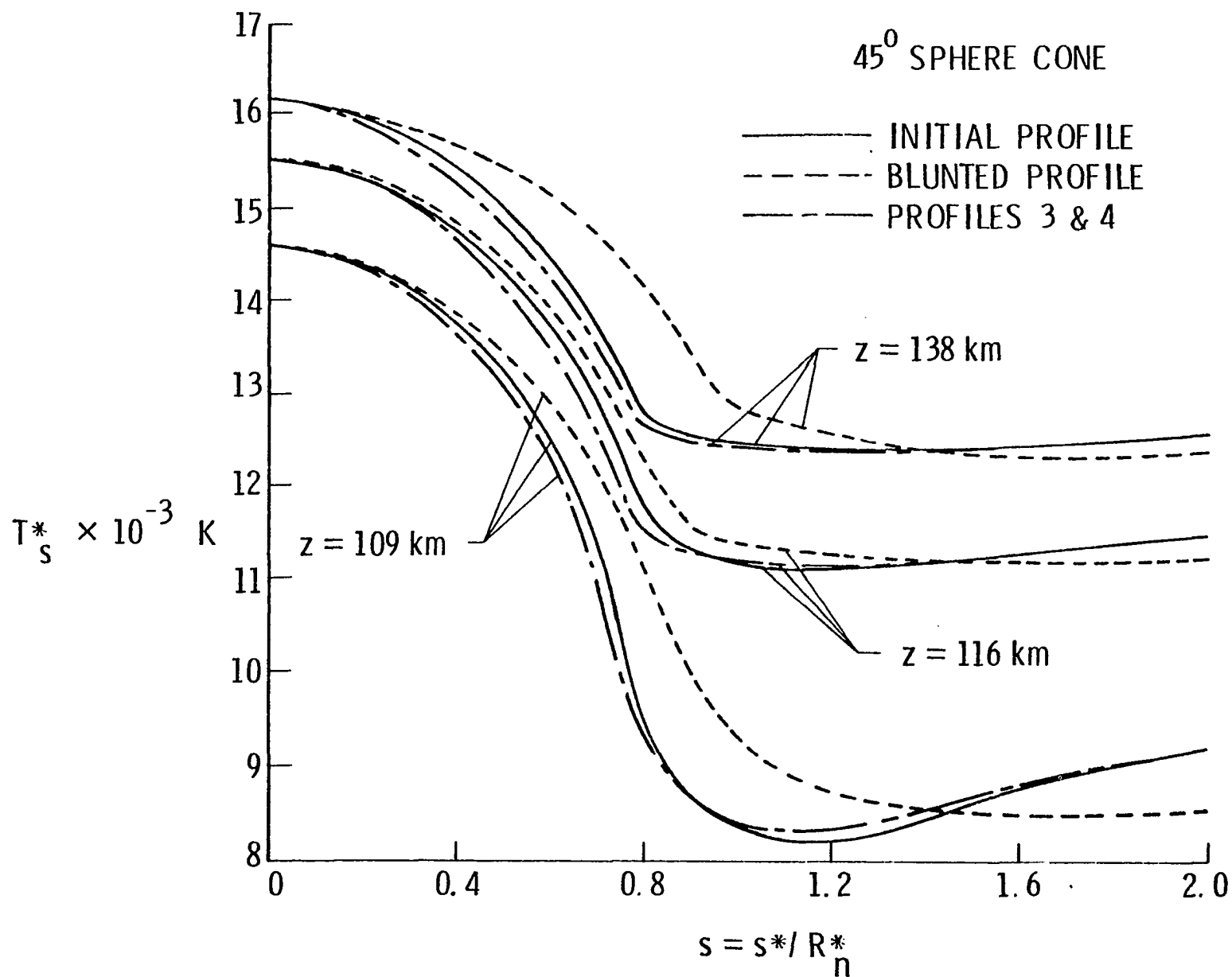


Fig. 40 Variation of temperature just behind the shock for 45-degree sphere cone.

temperature along most of the downstream region of the probe. For $Z = 116$ km, a maximum difference of 5.6 percent is found at the tangency point (where the forebody and afterbody coincide asymptotically). The effect of blunting is seen to have relatively higher influence on the shock temperature for the other two entry conditions. Results of moderate shape change (with uniform mass loss), as shown by curves 3 and 4, indicate negligible influence on the shock temperature. Variation in density just behind the shock along the body surface is shown in Fig. 41 for 2 entry conditions, $Z = 116$ km and 138 km. In general, lower shock densities are associated with higher entry altitudes. This is because the free stream densities are lower at higher altitudes. The shock-density variation is relatively higher for the blunted profile, and a significant increase is noted from the stagnation point to the tangency point. However, virtually no difference is seen after the location $s = 1$. For $Z = 116$ km, a maximum difference of 5.6 percent is noted between the initial and blunted profiles at location $s = 0.8$. This difference is even smaller (4.5 percent) for results at $Z = 138$ km. Results of profiles 3 and 4 are in general agreement with the results of the initial profiles; a maximum difference of 1.25 percent is noted at $s = 0.8$ for $Z = 116$ km.

Variations in density and v -velocity across the shock layer are shown in Figs. 42 and 43 respectively. Figure 42 shows the density variation for two body locations ($s = 0$ and 1.4) and entry conditions ($Z = 116$ km and 138 km). It is seen that along the stagnation line the density is not influenced by the shape change. However, significant differences in results of the initial and blunted profiles are noted for the downstream location of $s = 1.4$. The density

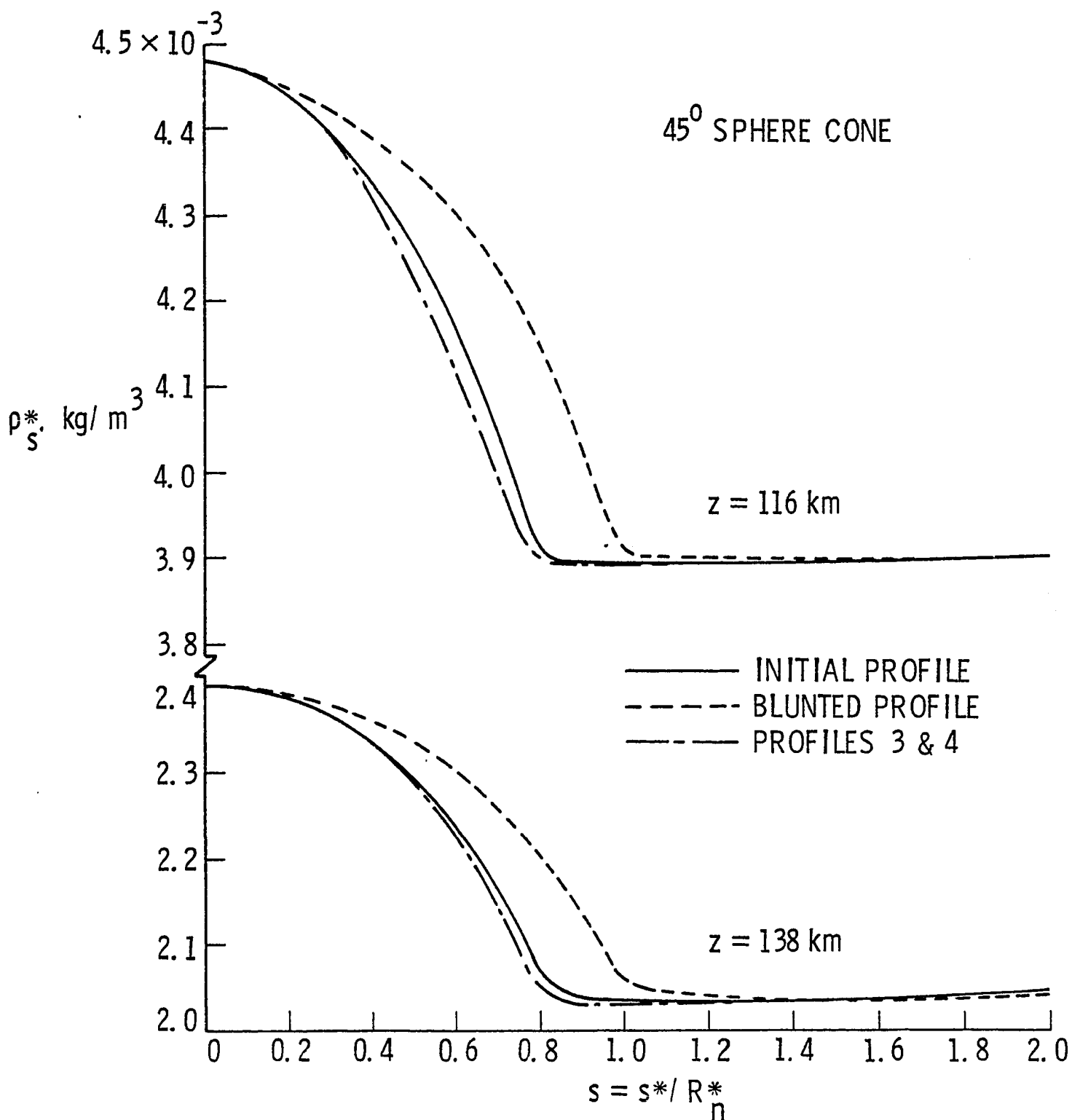


Fig. 41 Variation of density just behind the shock for 45-degree sphere cone.

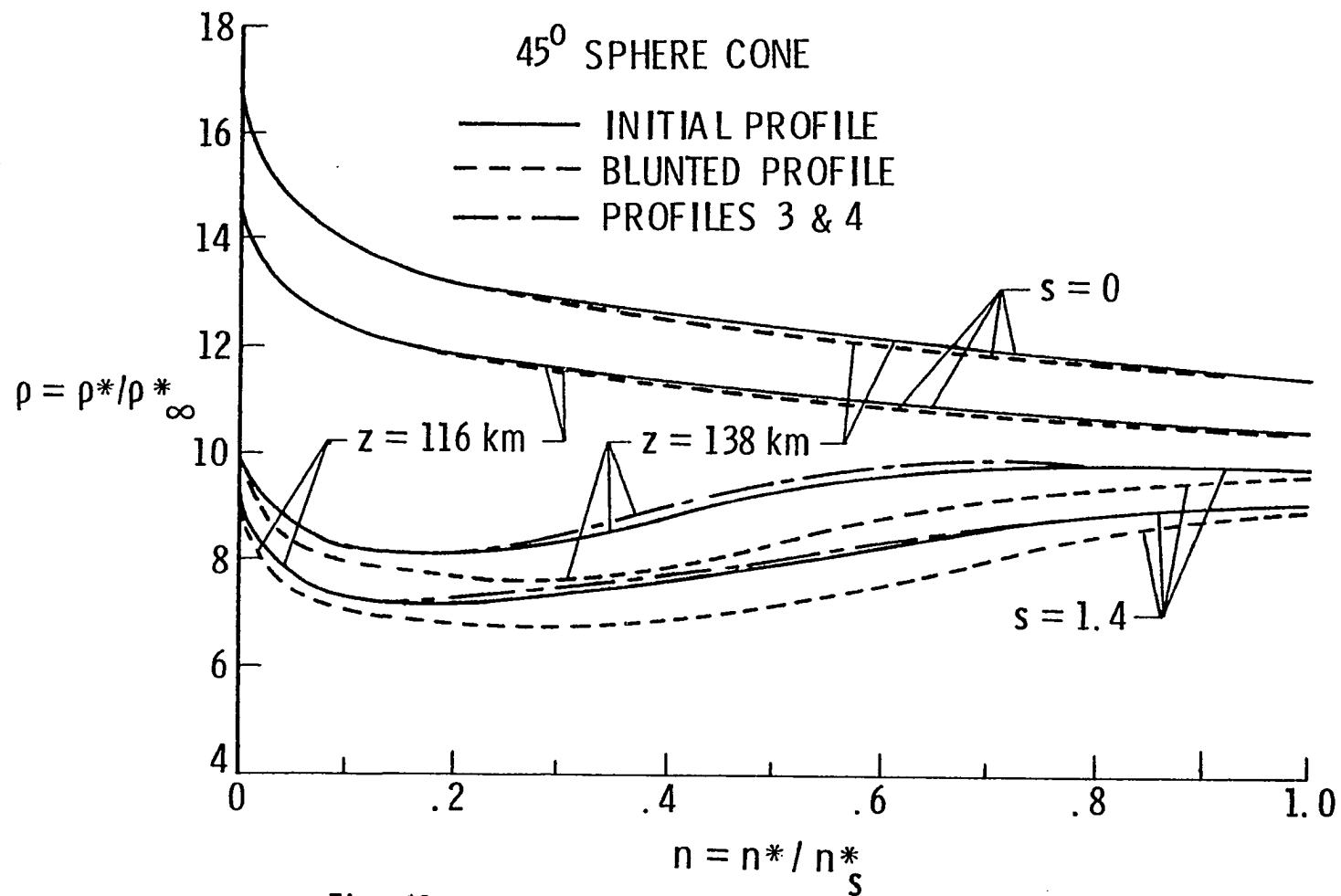


Fig. 42. Variation of density in the shock layer for 2 body location ($s = 0$ and 1.4), 45 -degree sphere cone.

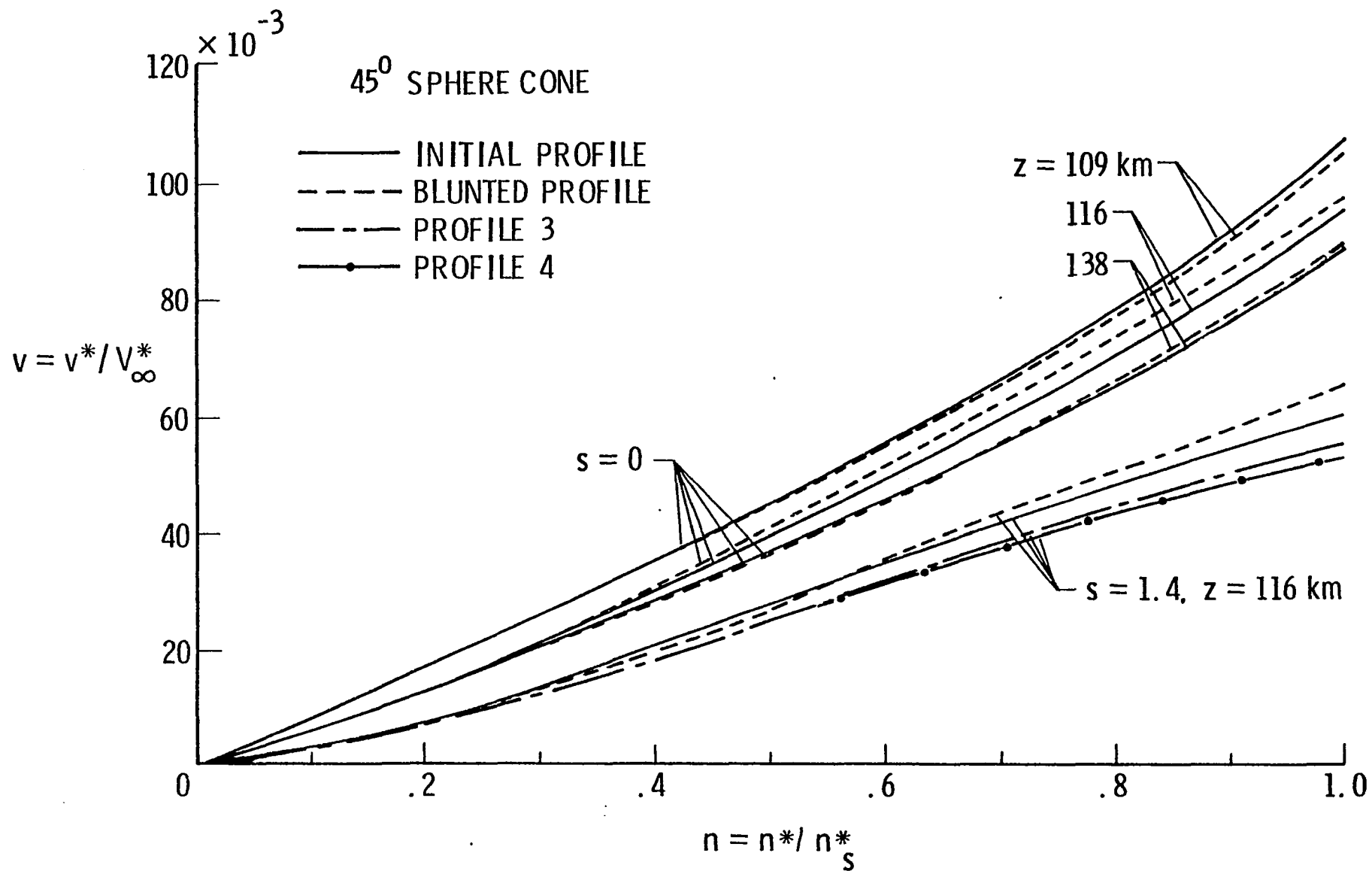


Fig. 43a Variation of v-velocity component in the shock-layer along the stagnation streamline and for $s = 1.4$ and $Z = 116 \text{ km}$.

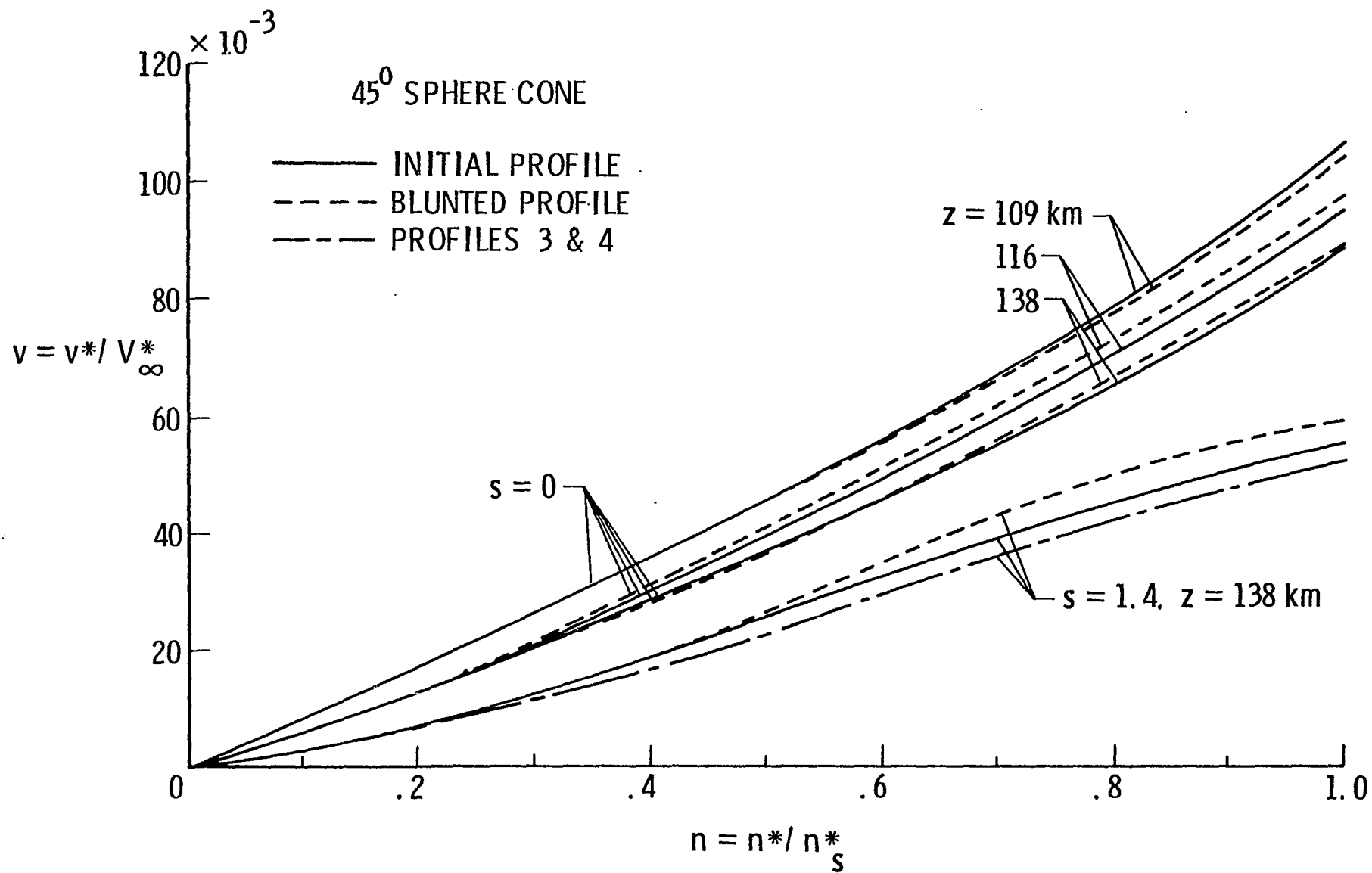


Fig. 43b Variation of v-velocity component in the shock layer along the stagnation streamline and for $s = 1.4$ and $Z = 138 \text{ km}$.

values are lower for the blunted profile because the temperatures are relatively higher. Uniform profile changes do not alter the density values appreciably. Figures 43a and 43b show that shape change does not influence the radial component of velocity significantly along the stagnation streamline. However, blunting is seen to influence the velocity toward downstream locations.

In the shock layer, variation in pressure is relatively small as compared to variations in temperature and density. The variation of pressure along the wall is shown in Fig. 44 for the four profiles and three entry conditions. As would be expected, pressure distribution is relatively higher for lower altitudes, and the maximum pressure occurs at the stagnation point. Results of profiles with uniform mass loss are not significantly different from the results of the initial profile. Blunting of the entry body is seen to increase the wall pressure significantly different from the results of the initial profile. Blunting of the entry body is seen to increase the wall pressure significantly, the increase being maximum closer to the tangency point. Blunting does not seem to affect the stagnation region and downstream pressure distribution appreciably. However, it is possible for the blunted probe to experience relatively higher total drag.

The radiative heating results are illustrated in Figs. 45a and 45b. In each case, the heating rate is seen to be significantly higher for the blunted profile all along the body. This, however, is expected because the shock temperature and shock-standoff distance are relatively higher for the blunted profile (see Figs. 39 and 40). The maximum stagnation point heating occurs, of course, at $Z = 116$ km. For this case, the blunted profile heating rate is about 9 percent higher than the

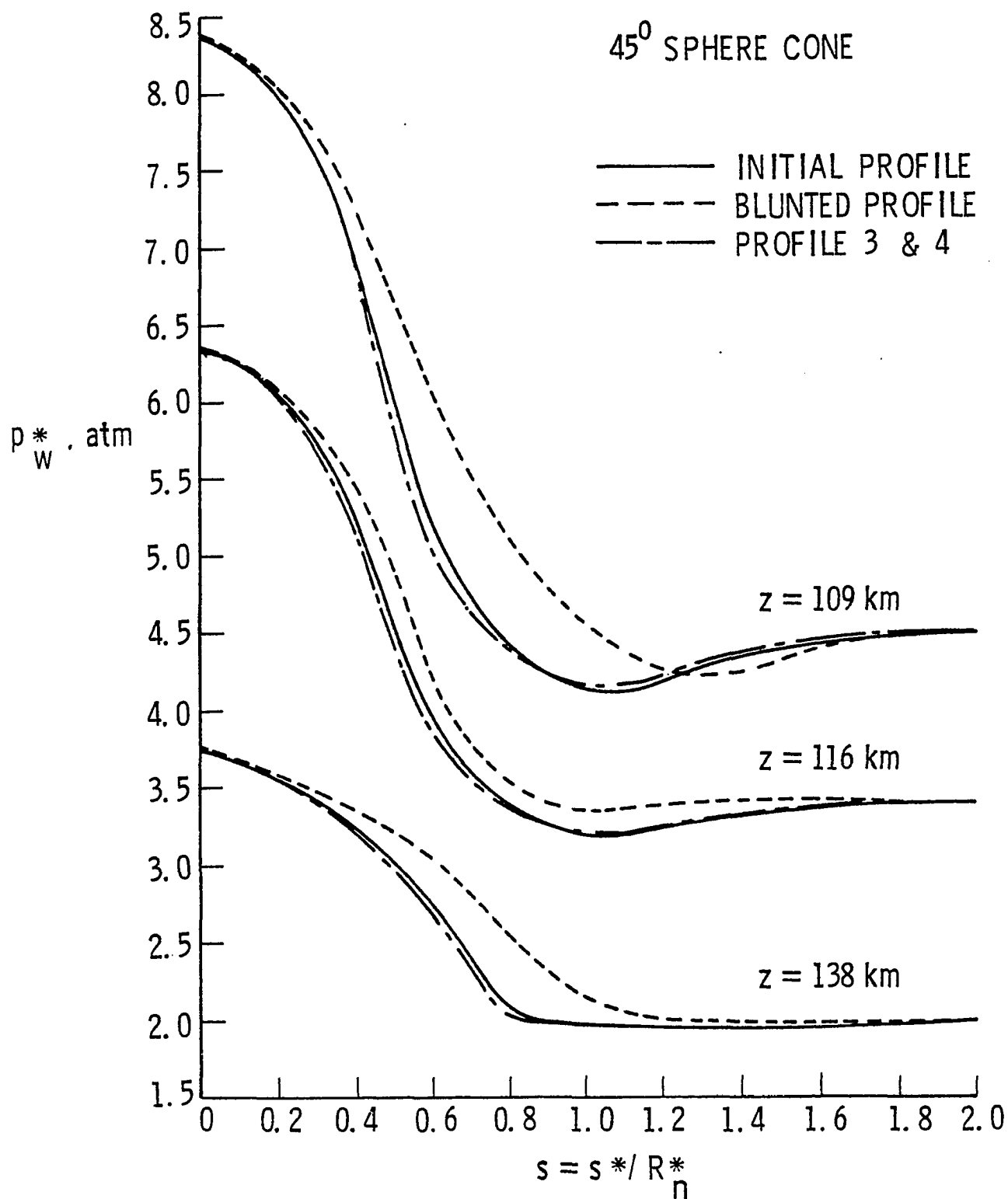


Fig. 44 Surface pressure variation for 45-degree sphere cone.

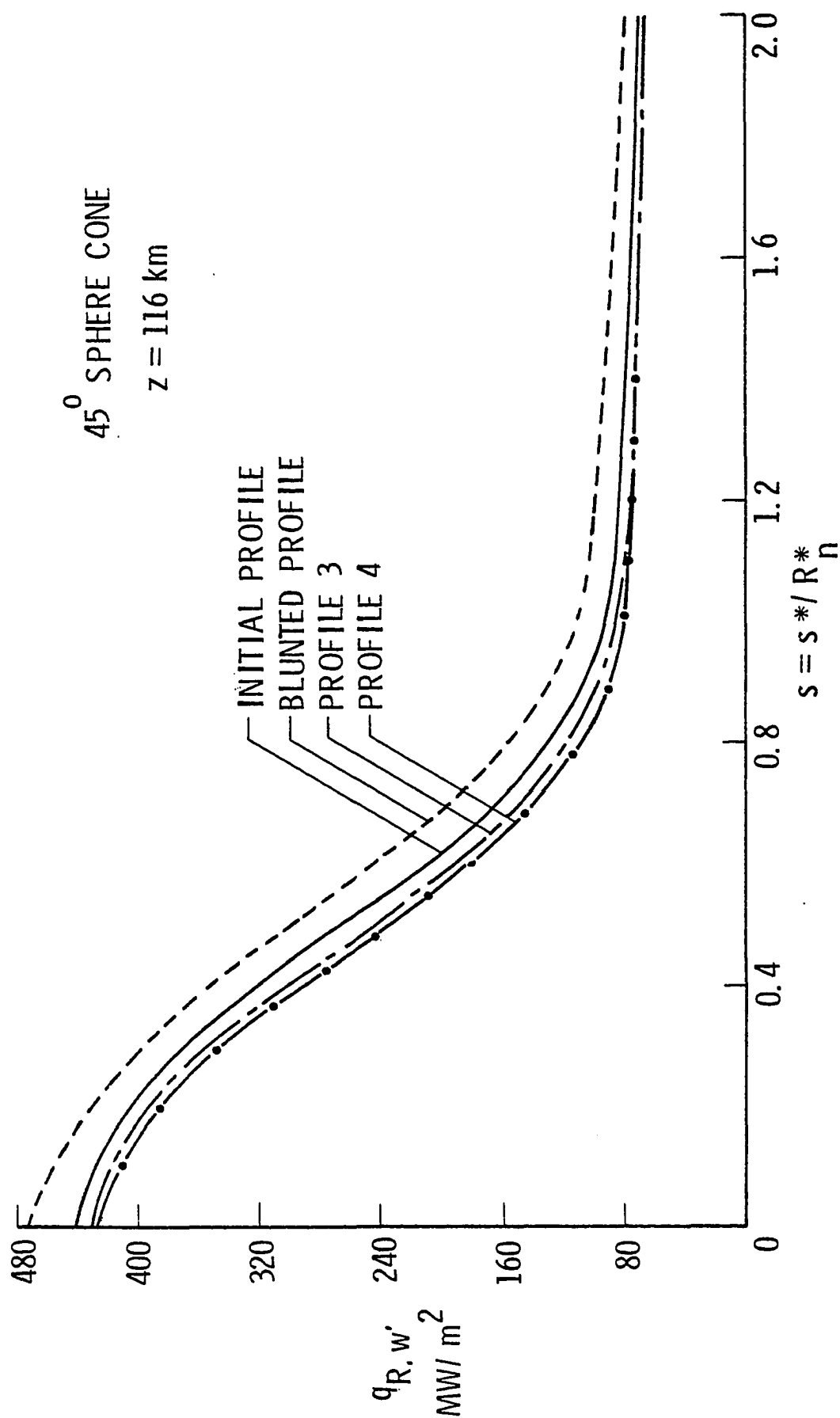


Fig. 45a Radiative heating rates for 45-degree sphere cone, $Z = 116 \text{ km}$.

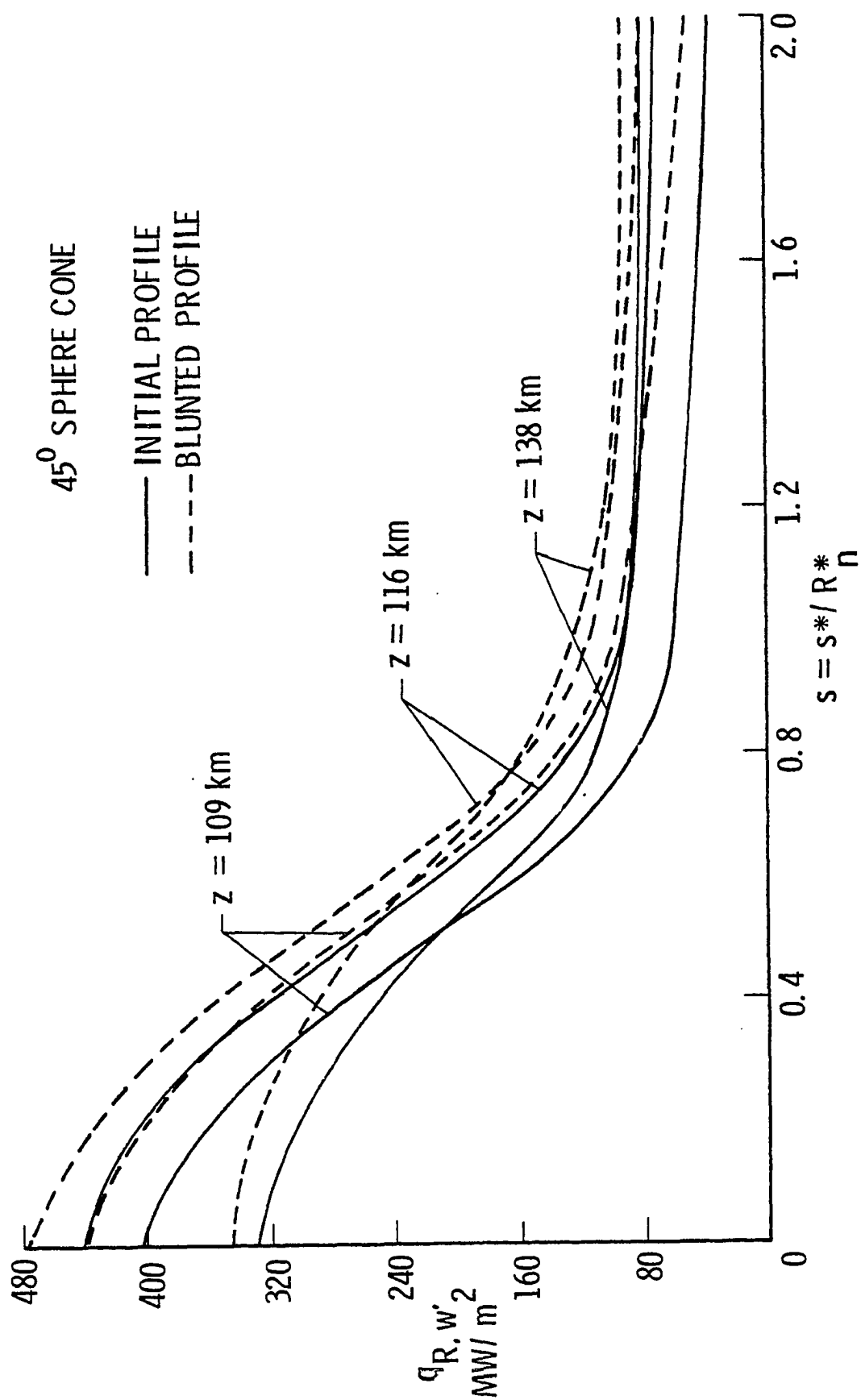


Fig. 45b Radiative heating rates for 45-degree sphere cone.

initial profile heating. Figure 45a shows that heating rates for profiles 3 and 4 are lower than those of the initial profile. A difference of 4.9 percent between initial profile and profile 3, and of 5.3 percent between initial profile and profile 4, is noticed at the stagnation point. Results presented in Fig. 45b indicate that the stagnation-region heating is comparatively higher for $Z = 109$ km than for $Z = 138$ km. The difference between stagnation-point heating rates for the blunted and initial profiles is 10 percent for $Z = 109$ km and 6 percent for $Z = 138$ km. The results clearly indicate that the shape change can have significant influence on heating of the afterbody of the entry probe.

7.4.2 Results for 35-Degree Hyperboloid

Some important results obtained for the 35-degree hyperboloid profiles (see Fig. 37b) are presented in Figs. 46 to 52. As expected, the hyperboloid results show a smoother trend than the sphere cone results. The shock standoff variation with distance along the body surface is illustrated in Fig. 46 for the three entry conditions considered. The results indicate that shape change increases the shock standoff distance all along the body. The increase is greater for the blunted profile, and a maximum increase of 8.5 percent is noted for $Z = 109$ km at $s = 0$. The results of profile 3 show an increase of only about 3 percent for $Z = 109$ km at $s = 0$. Variation of the shock temperature is illustrated in Fig. 47. The results show that the shape change has only a slight influence on the temperature between locations $s = 0.2$ and 1.2 , and its effects are negligible further downstream. Variation in the shock density for the initial and blunted profiles is shown in Fig. 48 for entry conditions at $Z = 116$ km and 138 km. The

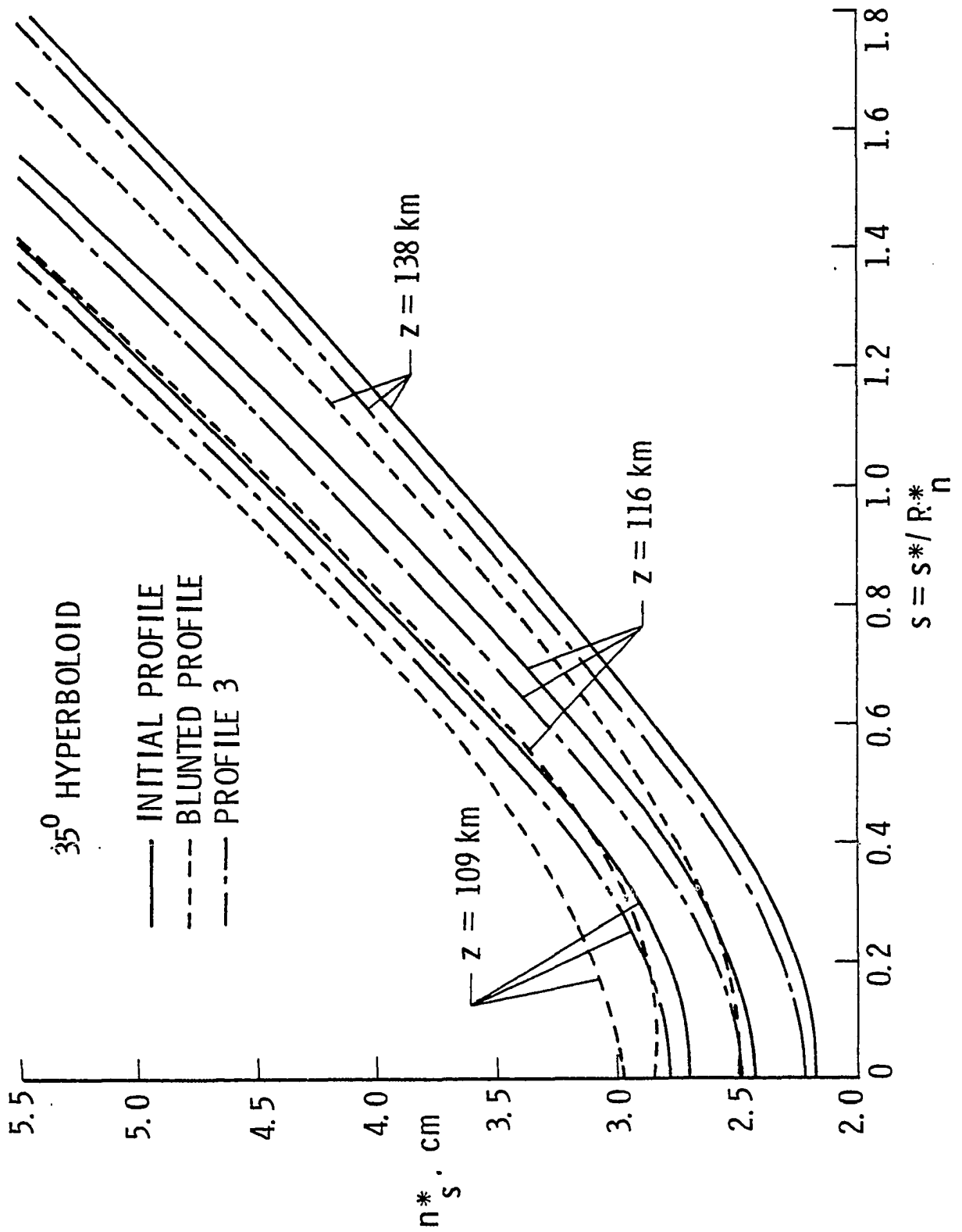


Fig. 46 Shock-standoff variation for 35-degree hyperboloid.

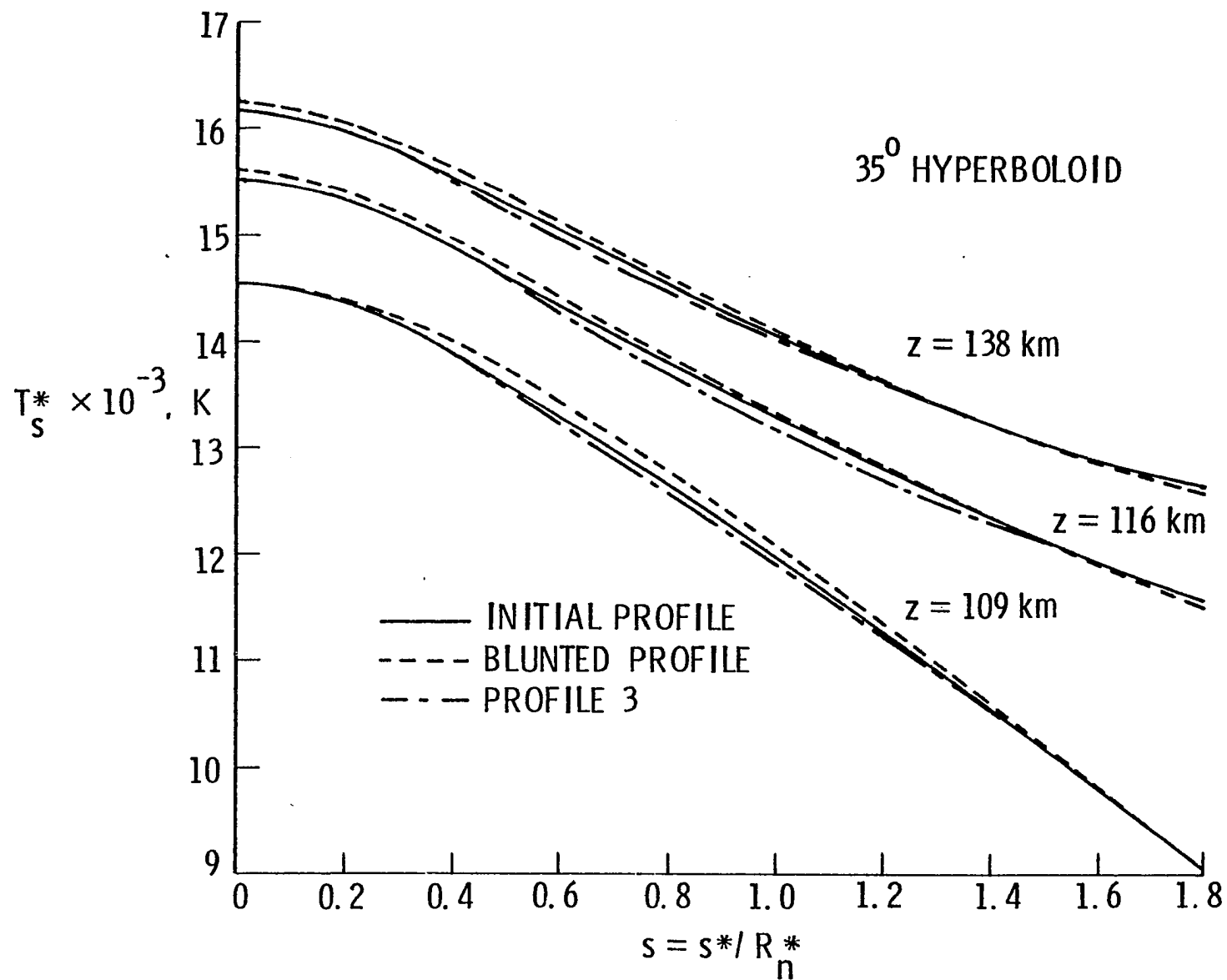


Fig. 47 Variation of temperature just behind the shock for 35-degree hyperboloid.

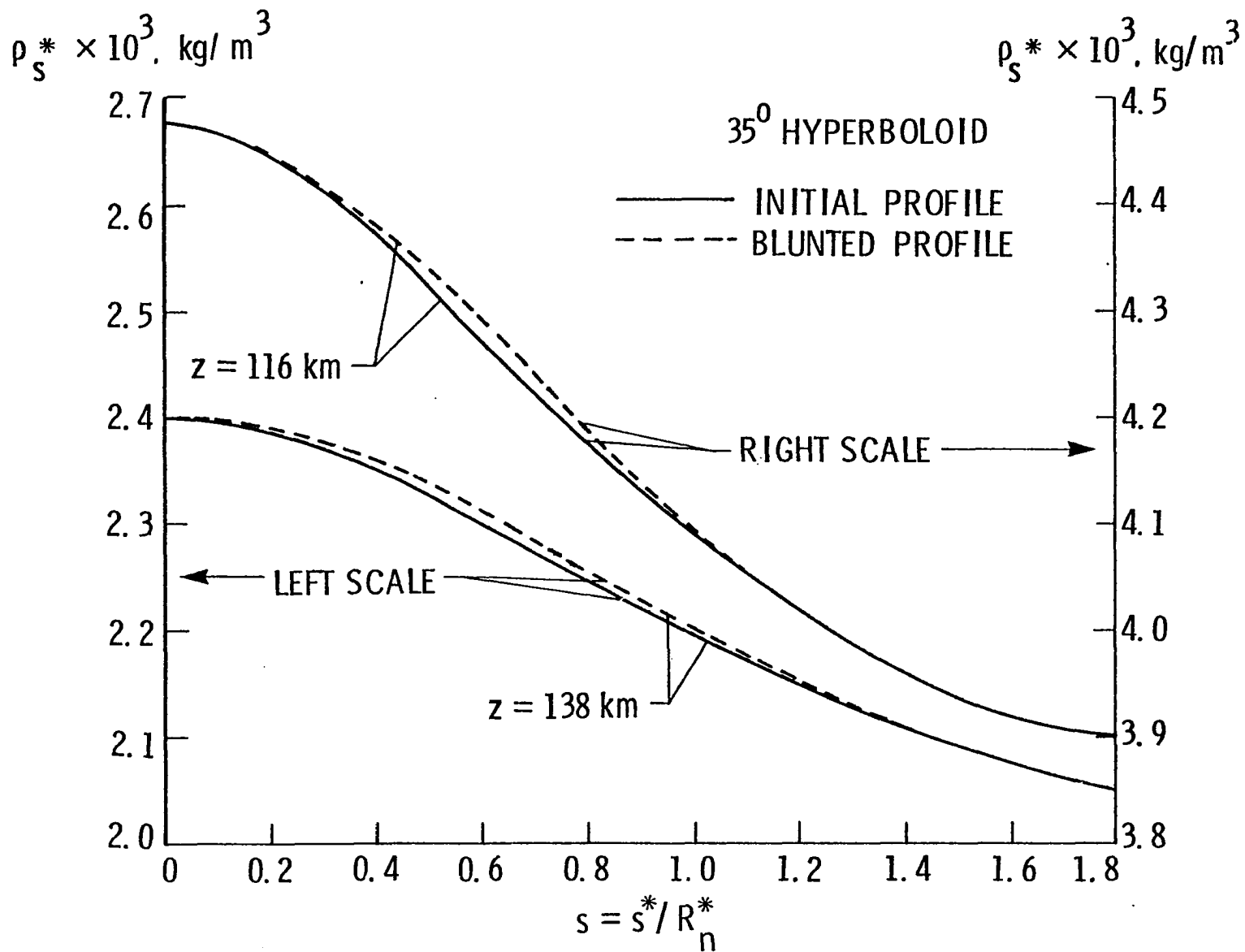


Fig. 48 Variation of density just behind the shock for 35-degree hyperboloid.

results indicate only slight influence of the shape change on the density variation.

The changes in velocity, density, temperature, and pressure across the shock layer of a hyperboloid essentially follow the same general pattern as for the sphere cone, but the effects of shape change are not as pronounced. Variations in density and v-velocity across the shock layer are shown in Figs. 49 and 50, respectively. Figure 49 shows the density variation for two body locations ($s = 0$ and 1.5) and entry conditions ($Z = 116$ km and 138 km). It is seen that along the stagnation line the density is not influenced by the shape change. However, small differences in results of the initial and blunted profiles are noted for the downstream location of $s = 1.5$. Uniform profile changes alter the density only slightly in the regions closer to the body. Figure 50 shows that along the stagnation streamline the shape change does not have any influence on the radial component of velocity; only slight changes are noted for $Z = 138$ km and at $s = 1.5$.

The pressure distribution along the wall is illustrated in Fig. 51 for the three entry conditions. The results indicate that blunting of the body slightly increases the wall pressure for conditions $Z = 116$ km and 138 km. Results of the initial profile and the profile with uniform mass loss were so close that the difference could not be shown in Fig. 51.

The results of radiative heating are presented in Fig. 52. These results follow the general trend of the sphere cone results. The differences in stagnation-point heating rates for the initial and blunted profiles are found to be 4.9, 4.1, and 3.2 percent for $Z = 109$ km, 116 km, and 138 km, respectively. Results of the profile with

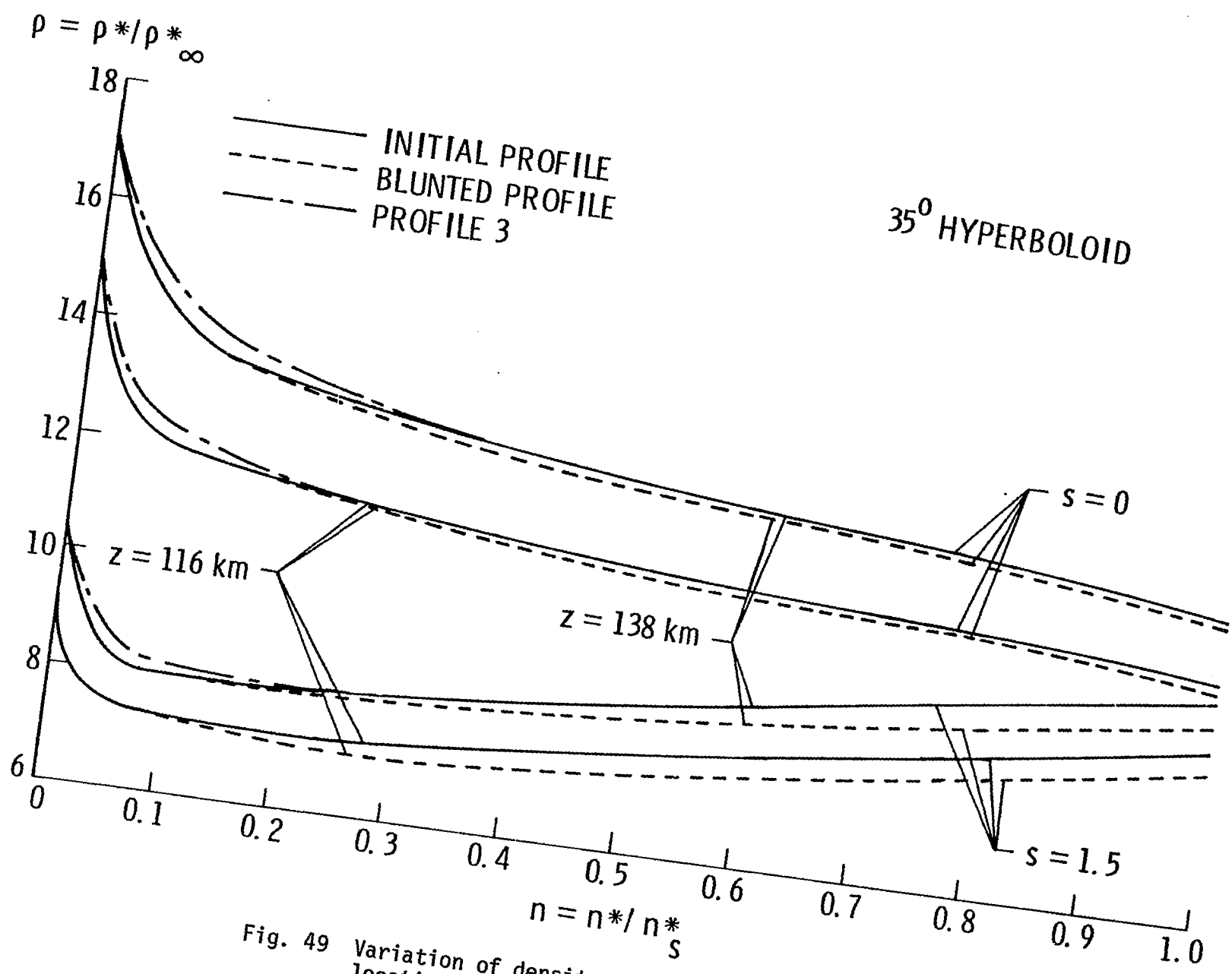


Fig. 49 Variation of density in the shock layer for body location ($s = 0$ and 1.5), 35-degree hyperboloid.

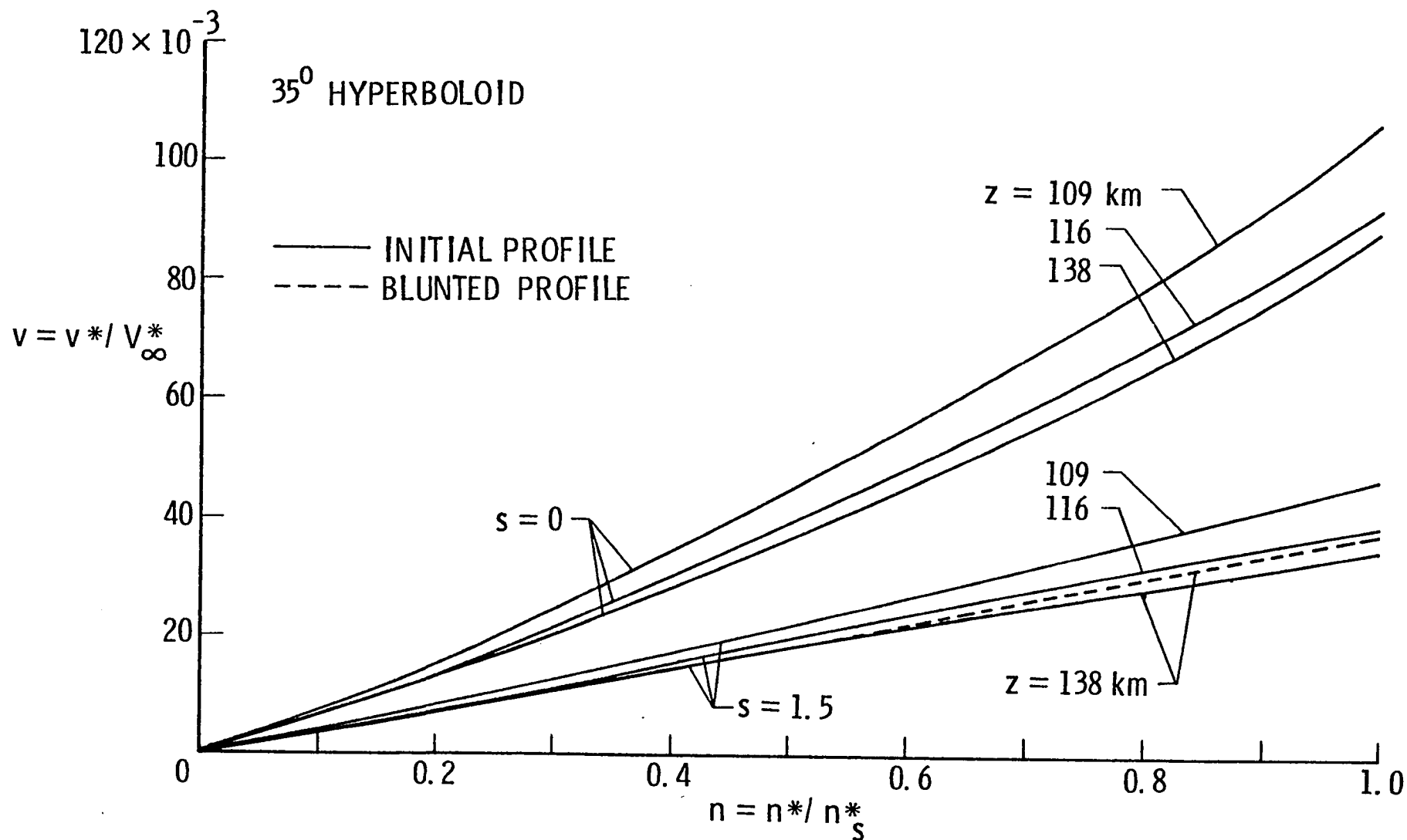


Fig. 50 Variation of v -velocity component in the shock layer for 2 body locations ($s = 0$ and 1.5), 35-degree hyperboloid.

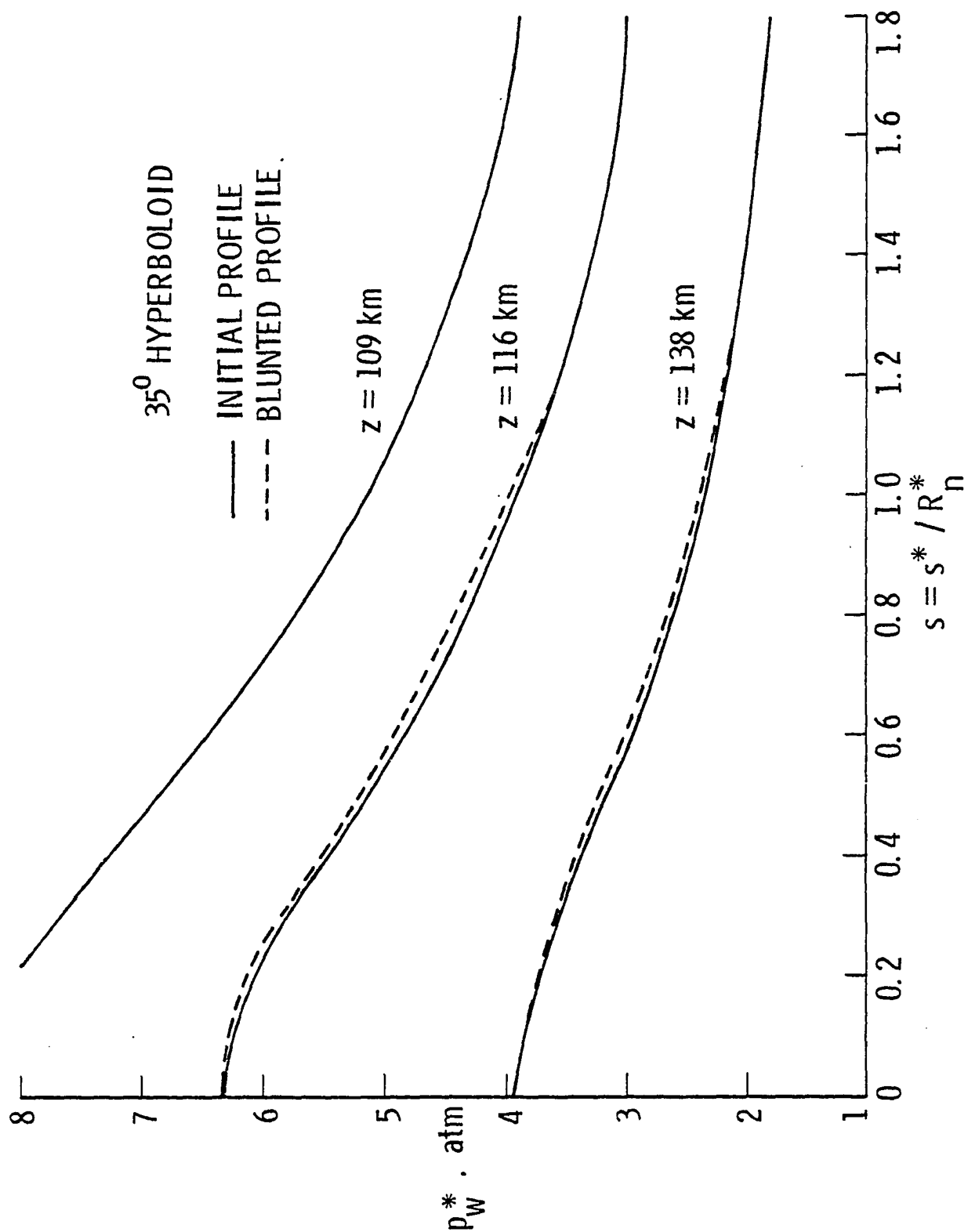


Fig. 51 Surface pressure variation for 35-degree hyperboloid.

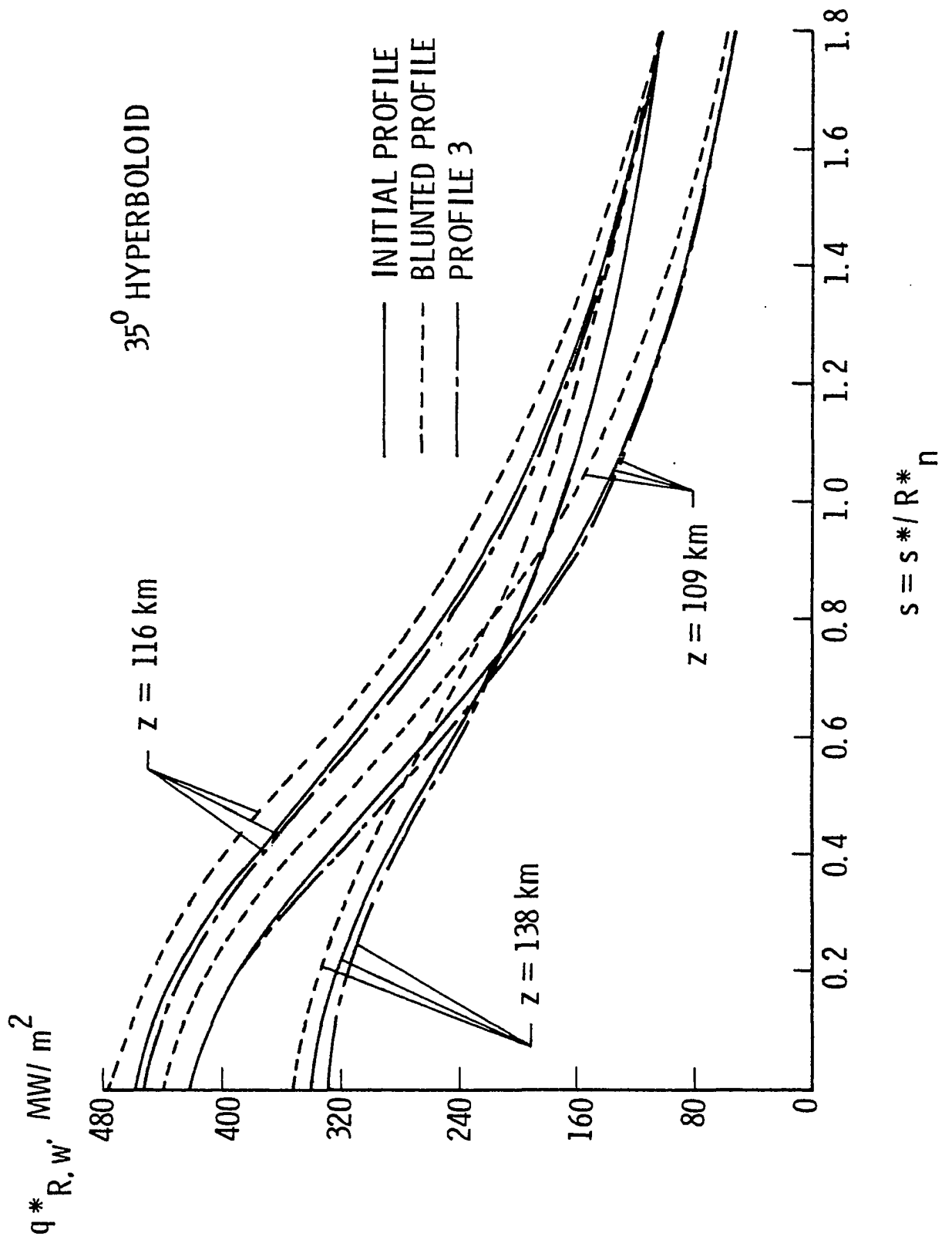


Fig. 52 Radiative heating rates for 35-degree hyperboloid.

uniform mass loss are not seen to be significantly different from the results of the initial profile.

7.4.3 Comparison of Peak Heating Results

Peak heating results for the 45-degree sphere cone, 35-degree hyperboloid, and 45-degree ellipsoid are compared in Figs. 53 to 57. Results for the 45-degree ellipsoid are seen to follow the same general trend as results for the 45-degree sphere cone; and, in comparison, results for the 35-degree hyperboloid are seen to exhibit a relatively smoother trend. In the stagnation region, all results for the ellipsoid are seen to be higher than results of the other two-body shapes.

Variations in the shock-standoff distance, illustrated in Fig. 53, indicate that the standoff distances for the ellipsoid are much greater than for the sphere cone, and, for the most part, the hyperboloid results fall between these two results. For the ellipsoid, the effect of blunting is seen to be quite pronounced in the stagnation region. As such, one would expect a higher stagnation-region heating rate for the ellipsoid.

The shock-temperature variations, illustrated in Fig. 54, indicate that the temperatures are higher for the ellipsoid near the stagnation region, but they fall between the results of the hyperboloid and sphere cone between $s = 0.6$ and 1.2 . After location $s = 1.2$, the results are slightly lower than the results of the sphere cone. In general, the shape change is seen to have greater effect on the temperature distribution for the ellipsoid than for the sphere cone. Variations in the shock density (Fig. 55) follow essentially the same trend as the temperature variations. The effects of shape change for the ellipsoid, however, are

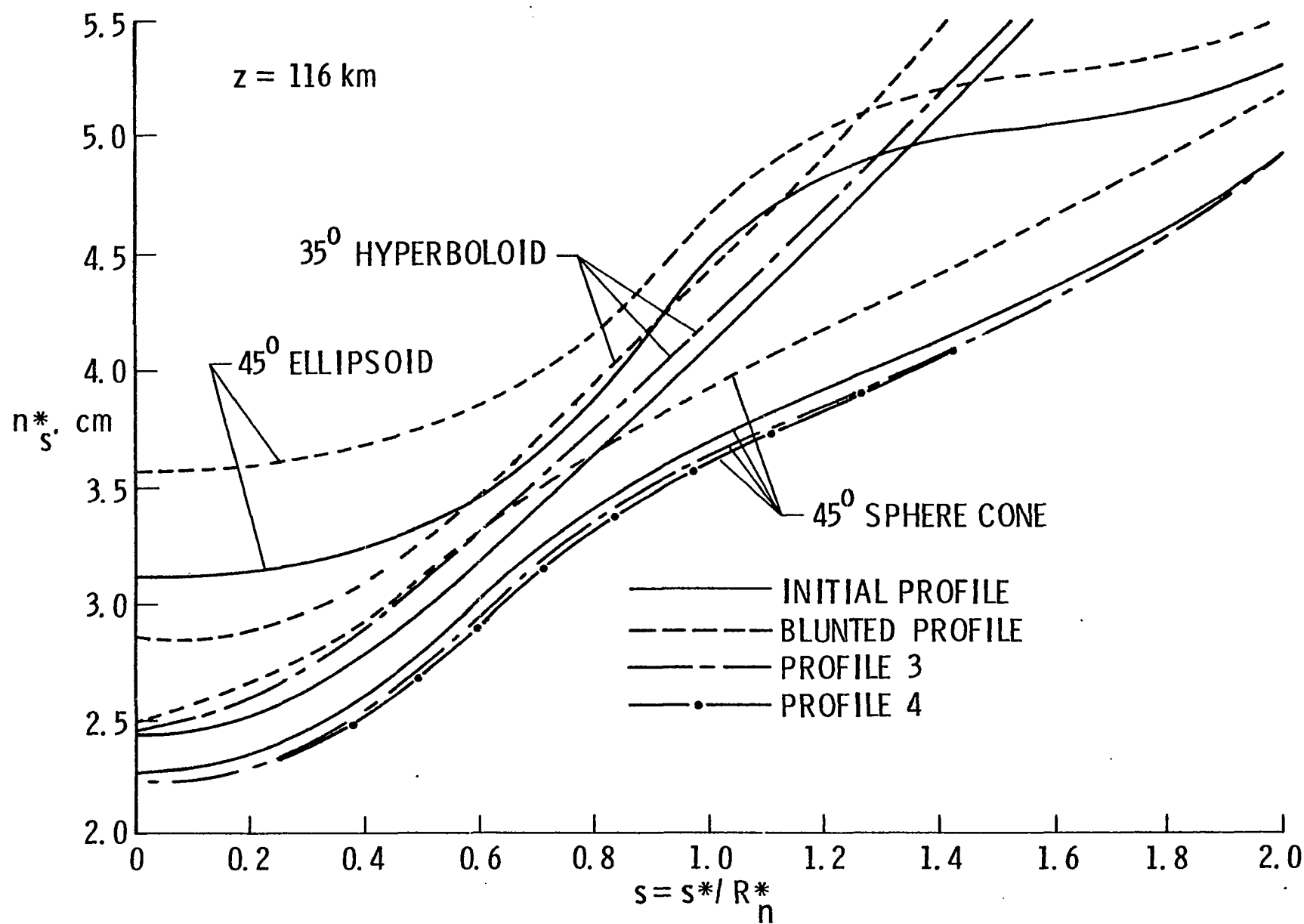


Fig. 53 Comparison os shock standoff distance for $Z = 116$ km.

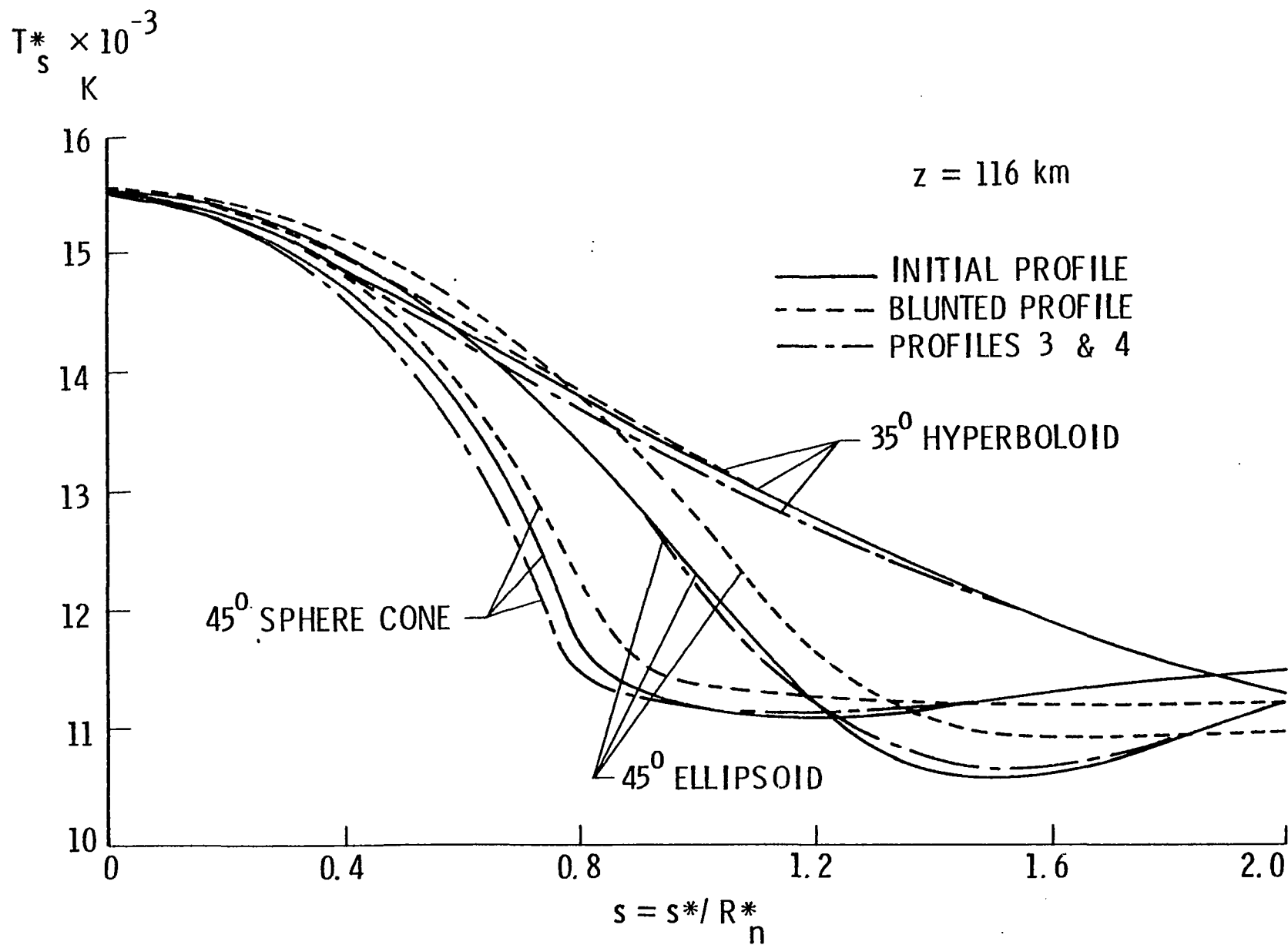


Fig. 54 Comparison of shock temperature for $Z = 116$ km.

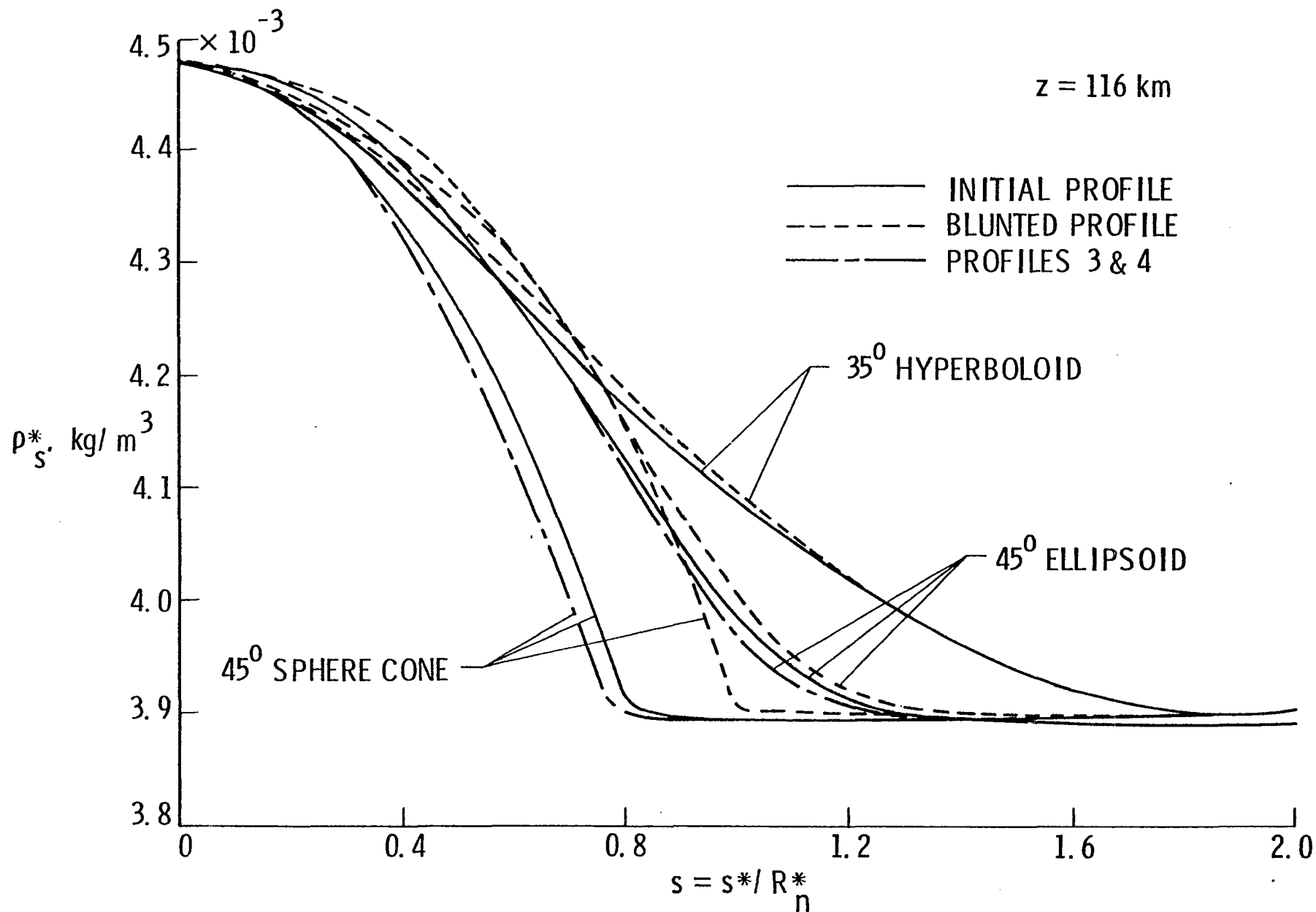


Fig. 55 Comparison of shock density for $Z = 116$ km.

not as pronounced as for the sphere cone. For the ellipsoid, blunting results in a maximum increase in density of 1.2 percent at $s = 0.8$. The results of uniform mass loss, however, do not show any significant change.

The pressure distribution along the body surface is illustrated in Fig. 56. The results show that the shape change has a considerable effect on the pressure variations for the ellipsoid in the range $s = 0.6$ to 1.2. The total drag for the ellipsoid, however, may not be greater than that for the sphere cone. As noted earlier, the shape change does not have significant influence on the pressure distribution for the hyperboloid, but the total drag for this shape can be higher than the other two shapes.

The radiative heating rates for the three entry shapes are compared in Fig. 57. As expected, the radiative heating rates for the ellipsoid are comparatively higher in the stagnation region. In the downstream region, however, the results fall between the results of the hyperboloid and sphere cone. For the ellipsoid, blunting results in a maximum increase in heating of 7 percent at $s = 0.8$. In general, the increase in heating rates due to shape change is seen to be greater for the sphere cone and ellipsoid than for the hyperboloid. Also, the shape change is seen to have considerably more effect on heating of the afterbody for the sphere cone and ellipsoid than for the hyperboloid. The results further indicate that the total radiative heating load (i.e., the total radiative heat input) to the entry body will be comparatively higher for the ellipsoid, and this will be followed by the results for the hyperboloid and sphere cone, respectively.

The results presented in this section indicate that uniform mass loss resulting in a shape that corresponds closely to the initial

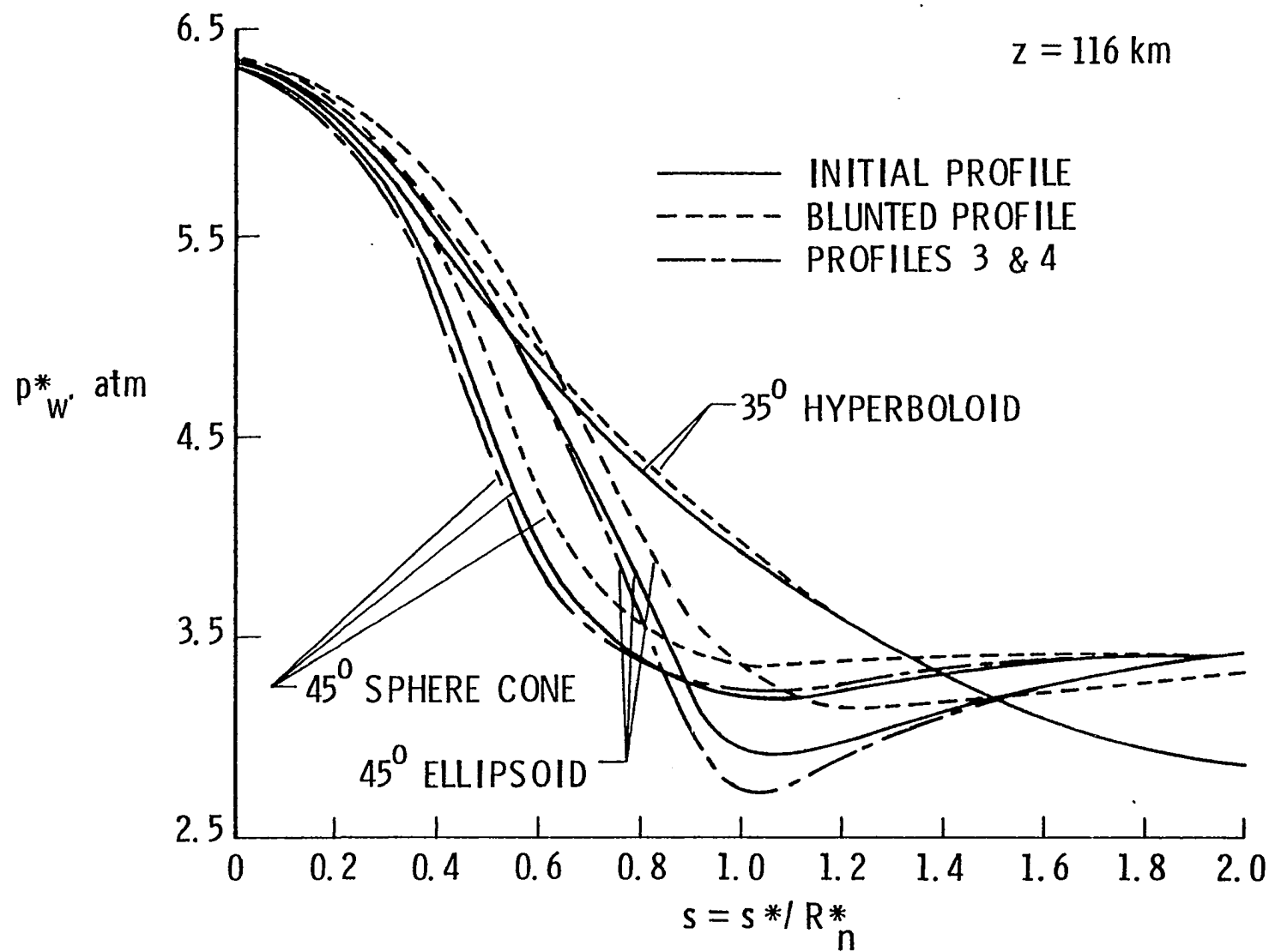


Fig. 56 Comparison of surface pressure for $Z = 116 \text{ km}$.

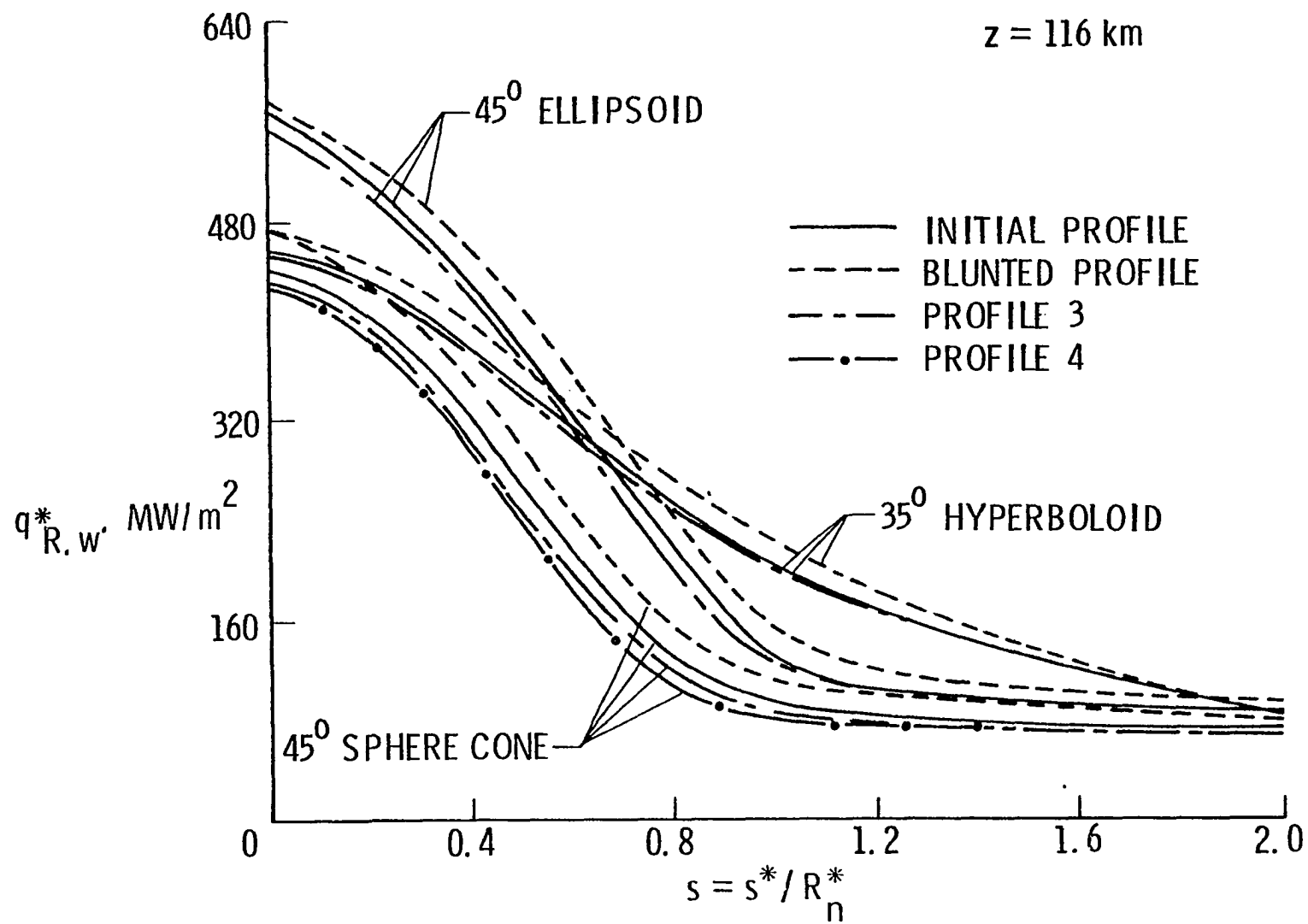


Fig. 57 Comparison of radiative heating rates for $z = 116 \text{ km}$.

profile does not affect the shock-standoff distance, temperature, density and pressure distribution along the body appreciably. In such cases, radiative heating rates to the body are not different significantly from the heating rates to the body with initial configurations. Blunting of the nose region, however, is seen to have a significant influence on the entire flow phenomena in the stagnation and downstream regions. It is noted that the shock-standoff distance increases with increasing nose blunting. While nose blunting results in increasing the shock temperature all along the body, its influence on increasing the density is significant only in the stagnation region. In the downstream regions, the velocity, density, temperature, and pressure are altered significantly across the shock layer because of changes in the probe configurations. In most cases, considerable increase in radiative heating rates is noted in the stagnation as well as downstream regions due to severe nose blunting. Blunting of the entry body is seen to increase the wall pressure distribution significantly. But, its effect on stagnation-region and afterbody pressure distribution is relatively small. However, it is possible for the blunted sphere cone and ellipsoid to experience relatively higher total drag. Blunting is seen to increase the radiative heating rates all along the body for all configurations considered. But, in the stagnation region, the increase is relatively higher for the ellipsoid and sphere cone than for the hyperboloid. The shape change is seen to have considerably more effect on heating of the afterbody for the sphere cone and ellipsoid than for the hyperboloid. It is further noted that the total radiative heating load to the body will be comparatively higher for the ellipsoid followed by that for the hyperboloid and sphere cone.

CONCLUSIONS

Results were obtained to investigate the influence of simplified radiation models, nonequilibrium radiative energy transfer and probe configuration changes on the flow properties and the heating rates in the stagnation and downstream regions of a Jovian entry body. Results obtained by using a simple 30-step radiation absorption model are found to be in good agreement with results of other sophisticated models available in the literature. It is found that use of the present model reduces the computational time significantly. However, use of this simplified model is recommended only for general parametric studies.

The radiative transfer equation has been formulated under the non-local thermodynamic equilibrium (NLTE) conditions. The NLTE effects are seen to enter through the absorption coefficient and the source function. The NLTE source function is expressed in terms of the Planck function, a NLTE parameter that measures the relative importance of the collisional and radiative deactivation processes in the gas and the influence factors arising from the higher level energy transitions. The influence of NLTE on the entire shock-layer flow phenomena is investigated by neglecting the contributions of ablative products as well as by including them.

The results obtained in the absence of the ablative species in the shock layer indicate that the NLTE effects are greater closer to the body than near the shock. The influence of NLTE, in general, is to reduce the convective and radiative heating to the entry body; a significant reduction in radiative heating is noted. The NLTE effects are greater for higher entry conditions. The NLTE results, however, are not influenced by the change in the forebody configurations.

The viscous shock-layer equations with coupled ablation and mass injection (for the entry probe with carbon phenolic heat shield) are solved under the NLTE conditions. The Swan (0,0), Freymark (0,1), and Mulliken (0,0) bands of the C_2 band systems are treated to be in nonequilibrium in the ablation layer. Flow-field results obtained for the peak-heating conditions indicate that the temperature distribution in the shock layer is lower under NLTE conditions. Similar behavior is also noticed for the enthalpy distribution. It is found that NLTE increases the density in the shock layer but it has no influence on the pressure variation. The radiative heating to the entry body is increased because of NLTE and this, in turn, results in increased mass loss from the body.

For investigating the influence of shape change of the entry probe on the flow field, different initial configurations (45-degree sphere cone, 35-degree hyperboloid, and 45-degree ellipsoid) for the entry probe were considered and results were obtained for three different entry conditions ($Z = 109, 116, \text{ and } 138 \text{ km}$). The results indicate that uniform mass loss resulting in a shape that corresponds closely to the initial profile does not affect the shock-standoff distance, temperature, density, and pressure distribution along the body appreciably. Blunting of the nose, however, is seen to have a significant influence on the entire flow phenomena in the stagnation and downstream regions. Blunting of the entry probe increases the radiative heating rates all along the body for all initial configurations considered. In the stagnation region, however, the increase is relatively higher for the ellipsoid and sphere cone than for the hyperboloid. It is concluded that, due to the shape change, the total heating load to the body will be higher for the ellipsoid than the hyperboloid and sphere cone.

REFERENCES

1. Anderson, J.D., "An Engineering Survey of Radiating Shock Layers," AIAA Journal, Vol. 7, No. 9, Sept. 1969, pp. 1665-1675.
2. Page, W.A., "Aerodynamic Heating for Probe Vehicles Entering the Outer Planets," American Astronautical Society Paper No. AAS-71-144, June 1971.
3. Olstad, W.B., "Nongray Radiating Flow About Smooth Symmetric Bodies," AIAA Journal, Vol. 9, No. 1, Jan. 1971, pp. 122-130.
4. Callis, L.B., "Coupled Nongray Radiating Flow About Long Blunt Bodies," AIAA Journal, Vol. 9, No. 4, April 1977, pp. 553-559.
5. Moss, J.N., "Reacting Viscous-Shock-Layer Solutions with Multi-component Diffusion and Mass Injection," NASA TR R-411, June 1974; also Radiative Viscous-Shock-Layer Solutions with Coupled Ablation Injection, AIAA Journal, Vol. 14, No. 9, Sept. 1976, pp. 1311-1316.
6. Sutton, K., "Fully Coupled Nongray Radiating Gas Flows with Ablation Product Effects about Planetary Entry Bodies," AIAA Paper No. 73-672, July 1973.
7. Sutton, K., Moss, J.N., Falanga, R.A., and Olstad, W.B., "Outer Planet Entry Probes Aerothermal Environment - Status of Prediction Methodology," AIAA Paper No. 75-1148, Sept. 1975.
8. Tiwari, S.N. and Szema, K.Y., "Effects of Precursor Heating on Chemical and Radiative Nonequilibrium Viscous Flow Around a Jovian Entry Body," AIAA Paper No. 78-907, May 1978; also NASA TR NSG-1492, Dec. 1978; also in Progress in Astronautics and Aeronautics: Outer Planet Entry Heating and Thermal Protection, Vol. 64, edited by R. Viskanta, AIAA, New York, 1979, pp. 129-146.
9. McWhirter, R.W.P., "Spectral Intensities," Plasma Diagnostic Techniques, edited by R.H. Huddleston and L.S. Leonard, Academic Press, New York, 1965.
10. Jefferies, J.T., "Source Function in a Nonequilibrium Atmosphere: VII. The interlocking Problem," Astrophysical Journal, Vol. 132, Nov. 1960, pp. 775-789.
11. Cottrell, T.L. and Matheson, A.J., "Transition Probability in Molecular Encounters," Faraday Society (London) Transactions, Vol. 58, July 1962, pp. 2336-2341.
12. Tiwari, S.N. and Cess, R.D., "The Influence of Vibrational Nonequilibrium upon Infrared Radiative Energy Transfer," Journal of Quantitative Spectroscopy and Radiative Transfer, Vol. 11, March 1971, pp. 237-248.

13. Tiwari, S.N. and Subramanian, S.V., "Evaluation of Upwelling Infrared Radiance in a Nonhomogeneous Nonequilibrium Atmosphere," Department of Mechanical Engineering and Mechanics, School of Engineering, Old Dominion University, Norfolk, VA, TR 76-T20, Nov. 1976.
14. Horton, T.E., "The Importance of Nonequilibrium in Estimating Radiative Heat Transfer Through a Flow," AIAA Paper No. 76-170, Jan. 1976.
15. Wilson, K.H., "RATRAP - A Radiation Transport Code 6-77-67-12," Lockheed Missiles and Space Co., Sunnyvale, California, 1967.
16. Thomas, M., "The Spectral Linear Absorption Coefficient of Gases - Computer Program SPECS (H 189)," Douglas Report DAC-59135, McDonnell-Douglas Astronautics Co., Western Division, Santa Monica, California, May 1967.
17. Nicolet, W.E., "User's Manual for the Generalized Radiation Transfer Code (RAD/EQUIL)," Aerotherm Report No. UM-69-9, Aerotherm Corp., Mountain View, California, 1969; also, "User's Manual for RAD/EQUIL/1973," A General Purpose Radiation Transport Program," NASA CR-132470, Nov. 1973.
18. Zoby, E.V., Sutton, K., Olstad, W.B., and Moss, J.N., "An Approximate Inviscid Radiation Flow Field Analysis of Outer Planet Entry Probes," AIAA Paper No. 78-189, Jan. 1978.
19. Tiwari, S.N. and Subramanian, S.V., "Significance of Radiation Models in Investigating the Flow Phenomena Around a Jovian Entry Body," Technical Report NAS1-14193-26, Jan. 1978, School of Engineering, Old Dominion University, Norfolk, Virginia; also, AIAA Paper No. 78-188, Jan. 1978.
20. Vincenti, W.G. and Kruger, C.H., Introduction to Physical Gas Dynamics, John Wiley and Sons, New York, 1965.
21. Sparrow, E.M. and Cess, R.D., Radiation Heat Transfer, Brooks/Cole Publishing Co., Belmont, California, 1966.
22. Penner, S.S. and Olfe, D.B., Radiation and Reentry, Academic Press, New York, 1968.
23. Tauber, M.E. and Wakefield, R.E., "Heating Environment and Protection During Jupiter Entry," Journal of Spacecrafts and Rockets, Vol. 8, 1971. pp. 630-636.
24. Sutton, K., "Coupled Nongrey Radiating Flow About Ablating Planetary Entry Bodies," AIAA Journal, Vol. 12, No. 8, Aug. 1974, pp. 1099-1105.
25. Sutton, K., "Radiative Heating About Outer Planetary Entry Probes," AIAA Paper 75-183, Jan. 1975.
26. Sutton, K., Jones, J.J., and Powell, R.W., "Effects of Probe Configuration on Radiative Heating During Jovian Entry," AIAA Paper 76-471, July 1976.

27. Walberg, G.D., Jones, J.J., Olstad, W.B., Sutton, K., Moss, J.N. and Powell, R.W., "Mass Loss Shape Change and Real-Gas Aerodynamic Effects on a Jovian Atmospheric Probe," Acta Astronautica, Vol. 4, May 1977, pp. 555-575.
28. Huges, W.F. and Gaylord, E.W., Basic Equations of Engineering Science, Schaum Publishing Company, New York, 1964.
29. Sutton, K., "Characteristics of Coupled Nongray Radiating Gas Flows with Ablation Produce Effects About Blunt Bodies During Planetary Entries." Ph.D. Dissertation, North Carolina State University, Raleigh, North Carolina, 1973.
30. Moss, J.N., "Radiative Viscous-Shock-Layer Solutions with Coupled Ablation Injection," AIAA Journal, Vol. 14, No. 9, Sept. 1976, pp. 1311-1316.
31. Blottner, F.G., "Finite Difference Methods of Solution of the Boundary-Layer Equation," AIAA Journal, Vol. 8, No. 2, Feb. 1970, pp. 193-205.
32. Davis, R.T., "Numerical Solution of the Hypersonic Viscous Shock-Layer Equations," AIAA Journal, Vol. 8, No. 5, May 1970, pp. 843-851.
33. Zoby, E.V., Gnoffo, P.A., and Graves, R.A., "Correlations for Determining Thermodynamic Properties of Hydrogen-Helium Gas Mixtures at Temperatures from 7,000 to 35,000 K," NASA TN D-8262, Aug. 1976
34. Sutton, K., Jones, J.J., and Powell, R.W., "Effects of Atmospheric Structure on Radiative Heating for Jupiter Entry Probe." AIAA Paper No. 78-185, Jan. 1978.
35. Szema, K.Y., "Effect of Precursor Heating on Radiating and Chemically Reaching Viscous Flow Around a Jovian Entry Body." Ph.D. Dissertation, Old Dominion University, Norfolk, Va., Nov. 1979, also NASA CR-3186, Oct. 1979.
36. Kenneth, H. and Strack, S.L., "Stagnation Point Radiative Heat Transfer," American Rocket Society Journal, Vol. 31, No. 3, 1961, pp. 370-372.
37. Hoshizaki, H. and Lasher, L.E., "Convective and Radiative Heat Transfer to an Ablating Body," AIAA Journal, Vol. 6, No. 8, Aug. 1968, pp. 1441-1449.
38. Chien, Kuei-Yuan, "Application of the S_n Method of Spherically Symmetric Radiative-Transfer Problems," AIAA Paper No. 71-466, April 1971.
39. Wilson, K.H., "Evaluation of One-Dimensional Approximations for Radiative Transport in Blunt Body Shock Layers," NASA-CR-1990, March 1972.
40. Pai, S.I., Radiation Gas Dynamics, Springer-Verlag, New York, 1966.

41. Kulander, J.L., "Curves of Growth for Nonequilibrium Gases," Journal of Quantitative Spectroscopy and Radiative Transfer, Vol. 8, June 1968, pp. 1319-1340.
42. Tiwari, S.N. and Subramanian, S.V., "Nonequilibrium Radiative Heating of Jovian Entry Body," AIAA Paper No. 79-0035, Jan. 1979.
43. Tiwari, S.N. and Subramanian, S.V., "Influence of Nonequilibrium Radiation on Heating of an Ablating Jovian Entry Probe," AIAA Paper No. 80-0356, Jan. 1980.
44. Armstrong, B.H., Johnston, R.R., and Kelly, P.S. "Opacity of High Temperature Air," Lockheed Missiles & Space Co., Report No. 8-94-64-2 (also Air Force Weapons Lab, Report AFWL-TR 65-17), 1964.
45. Nicolet, W.E., "Advanced Methods for Calculating Radiation Transport in Ablation Product Contaminated Boundary Layers," NASA CR-1656, Sept. 1970.
46. Nicolet, W.E., "Rapid Methods for Calculating Radiation Transport in the Entry Environment," NASA CR-2528, April 1975.
47. Patch, R.W., Shackelford, W.L., and Penner, S.S., "Approximate Spectral Absorption Coefficient Calculations for Electronic Band Systems Belonging to Diatomic Molecules," Journal of Quantitative Spectroscopy and Radiative Transfer, Vol. 2, July 1962, pp. 263-271.
48. Sutton, K., Moss, J.N., and Anderson, E.C., "Radiation Absorption by the C_2 Band Systems for the Jupiter Entry Conditions," AIAA Paper No. 79-0033, Jan. 1979.
49. Heitler, W., The Quantum Theory of Radiation (Third Edition), Oxford University Press, London, 1954.
50. Goody, R.M., Atmospheric Radiation I, Theoretical Basis; Oxford University Press, London, 1964.
51. Gaydon, A.G., Dissociation Energies, Chapman and Hall Ltd., London, 1953.
52. Cooper, D.M. and Nicholls, R.W., "Measurements of the Electronic Transition Moments of C_2 Band Systems," Journal of Quantitative Spectroscopy and Radiative Transfer, Vol. 15, Feb. 1975, pp. 139-150.
53. Schadee, A., "The Relation Between the Electronic Oscillator Strength and the Wavelength for Diatomic Molecules," Journal of Quantitative Spectroscopy and Radiative Transfer, Vol. 7, Feb. 1967, pp. 169-183.
54. Herzberg, G., Atomic Spectra and Atomic Structure, Dover Publications, New York, 1944.
55. Massey, M.S.W. and Burhop, E.H.S., Electronic and Ionic Impact Phenomena, Oxford University Press, London, 1956.

56. Schwartz, R.N., Slawsky, Z.I., and Herzfeld, K.F., "Calculation of Vibrational Relaxation Times in Gases," Journal of Chemical Physics, Vol. 20, No. 10, Oct. 1952.
57. Spitzer, L., Physics of Fully Ionized Gases, John Wiley and Sons, New York, 1962.
58. McBride, B.J., Heimerl, S., Ehlers, J.G. and Gordon, S., "Thermodynamic Properties to 6000 K for 210 Substances Involving the First 18 Element," NASA Report SP-3001, 1963.
59. Babu, S.G., "Approximate Thermochemical Tables for Some C-H and C-H-O Species," NASA CR-2187, March 1973.
60. Wilke, C.R., "A Viscosity Equation for Gas Mixtures," Journal of Chemical Physics, Vol. 18. No. 4, April 1950, pp. 517-519.
61. Hall, N.A., Thermodynamics of Fluid Flow, Printice Hall, Inc., New Jersey, 1957.
62. Esch, D.D., Pike, R.W., Engle, C.D., Farmer, R.C., and Balhoff, J.F., "Stagnation Region Heating of a Phenolic Nylon Ablator During Return from Planetary Mission," NASA CR-112026, Sept. 1971.
63. Moss, J.N., Anderson, E.C., and Boltz, C.W., "Viscous-Shock-Layer Solutions with Radiation and Ablation Injection for Jovian Entry," AIAA Paper No. 75-671, May 1975.
64. Moss, J.N., Anderson, E.C., and Boltz, C.W., "Aerothermal Environment for Jovian Entry Probes," AIAA Paper No. 76-469, July 1976.
65. Sutton, K. and Moss, J.N., "Radiation Absorption by C_2 Band Systems for the Jupiter Entry Conditions," AIAA Paper No. 76-0033, Jan. 1979.
66. Moss, J.N., "A Study of the Aerothermal Entry Environment for the Galileo Probe," AIAA Paper No. 79-1081, June 1979.
67. Tiwari, S.N. and Subramanian, S.V., "Influence of Nonequilibrium Radiation and Shape Change on the Flowfield of a Jupiter Probe with Ablation and Mass Injection," Department of Mechanical Engineering and Mechanics, School of Engineering, Old Dominion University, Norfolk, Va., TR NSG-1500, in Preparation

APPENDIX A

FINITE DIFFERENCE SCHEME FOR VISCOUS
RADIATING SHOCK-LAYER FLOW

APPENDIX A
FINITE DIFFERENCE SCHEME FOR VISCOUS
RADIATING SHOCK-LAYER FLOW

The solution of the second order partial differential equation expressed by Eq. (6.3) is obtained by employing the implicit finite difference scheme. For this purpose, the shock layer is considered as a network of nodal points with a variable grid space in the η -direction. The scheme is shown in Fig. A.1 where m is a station measured along the body surface and n denotes the station normal to the body surface. The derivatives are converted to finite-difference form by using Taylor's series expansions. Thus, unequal space central difference equations in the η -direction at point m, n can be written as

$$\begin{aligned} \frac{\partial W}{\partial \eta}_n = & \frac{\Delta \eta_{n-1}}{\Delta \eta_n (\Delta \eta_{n-1} + \Delta \eta_n)} W_{m,n+1} - \frac{\Delta \eta_n}{\Delta \eta_{n-1} (\Delta \eta_{n-1} + \Delta \eta_n)} W_{m,n-1} \\ & + \frac{\Delta \eta_n - \Delta \eta_{n-1}}{\Delta \eta_n \Delta \eta_{n-1}} W_{m,n} \end{aligned} \quad (A.1a)$$

$$\begin{aligned} \frac{\partial^2 W}{\partial \eta^2}_n = & \frac{2}{\Delta \eta_n (\Delta \eta_n + \Delta \eta_{n-1})} W_{m,n+1} - \frac{2}{\Delta \eta_n \Delta \eta_{n-1}} W_{m,n} \\ & + \frac{2}{\Delta \eta_{n-1} (\Delta \eta_n + \Delta \eta_{n-1})} W_{m,n-1} \end{aligned} \quad (A.1b)$$

$$\frac{\partial W}{\partial \xi}_m = \frac{W_{m,n} - W_{m-1,n}}{\Delta \xi} \quad (A.1c)$$

A typical difference equation is obtained by substituting the above

equations in Eq. (6.3) as

$$W_{m,n} = -(D_n/B_n) - (A_n/B_n)W_{m,n+1} - (C_n/B_n)W_{m,n-1} \quad (A.2)$$

where

$$A_n = (2 + a_1 \Delta \eta_{n-1}) / [\Delta \eta_n (\Delta \eta_n + \Delta \eta_{n-1})]$$

$$B_n = - [2 - a_1 (\Delta \eta_n - \Delta \eta_{n-1})] / (\Delta \eta_n \Delta \eta_{n-1}) - a_2 - a_4 / \Delta \xi_{m-1}$$

$$C_n = (2 - a_1 \Delta \eta_n) / [\Delta \eta_{n-1} (\Delta \eta_n + \Delta \eta_{n-1})]$$

$$D_n = a_3 - a_4 W_{m-1,n} / \Delta \xi_{m-1}$$

Now, if it is assumed that

$$W_{m,n} = E_n W_{m,n+1} + F_n \quad (A.3)$$

or

$$W_{m,n-1} = E_{n-1} W_{m,n} + F_{n-1} \quad (A.4)$$

then by substituting Eq. (A.4) into Eq. (A.2), there is obtained

$$\begin{aligned} W_{m,n} = & [-A_n / (B_n + C_n E_{n-1})] W_{m,n+1} \\ & + (-D_n - C_n F_{n-1}) / (B_n + C_n E_{n-1}) \end{aligned} \quad (A.5)$$

By comparing Eqs. (A.3) and (A.5), one finds

$$E_n = -A_n / (B_n - C_n E_{n-1}) \quad (A.6)$$

$$F_n = (-D_n - C_n F_{n-1}) / (B_n + C_n E_{n-1}) \quad (A.7)$$

Now, since E_1 and F_1 are known from the boundary conditions, E_n and F_n can be calculated from Eqs. (A.6) and (A.7). The quantities $W_{m,n}$ at point m, n can now be calculated from Eq. (A.3).

The overall solution procedure starts with evaluation of the flow properties immediately behind the shock by using the Rankine-Hugoniot

relations. With known shock and body surface conditions, each of the second-order partial differential equations are integrated numerically by using the tridiagonal formalism of Eq. (6.3) and following the procedure described by Eqs. (A.2) to (A.7). As mentioned before, the solutions are obtained first for the stagnation streamline. With this solution providing the initial conditions, the solution is marched downstream to the desired body location. The first solution pass provides only an approximate flow-field solution. This is because in the first solution pass the thin shock-layer form of the normal momentum equation is used, the stagnation streamline solution is assumed to be independent of downstream influence, the term $dy_s/d\xi$ is equated to zero at each body station, and the shock angle α is assumed to be the same as the body angle θ . All these assumptions are removed by making additional solution passes.

In the first solution pass, the viscous shock-layer equations are solved at any location m after obtaining the shock conditions from the free-stream conditions. The converged solutions at station $(m-1)$ are used as the initial guess for the solution at station m . The solution is iterated locally until convergence is achieved. For the stagnation streamline, guess values for dependent variables are used to start the solution. In the first local iteration, $(\partial n_s/\partial \xi)$ and $(\partial W/\partial \xi)$ are assumed to be zero. The energy equation is then integrated numerically to obtain a new temperature. By using this temperature, new values of thermodynamic and transport properties are calculated. Next, the x-momentum equation is integrated to find the \bar{u} component of velocity. The continuity equation is used to obtain both the shock standoff distance and the \bar{v} component of velocity. The pressure \bar{P} is

determined by integrating the normal momentum equation. Then the equation of state is used to determine the density value.

With known stagnation streamline solution and body surface and shock conditions, the above procedure is used to find solutions for any body location m . The flow chart for the computational procedure is shown in Figs. A.2 and A.3. Further details of this procedure and flow chart are given in Ref. 35. The flow chart for the NLTE radiation computation is shown in Fig. A.4 and the integrals used in this chart are defined in Fig. A.5.

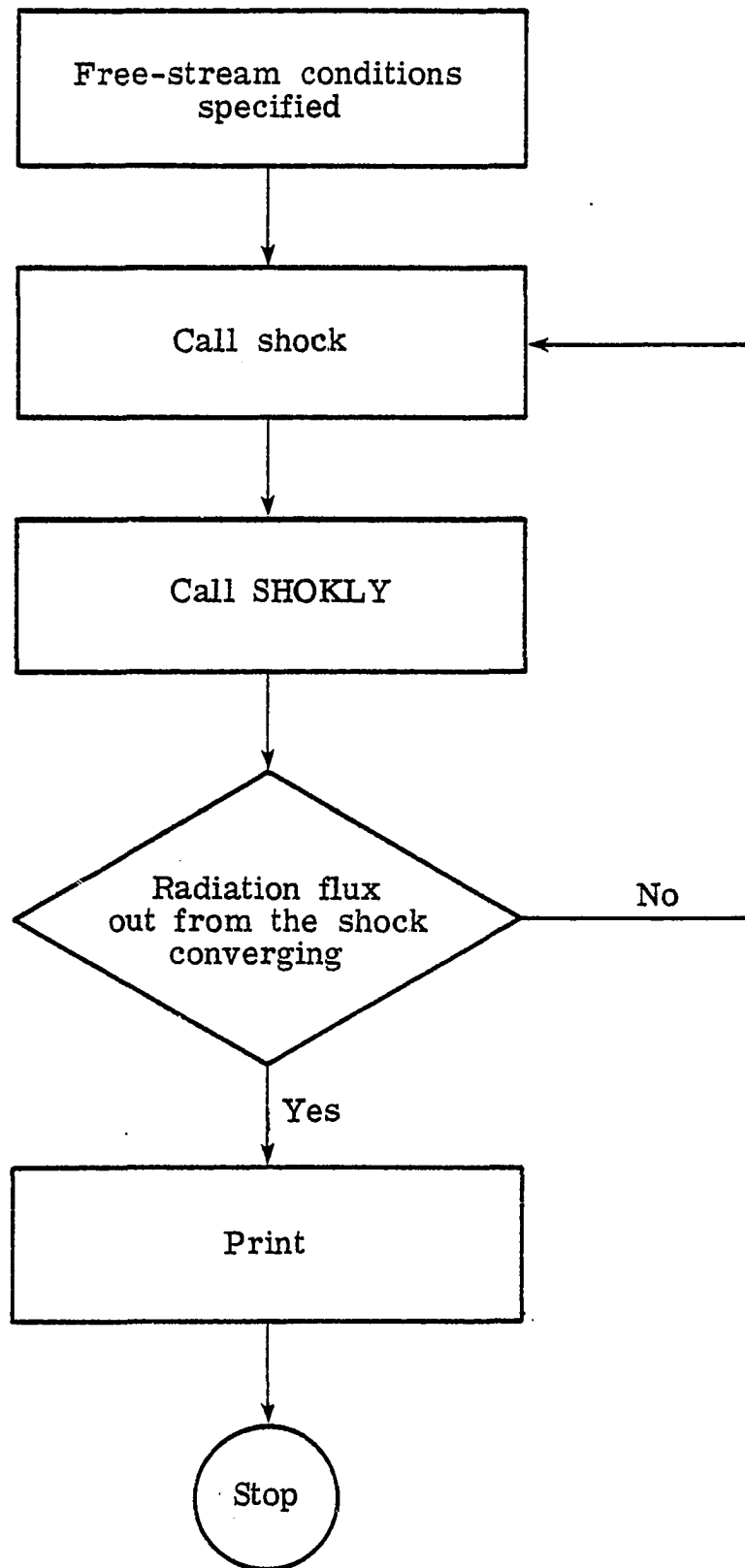


Fig. A.2 Flow-chart for shock-layer solution procedure.

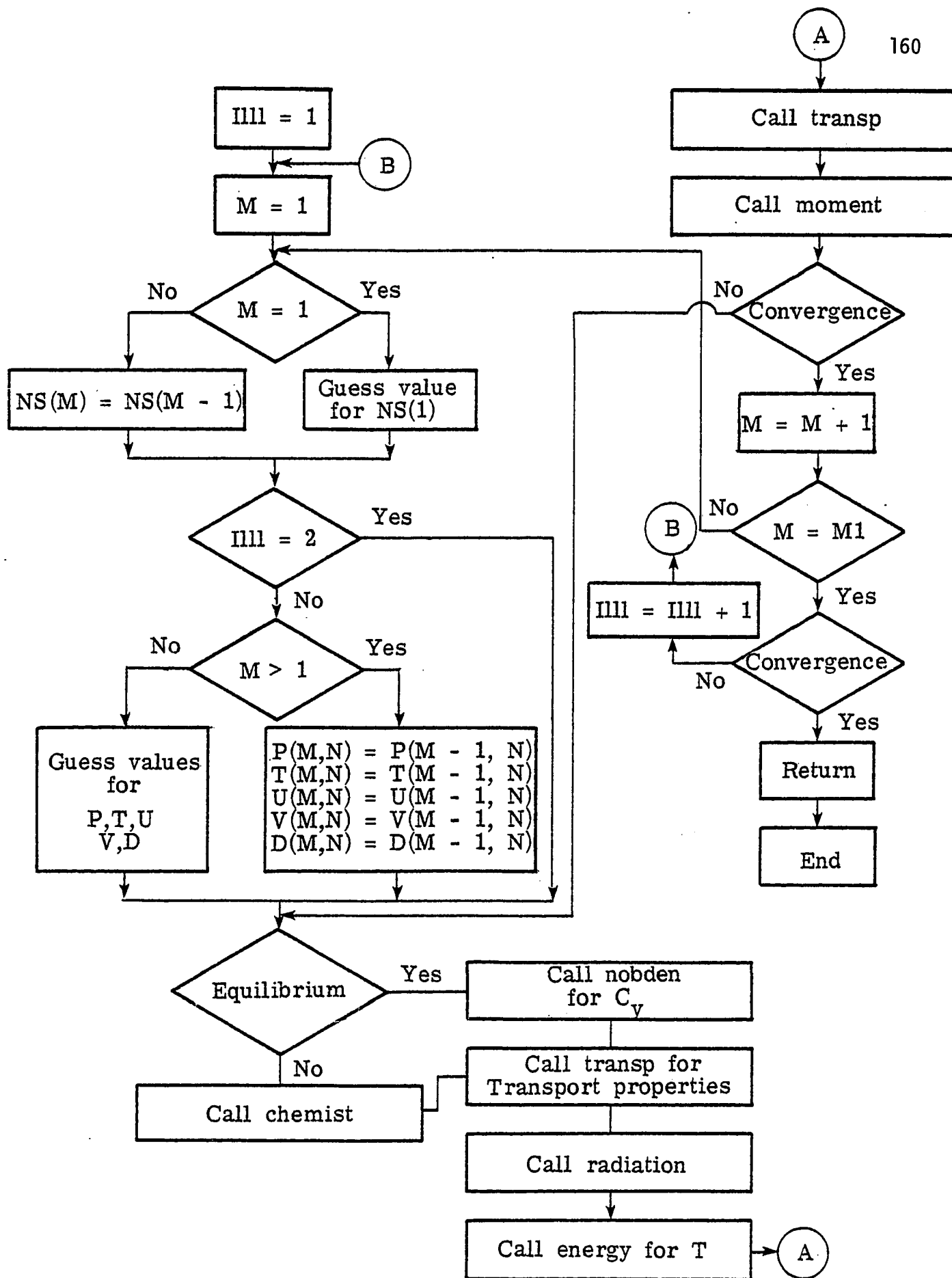


Fig. A.3 Flow-chart for subroutine SHOKLY for shock-layer solution.

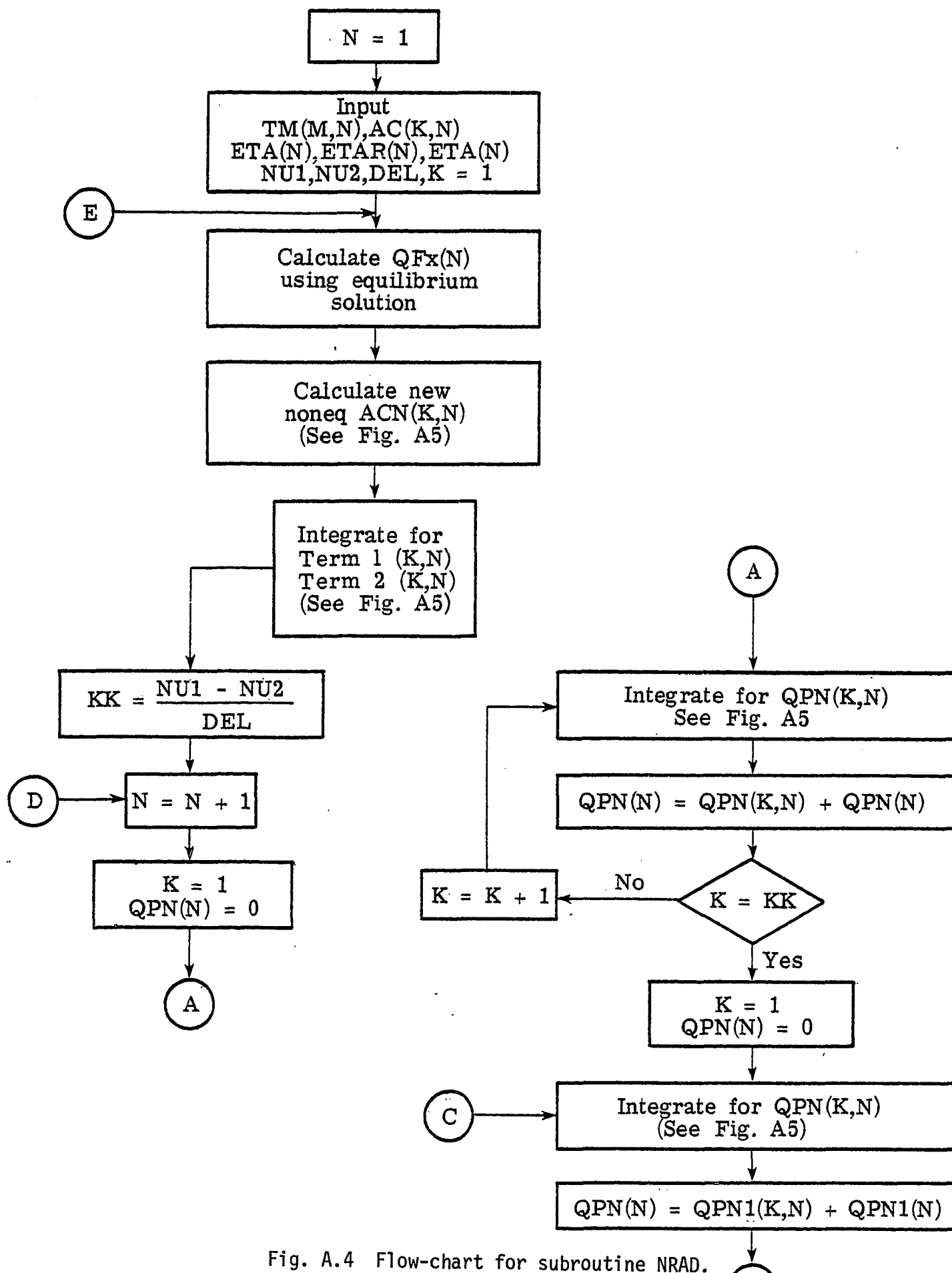


Fig. A.4 Flow-chart for subroutine NRAD.

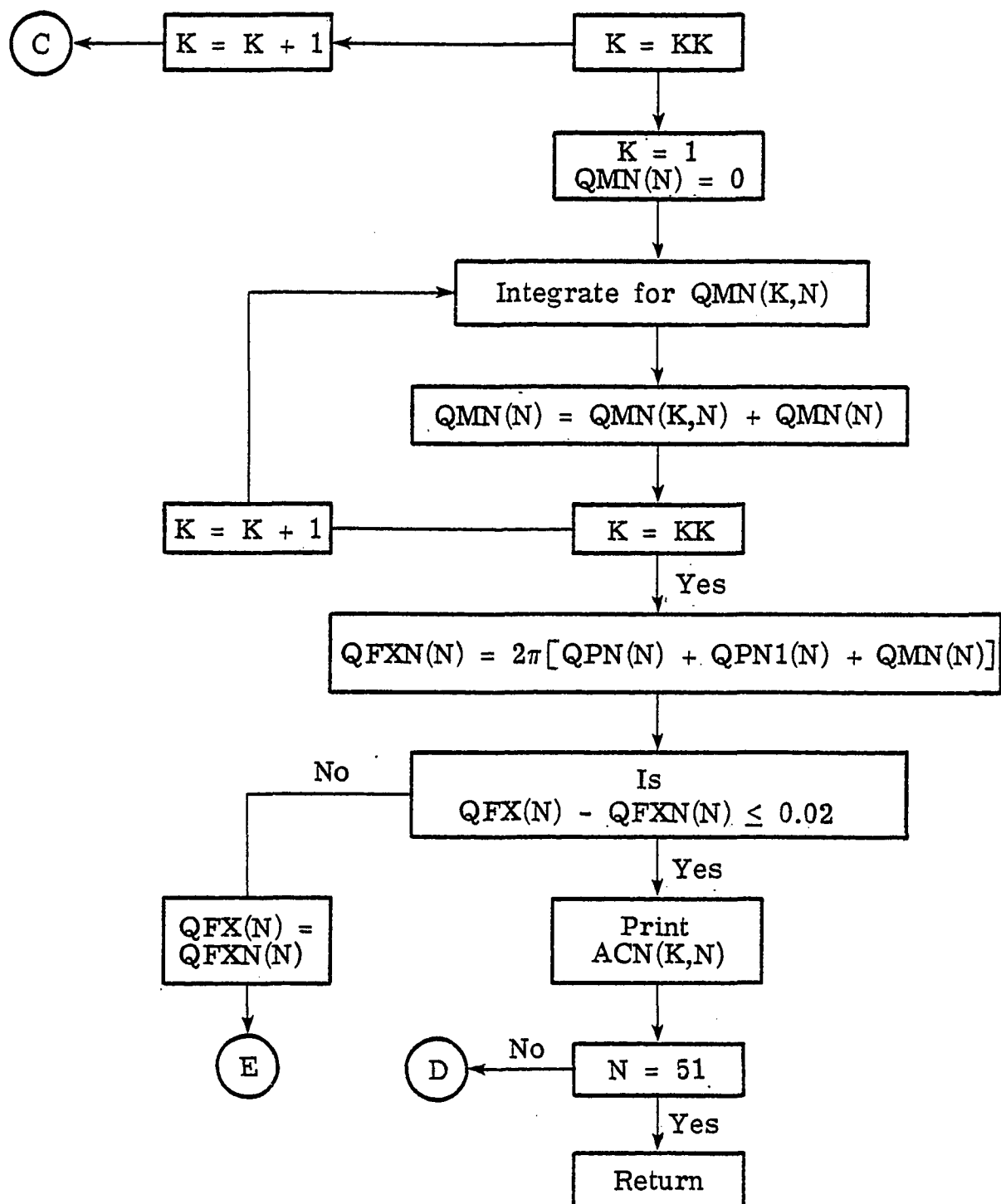


Fig. A.4 Flow-chart for subroutine NRAD. (Concluded).

$$ACN(K,N) = AC(K,N) \left[1 + \eta + h\eta/2(\nu_{1k}^4 - \nu_{2k}^4) \right] / \bar{X}$$

$$\bar{X} = \int_{\nu_{k1}}^{\nu_{k2}} \left\{ 2h\eta\nu^3/c^2 + \exp(-h\nu/kT) \right\} d\nu$$

$$X_1 = \int_{\nu_{k1}}^{\nu_{k2}} \nu^3 / [\exp(\nu) - 1] d\nu$$

$$X_3 = \int_{\nu_{k1}}^{\nu_{k2}} \left\{ \nu^3 / [\exp(k\nu - 1)] \right\} d\nu$$

$$X_2 = \eta \left[QFX(N + 1) - QFX(N) \right] / 4\pi AC(K,N) \cdot DN$$

$$\text{Term 1 (K,N)} = (2h/c^2) (kT^4/h) X_1 - X_2$$

$$\text{Term 2 (K,N)} = (\epsilon h/c^2) X_3$$

$$QPN(K,N) = \int_0^N \text{Term 1 (K,N)} ACN(K,N) E_2 \left[\int_0^N \alpha_j(N') dN' \right] d\xi$$

$$QPN1(K,N) = \int_0^N \text{Term 2 (K,N)} E_3 \left[\int_0^N \alpha_j(N') dN' \right] d\xi$$

$$QMN(K,N) = \int_N^\xi \text{Term 1 (K,N)} ACN(K,N) E_2 \left[\int_N^\xi \alpha_j(N') dN' \right] d\xi$$

Fig. A.5 Definition of integrals used in NRAD.

BIOGRAPHY

Sundaresa Venkata Subramanian was born on May 19, 1951 in Tiruvaiyaru, Madras, India. In June 1972, he received his Bachelor of Engineering degree from University of Madras. Soon after graduating, he was employed by the Indian Space Research Organization as an Aerodynamic Engineer till August 1974 when he came to the United States for pursuing his graduate study program. After completing one semester at the City College of the City University of New York, he enrolled in the NASA/ODU Aeronautics fellowship program and received the Master of Engineering degree in Mechanical Engineering from Old Dominion University in December 1976.

He commenced full-time study and research work towards the doctoral degree in January 1977 and completed the course requirements in May 1978. During the period of his research, he was very closely associated with the Aerothermodynamics Branch of the Space Systems Division at NASA Langley Research Center, Hampton, Virginia.